Doppler Velocimetry Lidar with Amplified Reference Beam Storage Loop

A thesis submitted to the

University of Waikato

for the degree

of

Doctor of Philosophy in Physics and Electronic Engineering

by

Jyi-Lai Shen

The
University
of Waikato
Te Whare Wānanga
o Waikato

Hamilton, New Zealand
September 2003

Abstract

Wind shear and clear air turbulence are phenomena in which wind speeds can change rapidly presenting a threat to aircraft and their passengers. Lidar is a proven technique for wind speed measurement but remains a research tool only and is not yet commercially viable as an early warning system. This is mainly due to the expense and bulk of the single frequency injection locked lasers required for long-range coherent measurements.

A different design philosophy for a pulsed Doppler lidar system has recently been presented in the literature, where the reference beam pulse is stored in a fibre optic storage loop. Each successive reference pulse has travelled a distance equivalent to the measurement beam's path length. This approach reduces the coherence requirements and allows the use of cheaper, smaller, and lower coherence sources. However, a major problem of this system is that the energy of the stored pulses decays exponentially.

This thesis introduces a new and improved reference pulse storage loop, which includes an erbium doped fibre amplifier to compensate for the decay of the reference signal. Details of the design are presented. The original storage loop concept is transferred to the fibre optics telecommunication wavelength range of 1.55μm. The noise and gain of the system is characterized. Special attention is paid to avoiding laser oscillation while maintaining sufficient gain. The components, like isolators, filters, and polarisation controllers, required to achieve satisfactory operation are presented. Electronic and software techniques based on phase lock loop and wavelet transformation are included in the overall system design to reduce noise. The experiments prove that the amplitude of 16 stored pulses remains constant to within 10% fluctuation.

To prove the validity of the concept the velocity of a rotating mirror is measured at various measurement distances of 0 to 583 m that coincide with the 16 reference pulses. The experiments show successful optical mixing between the stored amplified reference and the delayed measurement beams. In the range 1 to 10 m/s the velocity can be determined to better than ±0.14 m/s (standard deviation). Software

simulations of the system indicate that with improved equipment measurements should be possible for up to 70 stored pulses, which correspond to a measurement distance of 2,550 m.

The results obtained illustrate that the amplified reference beam storage loop is a viable concept for Doppler lidar velocimetry.

Acknowledgements

I am extremely grateful to be educated in applied optics by a distinguished physicist and chief supervisor Dr. Rainer Künnemeyer. Personal gratitude for his patience, guidance, support and friendship over the last four years as I have worked towards this thesis.

In addition, without the help and support of great many people it may not have been possible to complete this thesis. To Dr. Adrian Dorrington I am more than grateful, for his efforts during the writing of this thesis and many thought provoking discussions and experimental instruction. Also, thank you Dr. Howell Round and Dr. Paul Gaynor for their encouragement to finish my PhD. Thanks to the staff, Heidi, Steward, Bruce and Scotty in the Department of Physics and Electronic Engineering for their timely assistance.

Many thanks must go to my best friends Susan-Stephen, Anne-Oscar, and Gloria-Stone with whom I have enjoyed many stimulating evenings of wine and conversations in the fishing boat and for their generosity in the form of the many cups of tea, lunches and dinners over the last three years. Finally, thanks must also go to Yee and Yi, Hsin-Chuan and Kyle for their assistance. Above all, very special thanks to Mum and Dad, and wife Tai-Chun for their patience and support.

Contents

List of figures

Abbreviations

AM	Amplitude modulation
AOM	Acousto-optic modulator
ARBS	Amplified reference beam storage
BDF	Beam delay fibre
CMOS	Complementary metal oxide semiconductor
CW	Continuous wave
DBF LD	Distributed feed back laser diode
DBM	Dual beam mode
DIAL	Differential absorption lidar
EDFA	Erbium doped fibre amplifier
EM	Electromagnetic
FFT	Fast Fourier transforms
FM	Frequency modulation
IC	Integrated circuit
LDA	Laser Doppler anemometry
LDM	Laser diode module
LDV	Laser Doppler velocimetry
LO	Local oscillator
OC	Optical coupler
OI	Optical isolator
PC	Polarisation controller
PCB	Printed circuit board
PLLD	Phase-locked loop demodulation
PM	Phase modulation
RBS	Reference beam storage
RF	Radio frequency
RM	Rotating mirror
S/N	Signal to noise (ratio)
SMFC	Single mode fibre coupler
TF	Tunable interference filter
VCO	Voltage controlled oscillator
VHC	Very high speed CMOS
WDM	Wavelength division multiplexer

Chapter 1

Introduction

1.1 Rationale

Wind shear and clear-air turbulence are atmospheric phenomena in which wind speeds can change rapidly presenting a threat to aircraft and their passengers (NASA 1998). Figure 1.1 pictures how wind shear affects an aircraft. The downdrafts are a danger to planes especially during takeoff and landing (NASA, 1992b). As NASA (1992a) reported, between 1964 and 1985 wind shear has caused fatalities and injuries in the United States of America. Though lidar is a proven technique for wind speed measurement, clear air turbulence and wind shear detection (NASA 1992b), it remains a research tool only and is not commercially viable as an early warning system. This is mainly due to the expense and bulk of the single frequency injection locked lasers required for long-range coherent measurements.

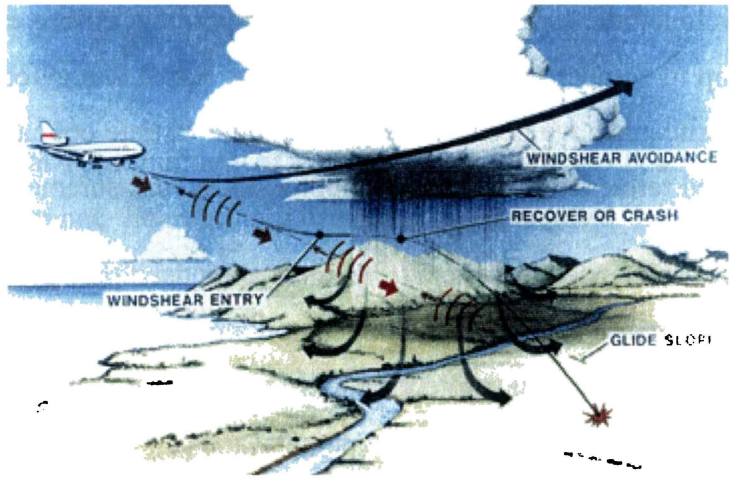

Figure 1. 1 - This artist's sketch shows how windshear affects an aircraft. (NASA, 1992b)

The problem with using a low coherence laser source for lidar systems is that a long path difference between measurement and reference beams causes the loss of

coherence before mixing of the beams. This implies that the reference beam must travel a distance of equal magnitude to that of the measurement beam.

A new lidar design philosophy in which the transmitted pulse is sampled and stored in a fibre optic ring resonator has previously been proposed by Dorrington *et al.* (2001) in "Reference-beam storage for long-range low-coherence pulsed Doppler lidar". The authors generate a reference beam consisting of a pulse train that has travelled a distance equivalent to the measurement beam's path length, reducing the coherence requirements and allowing the use of cheaper and smaller laser sources. However, the proposed system is limited by the decay of the stored energy.

In this thesis we expand the concept and attempt to overcome some of the problems associated with the previous storage loop design. The aim is to investigate whether we can

- move to the telecommunication wavelength range around 1550 nm rather than using the 632 nm wavelength,
- reduce the rapid amplitude decay of the stored reference pulses,
- increase the number of pulses that are useful, and
- progress the concept closer to a viable wind shear detection system .

We have developed the concept to include an erbium-doped fibre amplifier (EDFA) inside the loop to compensate for losses, including output energy coupling. Proof of concepts experiments have been conducted that demonstrate optical mixing between amplified stored reference pulses and a Doppler shifted measurement beam.

To develop the reference pulse storage requires an understanding of a wide range of topics including lidar, laser Doppler velocimetry, atmospheric Doppler lidar, and low coherence lidar theory. This project details an amplified reference pulse storage design, the hardware and software developments, and concepts of the optical system.

1.2 Description of thesis

The aim of the work presented is to further develop the existing reference beam storage lidar system, to increase the number of reference beam pulses which remain coherent, stable, and equal over a large number of passes through a reference beam storage loop. This would reduce the size and cost of the present lidar systems making them commercially viable for the aviation industries on the ground as well as in the air.

The next chapter discusses the background theory of lidar especially the techniques used for laser Doppler lidar. The reference pulse storage method is also introduced with the concept of low coherence lidar. This is the main inspiration for the presented work on the amplified reference beam storage.

Chapter three presents the theory for using an erbium-doped fibre amplifier for reference pulse storage. Topics covered include the gain and noise characteristics and the four different pumping configurations available. Furthermore, special optical components that are used in the amplified reference beam storage loop are also covered in detail.

The signal processing techniques used to reduce the noise of the output signal are presented in Chapter four. This chapter will first discuss in detail phase-locked loop demodulation and then the discrete wavelet transforms of a one-dimensional signal. Finally, the last section will present how to perform a peak search on the fast Fourier transformed (FFT) data.

The experimental configuration of the amplified reference beam storage for low coherence long-range lidar is proposed and demonstrated in chapter five. The components discussed in chapter three are inserted into a reference beam storage loop in an attempt to increase the number of Doppler bursts from the previous reference beam storage loop design. Experimental results are presented to determine if the amplified reference beam storage loop would allow amplitude equalization of the reference pulses.

The results obtained from the experiments are described in Chapter six. Velocity measurements with the amplified reference beam storage are presented to validate

the concept. This is done using a rotating mirror to cause a Doppler shift in the measurement beam.

Chapter seven contains a summary of the effectiveness and performance of the improved reference pulse storage, as well as possible improvements that could be made in the future.

Chapter 2

Introduction to velocimetry lidar

Lidar is similar to the more familiar radar and can be thought of as laser radar. In radar, radio waves are transmitted into the atmosphere, which scatters some of the power back to the radar's receiver. Lidar also transmits and receives electromagnetic radiation but at a higher frequency. Lidars operate in the ultraviolet, visible and infrared region of the electromagnetic spectrum.

Actually, "Lidar" is an acronym for "Light Detection and Ranging". It can be used to detect and track objects as a remote sensing technique in a non-contact and non-destructive manner. Generally, a lidar system can measure properties in the atmosphere such as distance, velocity, particle size, temperature and chemical content of objects at a remote location.

Different types of lasers are used depending on the power and wavelength required. The lasers may be either continuous wave or pulsed. Generally, the pulsed light source is made up of several components including laser, modulating driver and pulse circuit. The final output of the transmitter typically has pulse widths of about 10 ns to 100 ns.

2.1 Lidar overview

A simplified block diagram of lidar consists of a transmitter, receiver and detector system. The lidar's transmitter is a laser, while its receiver is an optical telescope and detection system. The lidar transmits light from a laser, which is then directed through a telescope and usually a scanner toward the target. The backscattered or reflected signal from the target travels toward lidar and is then detected by the

receiver. When using appropriate signal processing to analyse this data the returned signal can describe the physical properties of the target.

Lidar typically uses extremely sensitive detectors, e.g. photo-multiplier tubes, to detect the backscattered light. Photo-multiplier tubes convert the photons into electric currents, which can be stored and processed on a computer. The electric currents received are recorded for fixed time intervals during the return pulse.
Various lasers are used depending on the required power and wavelength. Similarly, differing physical processes in the atmosphere are related to different types of light scattering. Choosing diverse scattering processes allows atmospheric composition, temperature and wind to be measured.

2.1.1 Categories of lidar

Lidar may be divided into three classes according to the detection technique (Drain 1980). Autodyne lidar is the first of these and the simplest one. It is an incoherent method. The other lidar methods are homodyne and heterodyne, both of which are coherent. The following sections discuss these three systems in more detail.

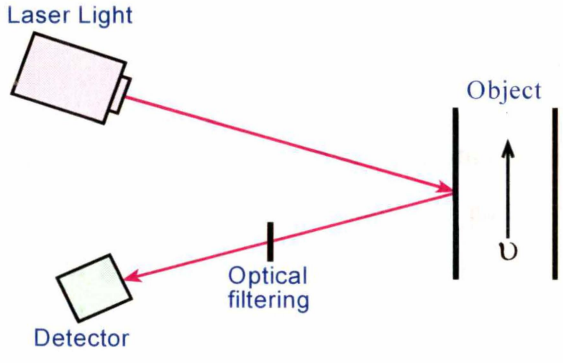

Figure 2. 1 - Autodyne lidar system.

The incoherent lidar technique is also called 'direct detection' or 'incoherent detection' lidar. Figure 2.1 shows an incoherent lidar system in which a light beam produced from a laser is directly incident on a moving object. A quantity of the laser beam is scattered back through an optical filtering unit towards the detector. This is called the autodyne lidar system.

Though the pre-detection filtering can make use of timing and spectral information, the lidar system cannot retain any phase information. It is useful for aerosol

measurements but has a lower signal to noise ratio than coherent lidar systems (McGill and Skinner, 1997).

The coherent lidar systems have been used for remote sensing since 1960. This technique works out the full frequency, phase and timing information of the received signal through optical mixing techniques (Vaughan *et al.*, 1996; Huffaker *et al.*, 1996).

Figure 2.2 shows a coherent lidar employing laser light that passes through a beam splitter and separates into two beams. This is known as the homodyne lidar system. The returned signal from the target is mixed with a portion of the reference laser beam resulting in a beat signal at the detector. The beating is caused by a frequency difference between the unshifted laser signal of the reference beam and the Doppler shifted return signal of the measurement beam.

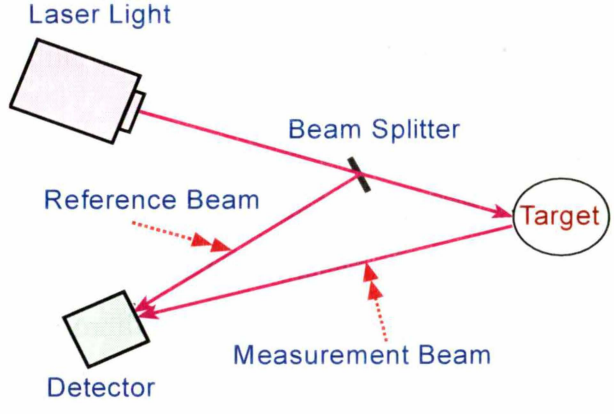

Figure 2. 2 - Homodyne lidar system.

Figure 2.3 shows another coherent lidar called heterodyne lidar system. It is similar to the homodyne system, except that the reference beam is derived from another source. The laser illuminates an object. Light is scattered back toward a detector where it is mixed with the beam of a second, local oscillator (LO) laser, injection locked to the transmitting laser and used as a reference beam generator. A variation often used involves generating a frequency offset reference beam from the transmitting laser with a Bragg cell.

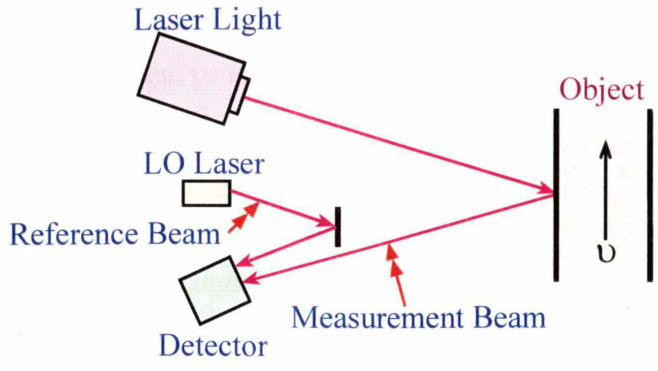

Figure 2. 3 - Heterodyne lidar system.

This heterodyne technique has high sensitivity and provides phase and velocity information useful for velocimetry, wind sensing, and detection of aircraft wake vortices. With continuous wave (CW) lidar, very high velocity resolution is possible (Harris *et al.* 1998).

2.2 Laser Doppler techniques

2.2.1 Background

Laser Doppler lidar is an important tool for measurement of atmospheric winds. Early Doppler lidars were based on coherent detection using CO_2 lasers operating at 10 μm, which is described by Hall *et al.* (1984) and Bilbro *et al.* (1984, 1986). More recently, Kavaya *et al.* (1989, 1991) have reported solid-state coherent Doppler lidars. Doppler lidars based on direct detection have also been proposed and demonstrated by Brown and Jones (1983), Chanin *et al.* (1989), Abreu *et al.* (1992) and Fischer *et al.* (1995). Coherent Doppler lidars typically offer high-sensitivity detection but require narrow-linewidth, pulsed laser technology and diffraction-limited optical receivers. The optical and laser spectral requirements for a direct-detection Doppler lidar are significantly reduced.

2.2.2 Theory of the Doppler shift

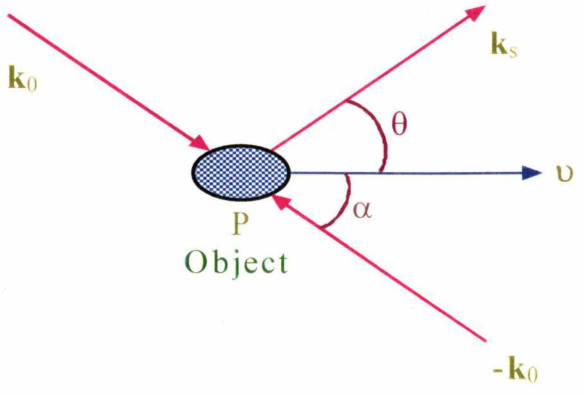

Figure 2. 4 - Light scattering by a moving object.

If a light source and observer are moving relative to each other we can detect a frequency shift based on the relative velocities. Doppler velocimetry utilises this effect. A laser is shone onto a moving object, and the reflected or scattered light is detected including its Doppler shift. This frequency deviation can then be used to calculate the speed of the object.

The scattering process is illustrated in Figure 2.4, where $\boldsymbol{k}_o$ and $\boldsymbol{k}_s$ are the wave vectors of the incident laser beam and the scattered radiation, respectively. The object P is moving with velocity vector $\boldsymbol{v}$. We then have a scattered light frequency f' given by (Drain, 1980; Tipler, 1983)

$$f' = f_0 + f_d = f_0 \cdot \frac{c - \boldsymbol{v} \cdot \boldsymbol{k_0}}{c - \boldsymbol{v} \cdot \boldsymbol{k_s}} \qquad 2\text{-}1$$

where f_0 is the frequency of the laser, f_d is the Doppler shift frequency, and c is the speed of light in free space. Using the definitions of Figure 2.5 we find

$$f_d = \frac{V}{\lambda}(cos\theta - cos\alpha) \qquad 2\text{-}2$$

where V is the magnitude of the particle's velocity, and λ is the wavelength of the incident light. If light source and detector are at the same location and the object is moving towards the source, that is θ is 0° and α is 180° then,

$$f_d = \frac{2V}{\lambda} \qquad 2\text{-}3$$

2.2.3 Laser Doppler velocimetry

Laser Doppler velocimetry (LDV) techniques can determine the Doppler shift caused by a target. Drain has reviewed these techniques in 1980 and then Schawlow in 1983. Coherent light from a laser is focused onto the measurement region and the reflected or scattered light is frequency shifted due to the motion of the target. A detection system then collects and processes the backscattered light to determine the target's velocity.

The LDV techniques are generally classified into three types. First is the differential Doppler, dual beam method (DBM) used to measure velocity. Truax *et al.*, (1984), for example, have used the dual beam technique to measure surface motion. This technique is used most often for the implementation of LDV systems because of a greater signal to noise ratio compared to the following systems.

The second technique is the two-scattered beam mode where light is collected from two directions. A beat signal can be observed when the two scattered beams are mixed, one of which is up-shifted and the other one is downshifted in frequency. Finally, there is the reference beam mode in which a reference beam and the scattered light are mixed. A beat signal is detected whose frequency is proportional to the Doppler shift.

Both, the differential Doppler and reference beam modes employ only one scattered beam, whereas the two-scattered beam mode uses two. The differential Doppler mode uses two measurement beams, and the reference beam mode employs one. All techniques are capable of determining the velocity components in more than one direction and will be discussed in more detail in the following sections.

2.2.4 Differential Doppler mode

The differential Doppler mode or dual beam mode (Figure 2.5) uses a symmetrical prism beam splitter arrangement to divide the initial laser light into two separate beams with scattered light collected in the forward direction. The principle of operation is that two measurement beams, rather than a single measurement beam, are focussed onto the flowing object; no reference beam is needed. The interference

fringe pattern of Figure 2.6 is produced in the crossover volume of the two beams. The forward scattered light is collected onto a detector.

It is desirable to collect the maximum amount of scattered light possible from the flowing object. Using a wide aperture does achieve this, and a high signal to noise ratio is obtained. Light collected in the forward direction is favoured over the backwards direction as light scattered from the flowing object is almost always greatest in the forward direction (Drain 1980).

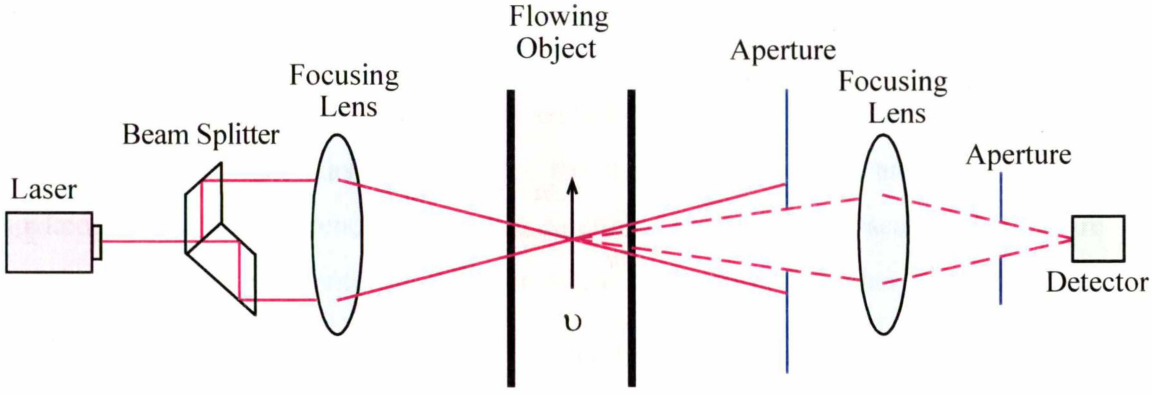

Figure 2. 5 - Dual beam mode optical arrangement.

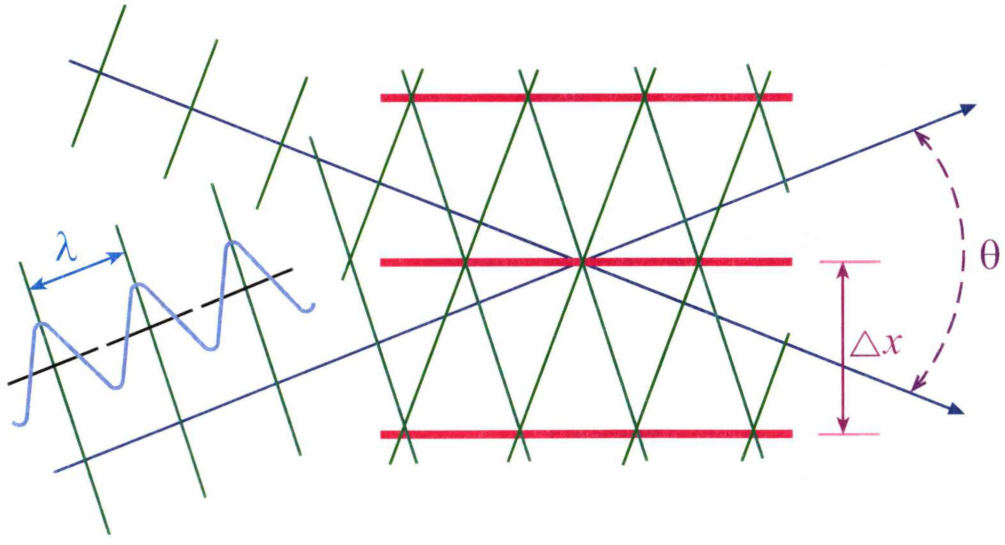

Figure 2. 6 - Interference fringe pattern for dual beam mode.

The operation of the technique in the low particle density situation can most easily be understood in terms of the fringe pattern that exits in the crossover region of the two

measurement beams. Suppose the incident angle is θ, then the distance between two interference planes is

$$\Delta x = \frac{\lambda}{2\, n \sin\left(\frac{\theta}{2}\right)} \qquad 2\text{-}4$$

where n is the refractive index of the target, and λ is the wavelength of the incident light in free space. If the particle in the target is moving with a velocity v at an angle β to the normal of the fringe planes, the planes of constructive and destructive interference will modulate the scattered light intensity. A photo detector detects this light intensity. The frequency modulation is given as:

$$\Delta f = \frac{v}{\Delta x} = \frac{2nv \cos\beta \sin\left(\frac{\theta}{2}\right)}{\lambda_0} \qquad 2\text{-}5$$

In this formula, the frequency modulation, Δf, is independent of the positioning of the photo detector. That is: we can collect scattered light anywhere, although the maximum intensity varies with the positioning of the photo detector. For this reason, the technique is sometimes called the 'intensity modulation' or 'real fringe' method. It is evident that the scattered light from the particle will also be modulated at this frequency, regardless of its direction.

2.2.5 Two-scattered beam mode

The two-scattered beam design (Figure 2.7) is very similar to the dual beam mode. Because of the different velocity components of the scattered light, there is a different effect of Doppler shift and then a different frequency deviation produced for each scattered beam.

This system can be applied to detect wind shear, blood speed, cell recognition within fluid, and wind speed over an aeroplane wing (Drain, 1980).

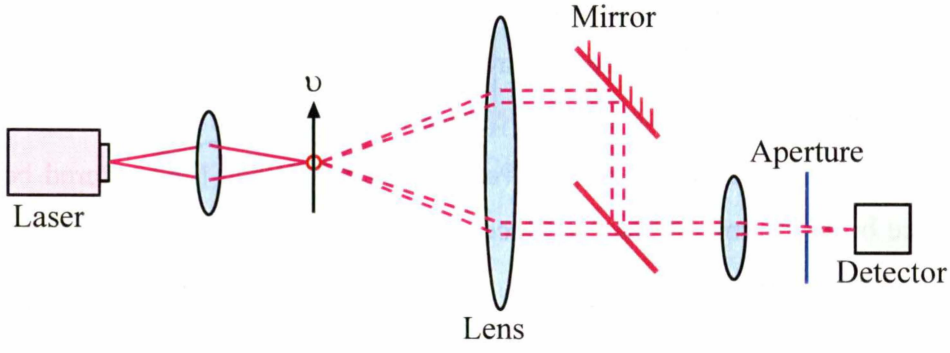

Figure 2. 7 - Optical arrangement for two-scattered beam mode.

2.2.6 Reference beam mode

There are two types of reference beam techniques; the first one uses two lasers as shown in Figure 2.8. Laser 1 provides the measurement beam and the injection locked laser 2 the reference beam. The reference beam and the scattered light are combined and focused onto the detector. Figure 2.9 shows the other method, which only has one laser split into two by a beam splitter, providing both a reference and measurement beam.

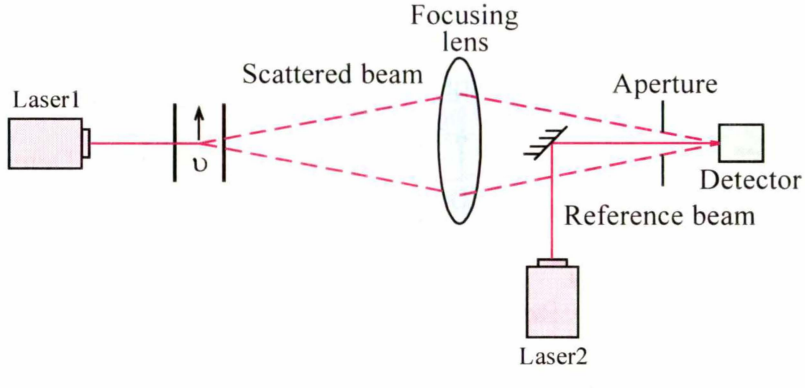

Figure 2. 8 - Optical arrangement for another laser to generate a reference beam.

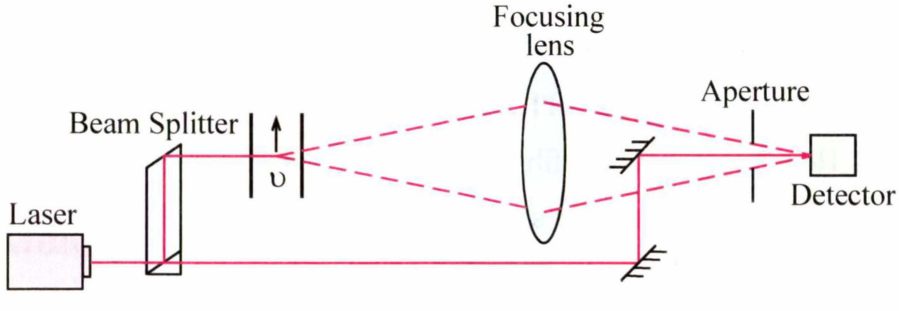

Figure 2. 9 - Optical arrangement for reference beam mode.

The reference beam technique is also called local oscillation heterodyning method for the reason that the laser beams are divided into strong and weak beams. The strong beam is incident on a moving particle to produce the scattered light and the weak beam is directed into a detector as a reference. When the scattered beam and reference beam are mixed, they produce a beat signal whose frequency is due to the Doppler shift of the scattered light.

The frequency is calculated as

$$\Delta f = \frac{2nv\ sin\left(\frac{\theta}{2}\right)}{\lambda_0} \qquad 2\text{-}6$$

where θ is the scattering angle and λ_0 is the incident wavelength. The scattering signal is usually weak, so more laser power is required compared to the dual beam mode.

A reference beam can be generated from a laser, which is divided by a beam splitter. This design is shown in figure 2.10.

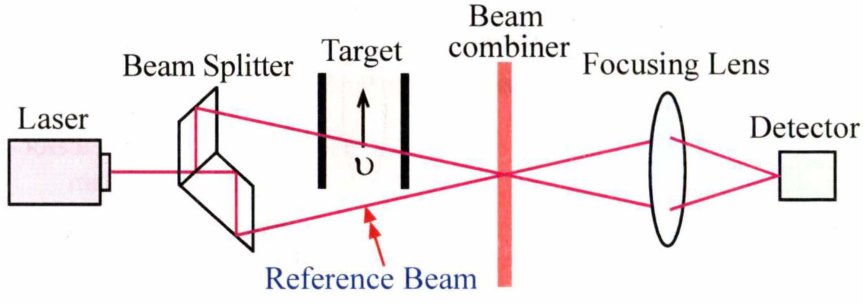

Figure 2. 10 - Generation of a reference beam.

In another arrangement the local oscillator is generated by Fresnel reflection from the fibre end at the input to the launching telescope as demonstrated by Karlsson *et al.* (2000) and shown in Figure 2.11. A flat fibre end can give a –14.7 dB (3.3%) reflection. However, when the fibre end is polished at a specific angle, a certain amount of power from the laser source will be reflected as the local oscillator for mixing with the measurement beam in the receiving detection unit.

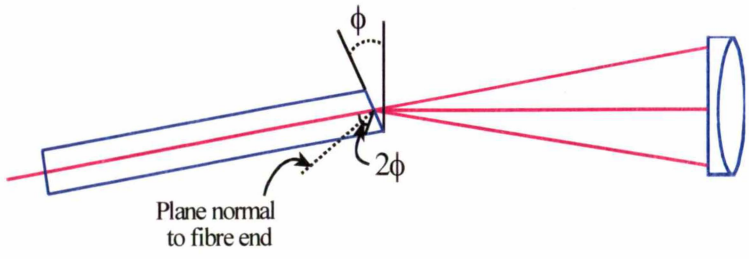

Figure 2. 11 - Angled fibre end and doublet lens of the telescope.

Suppose that the angle of the fibre end is ϕ, the reflection will be misaligned by 2ϕ relative to the mode of the fibre. The coupling efficiency (η) between two Gaussian beams (Marcuse, 1977; Kogelnik, 1964) is given as

$$\eta = \left(\frac{2W_1W_2}{W_1^2 + W_2^2} \right)^2 exp\left(-\frac{2(\pi n W_1 W_2 2\phi)^2}{(W_1^2 + W_2^2)\lambda^2} \right) \qquad 2\text{-}7$$

where W_1 and W_2 are the beam radii of the Gaussian beams, n is the reflective index of the core, and λ is the wavelength of the light. When we add a factor (1 %) representing the refection from the fibre-air interfaces and note that $W_1 = W_2$, the resulting coupling efficiency is

$$\eta = exp\left(-\frac{4(\pi n W_1 \varphi)^2}{\lambda^2} \right)\left(\frac{n-1}{n+1} \right)^2 \qquad 2\text{-}8$$

A 4° angle-polished fibre end has a measured coupling efficiency of the back reflection of –32 dB, which is in fair agreement with the calculation (-35 dB) (Marcuse, 1977).

The use of angled fibre reflection in the telescope as the local oscillator has the advantage that the signal beam propagates in the same direction as that of the local oscillator within the system.

2.3 Atmospheric lidar

In the past, to obtain a better signal to noise ratio, a differential Doppler technique has been proposed as a configuration to measure wind speed (Bilbro *et al.*, 1984). But this technique only allows the measurement of wind speed at one spatial

location. Recently, a modified reference beam technique that utilises a pulsed measurement beam has been demonstrated for wind measurements.

In the following sections systems suitable for wind measurements, the atmosphere Doppler lidar, the edge technique Doppler lidar, and the pulsed Doppler lidar will be discussed. More recently, Dorrington *et al.* (2001) have proven that a low coherent long-range lidar system using reference beam storage is a valid concept for atmospheric Doppler velocimetry. This new design will be covered as well.

2.3.1 Atmosphere Doppler lidar

Figure 2.12 depicts a typical optical arrangement for atmosphere Doppler lidar. The laser light is passed through a beam splitter and is divided into two beams. One beam acts as a measurement beam propagating into the atmosphere. The back-scattered light is collected by a telescope and is then optically mixed with the reference beam at a beam combiner. A focusing lens is used to concentrate the signal onto the detector. The back-scattered light level from each object or particle is proportional to its cross-sectional area, the incident light level and the scattering efficiency, which depend on the particle size, shape and composition.

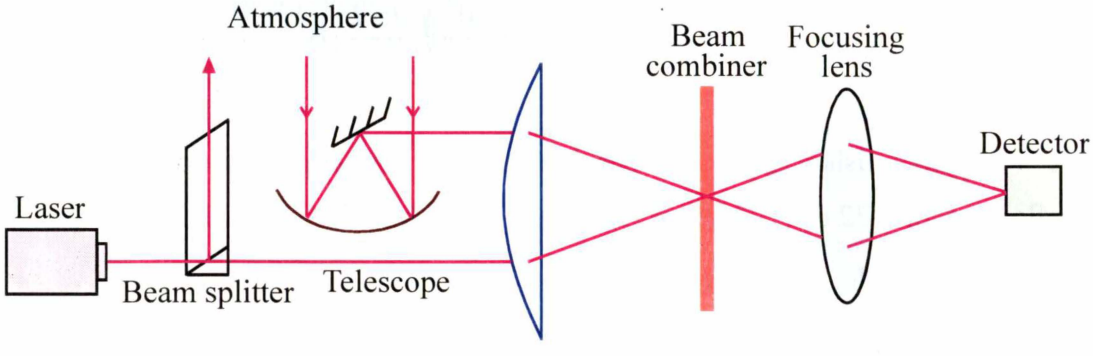

Figure 2. 12 - Optical arrangement for atmosphere Doppler lidar.

For applications near the earth's surface, where aerosols are abundant, aerosol scattering returns a larger signal at the longer wavelength. McGill and Spinhirne (1998) have proven that signals obtained from aerosol scattering have a considerably narrower spectral width than those from molecular scattering, which is susceptible to thermal broadening. In the upper atmosphere however, there are few aerosols, and molecular scatter based systems are often more appropriate.

For a small scattering volume length the instantaneous Doppler shift is approximately proportional to the velocity value. The measurement error variances of the profiles of wind velocities depend on atmospheric turbulence and Doppler shift, which is described by Shelekhov (2000). Typical system parameters for a compact CO_2 pulsed Doppler lidar are a range of 3 km to 4 km (dependent upon atmospheric conditions) and velocity accuracy in the order of 0.50 m/s with 112 m range gates (Pearson and Collier, 1999).

2.3.2 Edge technique Doppler lidar

The edge technique Doppler lidar has been demonstrated by Henderson *et al.* (1993) who have used a pulsed 2 μm CO_2 laser system for wind measurements. Harris and Kavaya (1999) have employed a bi-static 1.55 μm continuous wave laser system. Korb *et al.* (1997) developed a Doppler lidar system using the edge technique to make atmospheric measurements as illustrated in Figure 2.13. The wind measurements are made by locating the laser frequency on the steep edge of a high spectral resolution optical filter. Small frequency shifts cause large changes in the measured signal because of the steep slope of the edge.

The laser signal is transmitted coaxially with the telescope and directed to a flat mirror. This mirror is mounted in a two-axis gimbals' mount to allow directional pointing of lidar.

The scattered light from the atmosphere is collected by the telescope and directed through the edge-detector. The central fringe of a Fabry-Perot etalon is used as a high-resolution edge filter to measure the shift of the aerosol backscattered light, which has the original sharp spectral distribution of the laser. Various other filters with sharp spectral edges could be used. These include gratings, prisms, Michelson or Mach-Zehnder interferometers, and molecular or atomic absorption lines. The Doppler shift is determined from a differential measurement of the frequency of the outgoing laser pulse and the frequency of the backscattered light from the atmosphere.

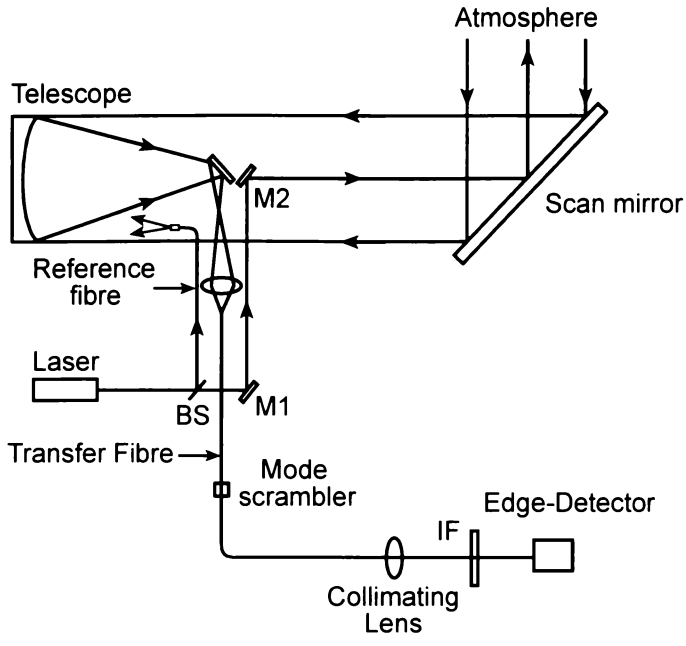

Figure 2. 13 - Diagram of optics used in the edge technique lidar experiment: BS, beam splitter; M1 and M2, mirrors; IF, bandpass interference filter.

2.3.3 Pulsed Doppler lidar

Generally, pulsed Doppler lidar is a reference beam configuration. Figure 2.14 illustrates a typical arrangement that uses a pulsed measurement beam and a CW reference beam. This allows measurements at multiple ranges along the direction of propagation.

The distance travelled by the laser pulse is a function of the time since departure, and therefore scattered light received by lidar at a specific time can be related to a particular distance. The scattered light returns continuously as long as the measurement pulse propagates through the scattering media. A second CW laser used as a local oscillator is required with which the collected light is mixed.

The local oscillator laser must remain coherent with the transmitted pulse over very long path length differences. Practically, a single frequency laser must be used. A portion of the local oscillator laser light is used to injection-lock the pulsed laser. An acousto optic modulator (AOM) is often used to apply a frequency offset to the injection beam before it is directed into the pulsed laser. A telescope is used to collect the backscattered light. Optical mixing of the reference beam and the received light is performed at a beam combiner.

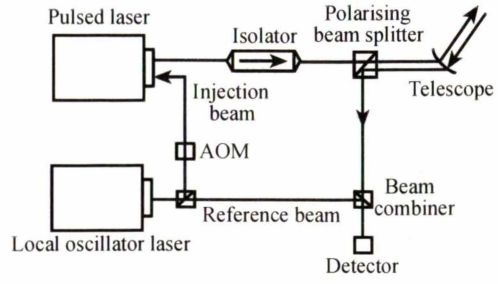

Figure 2. 14 - A typical pulsed Doppler lidar optical arrangement.

A method to obtain high repetition rate, stable, pulsed laser output is 'mode locking'. Coupling the modes of a laser and locking the phases to each other attain the pulsed laser action. When the phases of these components are locked, they behave like the Fourier components of a periodic function and therefore form a periodic pulse train (Saleh and Teich, 1990). The most direct method of obtaining this light is to use a multimode continuous wave laser and an internal modulation process to transmit light only during short time intervals (Post and Cupp, 1990).

2.3.4 Reference beam storage loop

The commercial viability of lidar systems is limited by the high cost and large size, mainly due to the injection locked laser systems currently used. In order to reduce the cost and size, the low coherence lidar concept (Dorrington *et al.*, 2001) has been introduced which requires only one pulsed laser as the source for the measurement and reference beam. Figure 2.15 illustrates the technique.

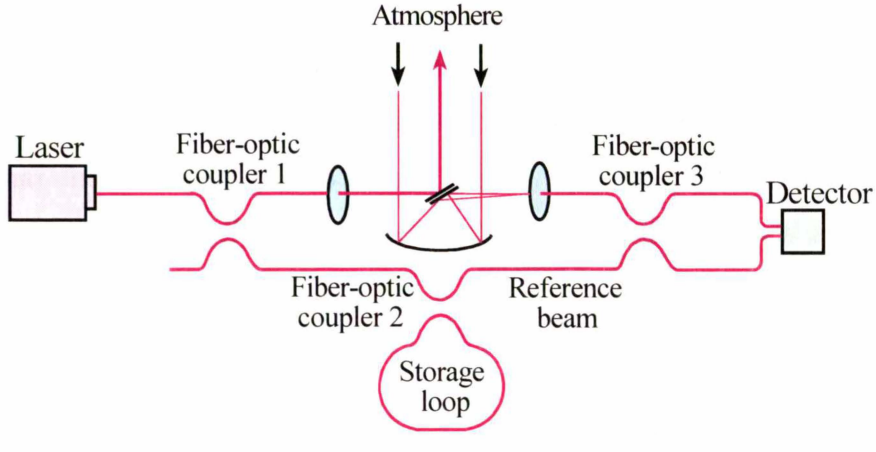

Figure 2. 15 - Optical arrangement of the reference beam storage.

Fibre-optic coupler 1 splits the light from the pulsed laser source, with the majority of its power as the measurement beam, and the remainder as the reference beam. The measurement beam is then directed into the atmosphere through a telescope as with any other type of lidar. This telescope also collects the scattered, Doppler shifted light and directs it to fibre-optic coupler 3.

The reference beam output of coupler 1 is connected to the storage loop consisting of coupler 2 and a beam delay fibre (BDF). When entering coupler 2 for the first time, a portion of the light pulse is split off and becomes the stored reference beam in the loop, while the rest is passed to coupler 3. There is now a laser pulse inside the loop, and each time it passes coupler 2, a portion is split off and passed to coupler 3, while the rest remains stored in the loop.

To avoid the stored pulse interfering with itself the storage loop round trip time is designed to be longer than the pulse width of the signal laser. A single input pulse then generates an output pulse train that exponentially decays in amplitude at a rate dependent on the input/output-coupling ratio of optical coupler 2.

While the measurement beam propagates to the target and the scattered light returns to optical coupler 3 of the system, the reference beam propagates several times through the storage loop. As a result, the measurement and reference beams have travelled corresponding distances, much longer than the laser's coherence length, when they are mixed. The two beams remain coherent and generate a beat signal at the output of coupler 3.

A single-pulse only allows the measurement of wind speed at one spatial location, but multiple pulses allow measurements at various locations. A large number of output pulses is desirable and would ensure a long measurement range, but to achieve this, a very small coupling ratio is necessary at fibre coupler two.

2.4 Summary

Various lidar systems are used to determine the velocity of particles in the atmosphere. All of these utilize the effect that light scattered or reflected by a moving target is Doppler shifted. The methods use a coherent laser, which is focused onto a particular target area that scatters or reflects the light and causes the frequency shift

of the original laser signal. A photo detection system then collects the reflected or backscattered light to determine the target's velocity. This process is called Laser Doppler velocimetry and can be set-up in the dual beam, two scattered beam or the reference beam modes. All methods can be implemented to determine the velocity components in more than one direction.

A differential Doppler method is generally used to measure wind speed as it achieves a higher signal to noise ratio. Suitable systems for wind measurements include the atmosphere Doppler lidar, edge technique Doppler lidar, pulsed Doppler lidar, and more recently the low coherent lidar concept that uses reference beam storage.

Chapter 3

Amplified reference beam storage

A new lidar design philosophy in which the transmitted pulse is sampled and stored in a fibre optic ring resonator has previously been demonstrated. This system generates a reference beam which consists of a pulse train that has travelled a distance equivalent to the measurement beam's path, reducing the coherence requirements and allowing the use of cheaper, smaller, and lower coherence sources. However, this system is limited by the decay of the stored energy.

To progress the concept of reference beam storage towards a low cost, widely useable technique, the system must counteract decaying pulse amplitudes by use of some means of amplification. Inclusion of an optical amplifier, such as an erbium-doped fibre amplifier (EDFA), in the system is an obvious choice but requires transferring the existing concept from visible to infrared light, to the telecommunication wavelength range where optical components are readily available.

A significant improvement may be observed if a gain element is introduced into the storage loop. This would allow the use of high coupling ratios, such as 50/50, because any loss including output coupling can be compensated for by the amplifier.

Although optical amplifiers have been the aim of extensive research, particularly for telecommunication applications, this is the first reported use of an erbium-doped fibre amplifier within a storage loop to generate a coherent reference beam train, as far as the author is aware.

3.1 Goals of the experiment

The aim of this project is to design a new storage loop, which generates reference beam pulses that remain coherent and useable over a large number of passes through a reference beam storage loop. To achieve this aim we need to address the following questions:

- Can an infrared diode laser of 1550 nm replace a Helium-Neon laser of wavelength 632 nm?
- Can the infrared laser be pulse modulated by an acousto-optic modulator at about 200 MHz?
- Can all optical components be fibre pigtailed?
- Can an erbium-doped fibre amplifier be included into a fibre optics based storage loop?Will the erbium-doped fibre amplifier compensate the total losses?
- Will the reference pulses remain sufficiently coherent over a large number of passes through the erbium-doped fibre amplifier?

3.2 Fibre amplifiers

"Optical amplifiers based on rare-earth-doped fibres have been widely recognised as key devices for achieving high-performance, high capacity and long-distance transmission in optical fibre networks" (Bononi and Rusch, 1998, Bononi *et al.*, 1999). The erbium-doped fibre amplifier is today the most recognised and frequently used optical amplifier. Its technology and exceptional consistency make it the perfect element for optical fibre communication systems in the 1550 nm window, and the trouble-free availability and size of the material make it much more economic than other amplification sources such as gas discharges.

The erbium-doped fibre amplifier consists of a length of erbium-doped fibre, a wavelength division multiplexer (WDM), and a pump laser diode. The pump power and gain characteristics of the erbium-doped fibre amplifier depend on a number of device parameters such as erbium-ion concentration, amplifier length, core radius, and pump power (Agrawal, 1997). In our case, the pump power, amplifier length,

and core radius must be carefully selected to avoid the reference pulse train increasing exponentially in amplitude and to avoid free running laser oscillation.

3.2.1 Energy levels and pumping scheme of erbium-doped fibre

At room temperature the erbium-doped fibre amplifier is a three level system while it can become a four level system at liquid nitrogen temperature (Saleh and Teich, 1991). At low temperature the ground state splits into distinct energy levels. Figure 3.1 illustrates the three-level, Figure 3.2 the corresponding four level pumping scheme.

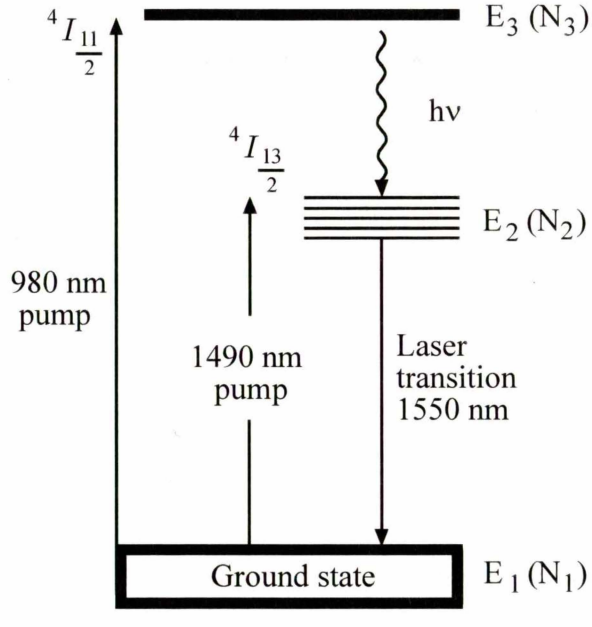

Figure 3. 1- Three level pumping scheme of Er^{3+}:silica (Yariv, 1997).

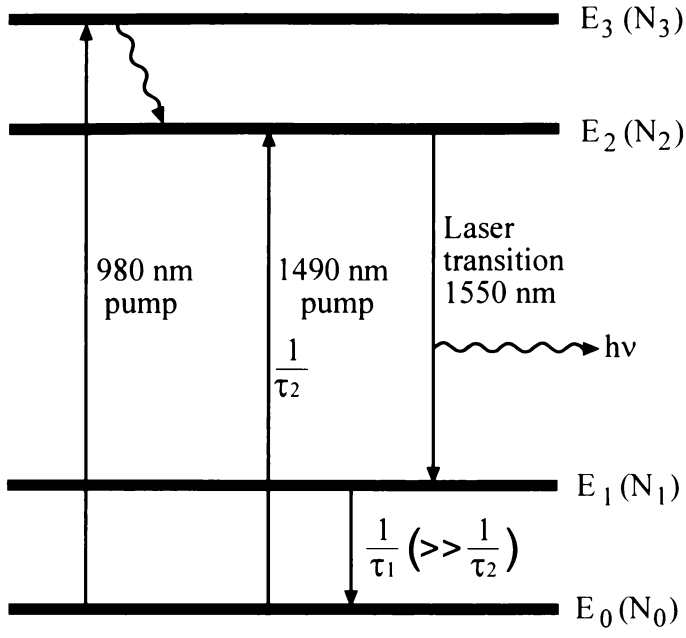

Figure 3. 2 - Four-level pumping scheme where N_i is the number of atoms in the energy level E_i (Saleh and Teich, 1991).

The population of energy levels 1 and 2 in thermodynamic equilibrium follows the Boltzmann distribution as

$$\frac{N_2}{N_1} = \frac{g_2}{g_1} exp\left(-\frac{E_2 - E_1}{k_B T}\right) \qquad 3\text{-}1$$

where N is the population density, E the energy, g is the degeneracy of the given energy level, T the temperature, and k_B the Boltzmann constant. At finite temperature and if the degeneracies are the same, $N_2<N_1$ if $E_2>E_1$. In order to obtain amplifier gain or lasing conditions a population inversion must be generated, $N_2>N_1$.

Luo and Chu (1997) described the three-level pumping of erbium-doped fibre lasers. The erbium-doped silica is pumped from its ground state, energy level 1 (0 in the four level case), to an excited state 3 by 980 nm pump radiation or to the top of the energy level group 2 by radiation of about 1490 nm. From level 3 the electrons rapidly decay to the long-lived level group 2 by non-radiative processes. They accumulate in level 2, and a population inversion is generated between levels 2 and 1.

The spontaneous lifetime of the level 2 group is around 10 ms. The lifetime can be changed by co-doping with other rare earth ions or by carefully choosing the doping concentrations.

Stimulated emission can take the electrons accumulated in the upper laser level (2) to the lower laser level (1). After this process another rapid, non-radiative decay occurs to the ground state 0.

Stimulated emission takes place around the 1550 nm wavelength. Other very similar, efficient four level laser systems are known, like for example Nd^{3+}:YAG However these materials operate only on one wavelength. Because of the rather broad energy level group 2 in Er^{3+}:silica the emission spectrum is very broad. When using erbium-doped fibre as an amplifier, spontaneous emission within this bandwidth is amplified along the gain medium (Barnes *et al.*, 1989). Amplified spontaneous emission will have a rather wide spectrum.

3.2.2 Pumping configurations and characteristics

An erbium-doped fibre amplifier can be pumped in either forward or backward or both directions simultaneously by using semiconductor lasers located at the fibre ends (Young, 1994). Figure 3.3 illustrates four pumping configurations: (a) forward or co-propagation, (b) backward or counter propagation, (c) bi-directional and (d) reflection pumping. The red, purple, and dark purple arrows indicate the direction of propagation of the pump, signal, and amplified signal light, respectively.

In each of the configurations the pump laser is coupled into the erbium-doped fibre by a wavelength division multiplexer. The wavelength division multiplexer is a bi-directional device, in which the pump signal can pass from port 1 to 3 and vice versa, the input signal from 2 to 3 and vice versa, no signal can pass from port 1 to port 2. Typical insertion losses are in the order of 1.0 dB.

In the forward pumping configuration the signal and pump laser light are propagating in the same direction, whereas in the backward pumping scheme the signal and pump are in opposite directions. Bi-directional pumping uses two lasers and wavelength division multiplexers at either end of the fibre. In the reflection-pumping scheme, the signal enters through a circulator. The erbium-doped fibre is forward pumped. The signal and pump light are reflected after the fibre by a mirror, which effectively results in additional backward pumping and additional signal amplification. The signal is then extracted from the amplifier by the circulator.

In (a), (b), and (c) pumping configurations isolators are used to block back reflection from the fibre ends and prevent pump laser light or amplified spontaneous emission going back to the signal source.

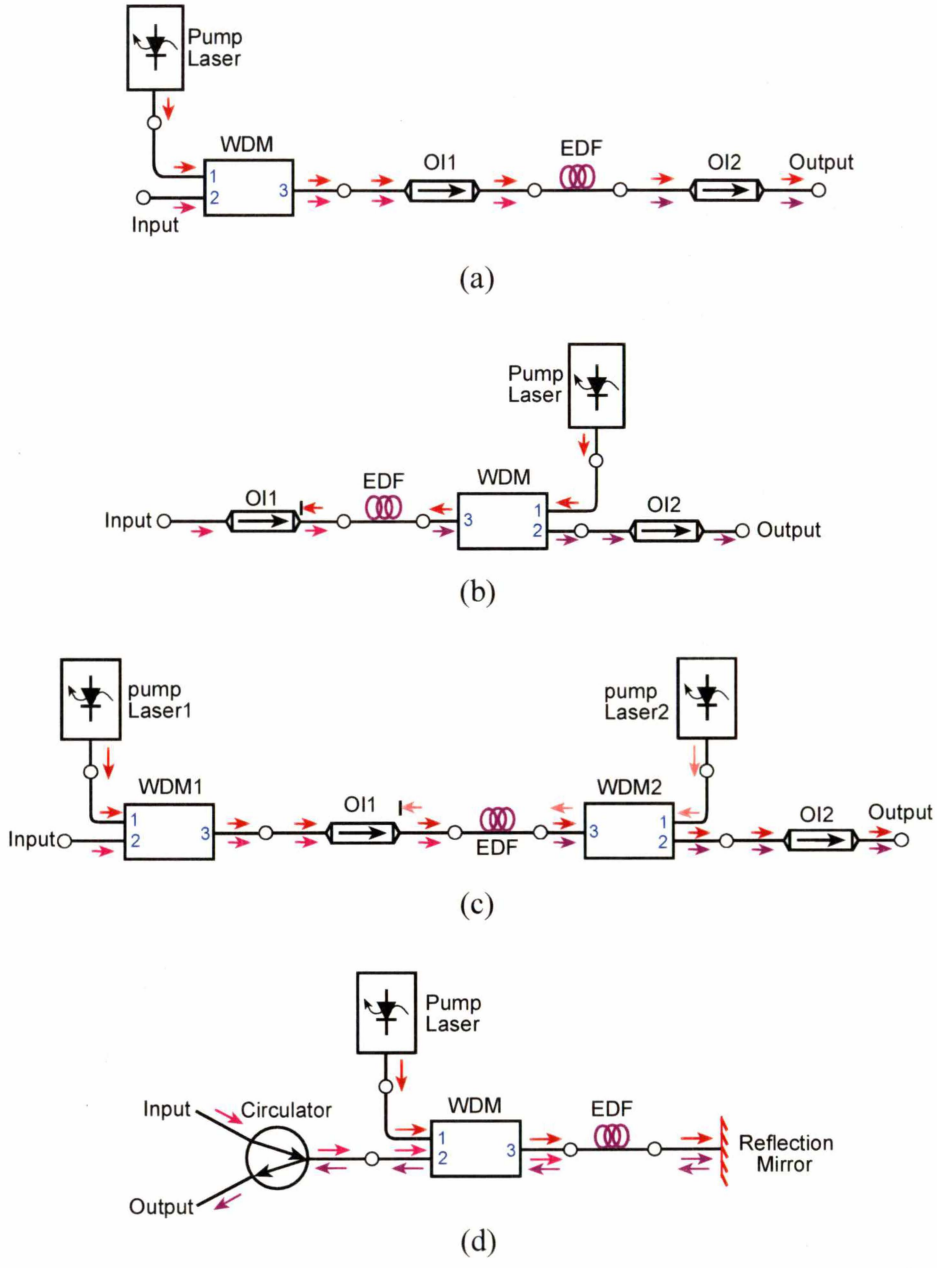

Figure 3. 3 - Pumping configurations (OI : optical isolator) (a) forward or co-propagation; (b) backward or counter propagation;(c) bi-directional and (d) reflection pumping.

Forward pumping is used for medium gain and low noise (preamplifier) applications; backward pumping is suitable for high gain and power amplifiers but has medium noise levels (Young, 1994). Bi directional pumping has moderately high gain and good noise level and is generally used for auxiliary amplifiers. The reflection

configuration is also used in auxiliary amplifiers but is not economic because of the expensive circulator. Bi-directional and reflection configurations are suitable for both, pre and power amplifiers.

3.2.3 EDFA gain characteristics

The energy diagram illustrated in Figure 3.1 and 3.2 leads to an absorption spectrum of erbium-doped fibre as illustrated in Figure 3.5. The diagram shows the absorption coefficient in dB/m of a typical fibre between 1450 and 1650 nm and the gain coefficient when pumping the fibre with 980 nm light.

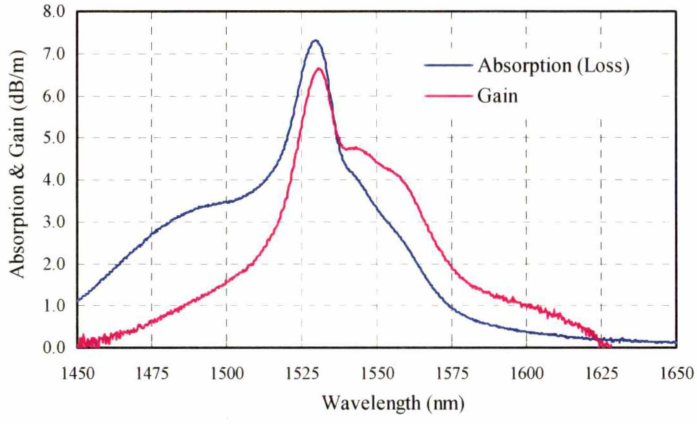

Figure 3. 4 - EDFA absorption and gain spectrum for 980 nm pump laser (FS-ER-7A28, Thorlabs, New Jersey, USA).

It can be seen that for wavelengths shorter than 1537 nm the fibre has a larger loss than gain; for wavelengths longer than 1537 nm, the situation is reversed, and hence signal amplification can occur.

The erbium-doped fibre is often pumped with a laser of about 1480 nm wavelength. However, more efficient pumping is possible using a laser operating near 980 nm where there is another strong absorption peak, not illustrated in figure 3.4.

The total gain of an EDFA is obtained by integrating over the length of the fibre.

3.2.4 Erbium-doped fibre amplifier noise characteristics

Amplifier noise depends on both the amplifier length and the pump power, just as the amplifier gain does. Generally, it is difficult to achieve high gain, low noise and high

pumping efficiency simultaneously (Giles *et al.*, 1991a). Amplified spontaneous emission travelling backward toward the pump and interfering with the signal imposes the main limitation. Noise is emanating from the combination of the signal and pumping power, known as beat signal noise. The problem of amplifier noise can be alleviated by inclusion of an optical isolator.

Low noise levels of erbium-doped fibre amplifiers make them an ideal choice for telecommunication system applications. In spite of low noise, the performance of long-haul fibre-optic communication systems employing multiple erbium-doped fibre amplifiers is often limited by the amplifier noise (Giles and DiGiovanni, 1990).

3.3 Fibre ring resonators

The reference beam storage loop is in concept very similar to a fibre ring resonator. Including an amplifier in the loop then makes the optical set-up similar to a fibre ring laser.

An optical fibre ring resonator, the optical counterpart of an electronic resonant circuit, can confine and store light at certain frequencies. A laser ring resonator is an optical resonator containing a medium that amplifies light. The ring resonator determines the frequency and spatial distribution of the laser beam. Chapter 5 will discuss the design philosophy of the amplified reference beam storage loop. Related, very similar set-ups from the literature will now be reviewed.

Figure 3.5 illustrates four typical optical resonators (a) planar-mirror resonator; (b) spherical-mirror resonator; (c) ring resonator and (d) optical-fibre resonator. These are different configurations for different purposes.

Obviously, the non-fibre resonators are not suitable for the amplified reference beam storage system. Only the optical-fibre resonators allow the erbium-doped fibre amplifier to be easily inserted into the amplified reference beam storage system. That is a length of erbium-doped fibre, a wavelength division multiplexer, and a pump laser. Various arrangements with optical fibre ring resonators have been reported that either generate or use pulsed light.

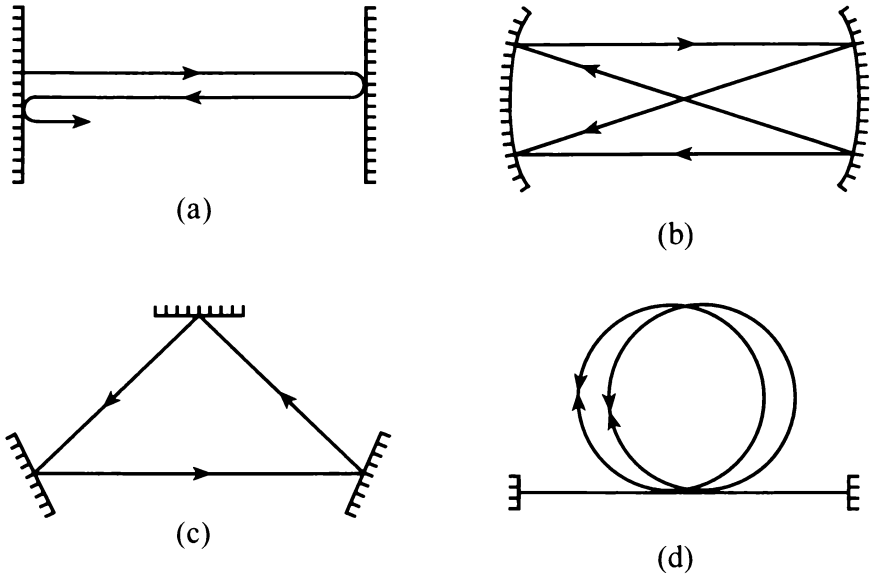

Figure 3. 5 - Four typical optical resonators (a) planar-mirror resonator; (b) spherical-mirror resonator; (c) ring resonator and (d) optical-fibre resonator.

3.3.1 Examples of pulse generation

A very simple set-up to generate laser pulses from a fibre loop has been reported. This set-up consists of a length of erbium-doped fibre, a wavelength division multiplexer coupler and a saturable absorber as presented in Figure 3.6 (Luo and Chu, 1999). The wavelength division multiplexer permits a high transmission of pumping power into the fibre ring resonator. The erbium-doped fibre laser has a high gain coefficient but has an unstable steady state region when combined with a saturable absorber, a second erbium-doped fibre with moderate absorption. This second fibre is included for its properties of nanosecond optical Q-switching and fast response time. This simple set-up is self-pulsing, capable of generating powerful, nanosecond optical pulses at wavelengths around 1550 nm.

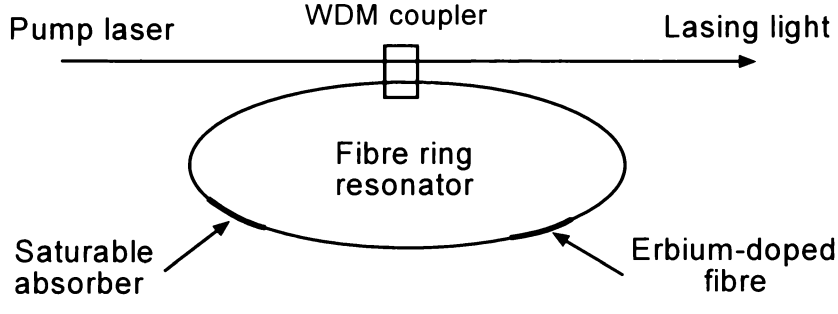

Figure 3. 6 - Schematic diagram of the fibre ring resonator.

Another common method to generate pulses is mode locking. Nakazawa *et al.* (1994) and Gupta and Novak (1997) have developed the harmonic modelocked fibre ring laser. Ahmed and Onodera (1996) have used the mode-locked ring laser to generate a high repetition rate optical pulse. Yoshida and Nakazawa (1996) have demonstrated repetition rates at 80 GHz to 200 GHz. A common problem in mode-locked fibre lasers is uneven pulse amplitude; generally the pulse height decays after some time. Doerr *et al.* (1994), Jeon *et al.* (1998) as well as Lee *et al.* (1999) have presented a semiconductor laser amplifier in a loop-mirror arrangement to solve the uneven pulse amplitude problem.

Amplitude equalisation of high repetition rate pulses generated in a rational harmonic mode-locked fibre ring laser was demonstrated by Li *et al.* (2001). The set-up is shown in Figure 3.7. In rational harmonic mode locking, the driving radio frequency does not match the cavity resonant frequency, resulting in severely uneven pulse amplitudes. The technique is based on non-linear polarisation rotation, where the rotation angle is proportional to the pulse peak power and the length of the fibre.

The gain of the fibre ring laser is provided by an erbium-doped fibre amplifier, which is pumped by a 980 nm laser diode. The pulse amplitude equalisation arrangement includes a polariser, three polarisation controllers and a section of dispersion-shifted fibre. The combination of these components and the control of the polarisation states of the polarisation controllers allow the generation of uniform amplitude optical pulses at high repetition rates.

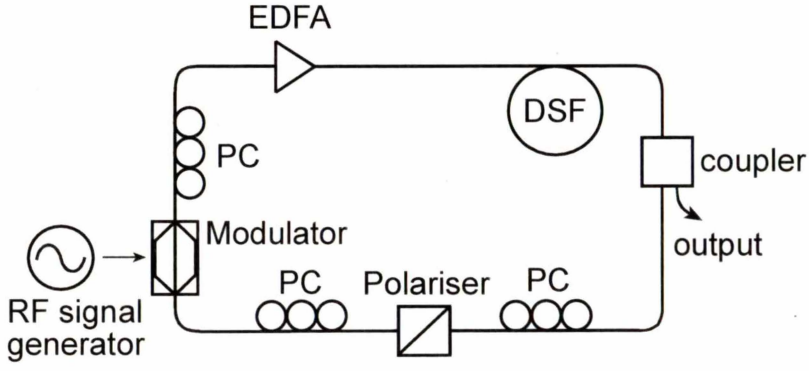

Figure 3. 7 - Schematic diagram of harmonic mode-locked fibre ring resonator.

The resonator for an erbium-doped, passively mode locked laser presented by Huve *et al.* (1999) is shown in Figure 3.8. The resonator consists of a length of erbium-

doped fibre, a wavelength division multiplexer, two polarisation controllers, a polariser, a length of standard single-mode fibre and an isolator. This method does not produce a single pulse per round trip; rather, most pulses are organized in bunches. Whatever the structure, it repeats at the cavity round trip frequency. Depending on the adjustment of the polarisation controllers the width, total number and the separation between pulses can be modified.

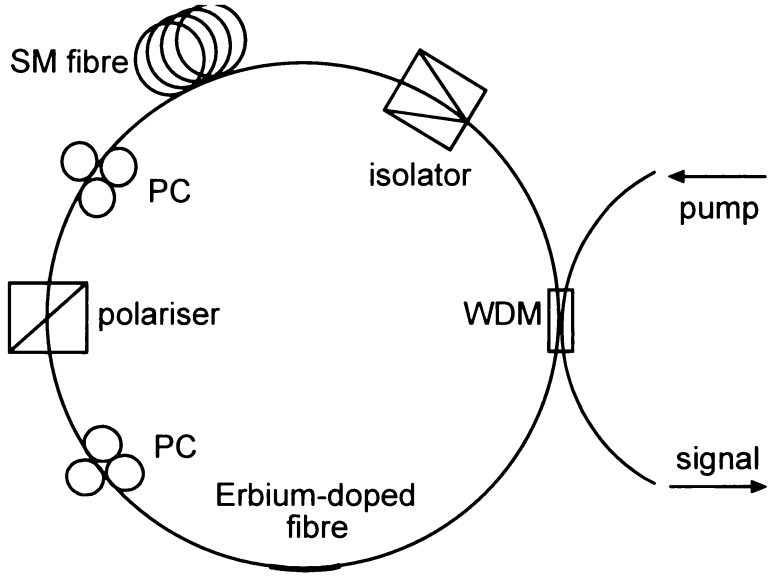

Figure 3. 8 - Schematic diagram of mode-locked fibre ring laser.

A different scheme to control the pulse amplitude is presented by Li and Chan (1999). A 1.0 m length of erbium-doped fibre is pumped by a 980 nm laser diode through a wavelength division multiplexer (Figure 3.9). A 1550 nm distributed feedback laser diode is used as a modulator. The gain of the cavity is highest at the distributed feedback laser frequency. Adjusting the roundtrip frequency to the driving frequency will make the fibre ring laser actively mode locked. This generates highly stable pulse trains at gigabit repetition rates, which are wavelength tuneable though the dc bias of the distributed feedback laser.

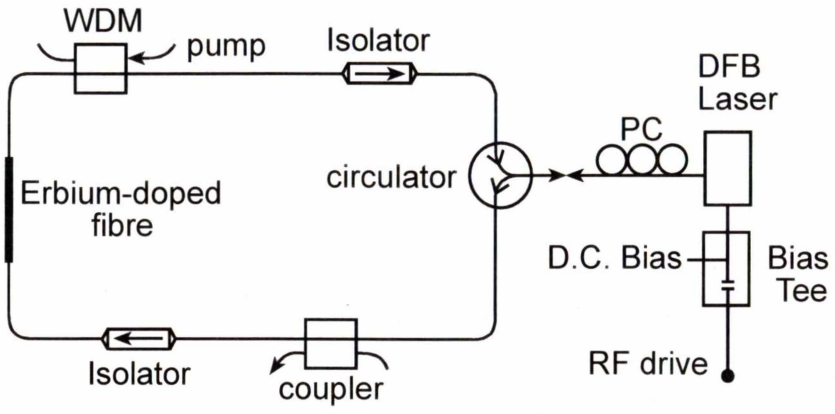

Figure 3. 9 - Configuration of mode-locked fibre ring resonator.

3.3.2 Examples of gain control

In the previous section we have reviewed free running lasers and methods to control their pulse amplitudes. However, in our application free running laser oscillation must be avoided. Only the stored signal should be amplified. Several methods of gain control have been reported in the literature.

One technique of obtaining erbium-doped fibre amplifiers with constant gain is using optical feedback (Zirngibl, 1991; Okamura, 1992; Massicott *et al.*, 1994 and 1996; Cai *et al.*, 1997). Optical feedback causes laser oscillation and will then clamp the signal gain at the threshold value. The optical feedback degrades noise figures because the population inversion is clamped at a low level. A problem is that the amplifier cannot be used for signals close to the lasing wavelength, because it is then very difficult to separate these two frequencies. Cai *et al.*, (1997) have demonstrated an amplifier configuration that employed a counter-propagating ring resonator to overcome this problem, but the noise degradation still exists.

A conventional configuration of a gain-clamped erbium-doped fibre amplifier is shown in Figure 3.10. The input signal is passed to the erbium-doped fibre amplifier through a wavelength division multiplexer, and the amplified signal is output from a separate wavelength division multiplexer. Light is fed-back from a pumped erbium-doped fibre with a ring configuration. With the proper attenuation within the ring, oscillation will occur at the feedback wavelength, and the erbium-doped fibre amplifier gain is clamped at the threshold value. The signal gain is constant irrespective of the signal input power.

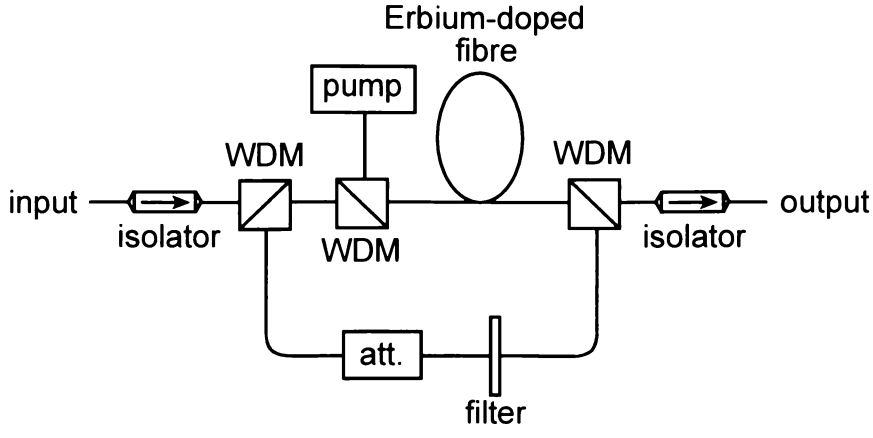

Figure 3. 10 - Conventional configuration of gain-clamped fibre amplifier.

A novel configuration presented by Kyo (1999a) uses a laser cavity formed by a fibre grating and a loop-mirror that contains an erbium-doped fibre amplifier in the loop (Figure 3.11). Two ports of a 3-dB coupler, (c) and (d), are connected to a fibre loop-mirror. Another port of the 3-dB coupler (b) is connected to a fibre grating through a wavelength division multiplexer and an attenuator. Pump light is input into the loop-mirror through the wavelength division multiplexer and activates the erbium-doped fibre in the loop. Port (a) of the 3-dB coupler is connected to a circulator, through which the signal enters and exits the loop-mirror.

Because the gain of the pumped erbium-doped fibre is clamped due to the laser oscillation, the signal gain is kept constant irrespective of the input signal power. The signal does not enter the laser cavity and thus does not disturb the cavity resonance even when its wavelength is close to or identical to the cavity resonance. A signal close to (but not exactly the same as) the cavity resonance wavelength can be amplified in the same way as signals far from the resonance. Therefore, wavelength-insensitive amplification is possible over a large wavelength range within the gain profile of the fibre.

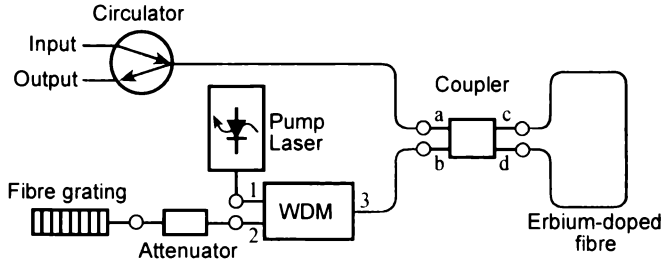

Figure 3. 11 - Configuration of gain-clamped fibre amplifier with a loop-mirror.

A ring resonator containing a pumped erbium-doped fibre and two circulators is presented in Figure 3.12 (Kyo, 1999b). A short length of erbium-doped fibre is attached in front of a gain-clamped erbium-doped fibre amplifier with a counter propagating ring resonator. The advantage of using a short length of pre-amplification fibre is that the noise figure is not degraded, and the gain is kept constant due to the gain clamped erbium-doped fibre amplifier in the main loop. The noise from amplified spontaneous emission is minimal because the preamplifier only generates a little noise, which is then further reduced by the filter in the loop. A drawback of this configuration is that it cannot be applied to a 980 nm pumping scheme because currently optical circulators do not operate on both the 1550 nm and 980 nm wavelengths.

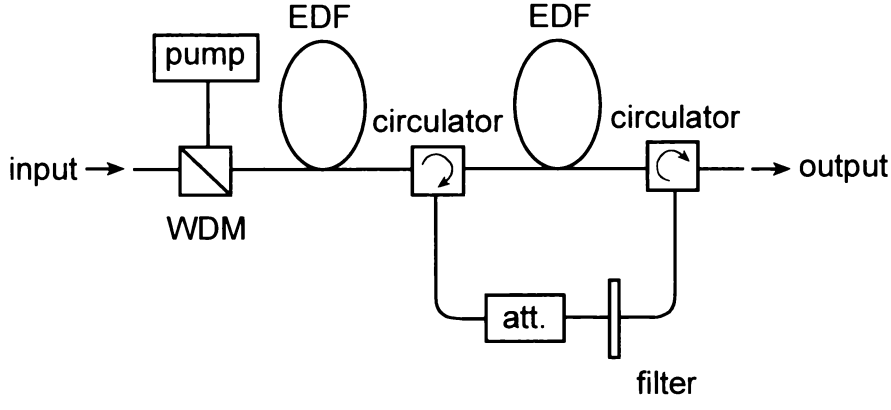

Figure 3. 12 - Configuration of gain-clamped EDFA with a counter propagating ring resonator.

Another approach to gain control is using several erbium-doped amplifiers in a cascade arrangement as shown in Figure 3.13 (Karásek *et al.*, 2000). The suppression of output power and signal to noise fluctuations is achieved by clamping the gain of the first amplifier using a ring laser configuration and propagating the signal through the cascade of erbium-doped fibre amplifiers. Each amplifier has a gain equalisation filter that perfectly equalises the gain for all signal amplitudes and wavelengths. However, this arrangement requires higher pumping power to maintain the gain of each amplifier, even when the erbium-doped fibre amplifiers are saturated by the propagating signal power.

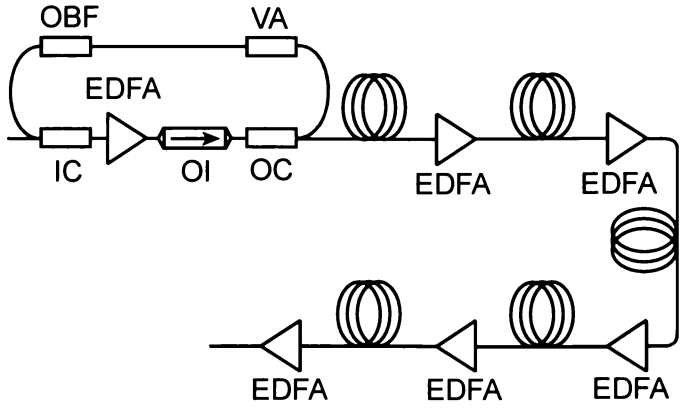

Figure 3. 13 - Schematic diagram of an EDFA cascade: OBF, optical bandpass filter; OI, optical isolator; VA, variable attenuator; IC and OC, input coupler and output coupler.

Today the erbium-doped fibre amplifiers are widely used in optical systems as power boosters, repeaters, and preamplifiers. Most differences in optical arrangements arise with different pumping directions (Kakinume *et al.*, 1990), multistage amplification (Masuda and Takada, 1990), optical circulators (Nishi *et al.*, 1990; Giles *et al.*, 1991a, 1991b) and so on. Less conventional devices include optical amplifiers with all-optical means of gain regulation (Zirngibl, 1991).

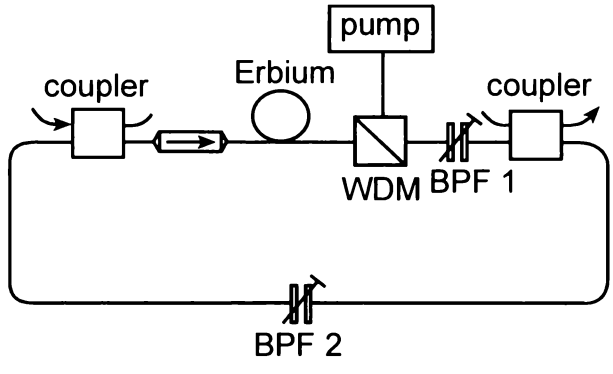

Figure 3. 14 - Schematic diagram of optically controlled fibre ring laser.

Fatehi and Giles (1996) have presented the modified optically controlled fibre ring laser shown in Figure 3.14. This design comprises of an erbium-doped fibre amplifier with optical feedback, creating an optically controlled ring laser whose frequency is defined by a bandpass filter. The signal enters the ring laser through the left coupler and regulates the saturation of the amplifier gain. The bandpass filters can be positioned either in the BPF1, to reject the signal, or in the BPF2 location, to pass the signal. Uses for this system include fault location, optical digital logic circuits and non-linear optical circuitry.

No technique is available which provides a long pulse delay time. However, an optical delay line can solve this problem (Jackson *et al.*, 1985; Taylor, 1990). A Sagnac interferometer incorporating a fibre optic recirculating-ring delay line with an erbium-doped fibre amplifier has been researched by Kringlebotn *et al.* (1995) (Figure 3.15). The design is used to improve the low frequency response by increasing the effective length of the Sagnac loop. The number of recirculations was increased by incorporating an erbium-doped fibre amplifier in the ring to compensate for both the coupling and intrinsic losses in the ring. However, the noise penalty of using a fibre amplifier in the ring is high, especially at low frequencies, so the advantage of using this design is limited.

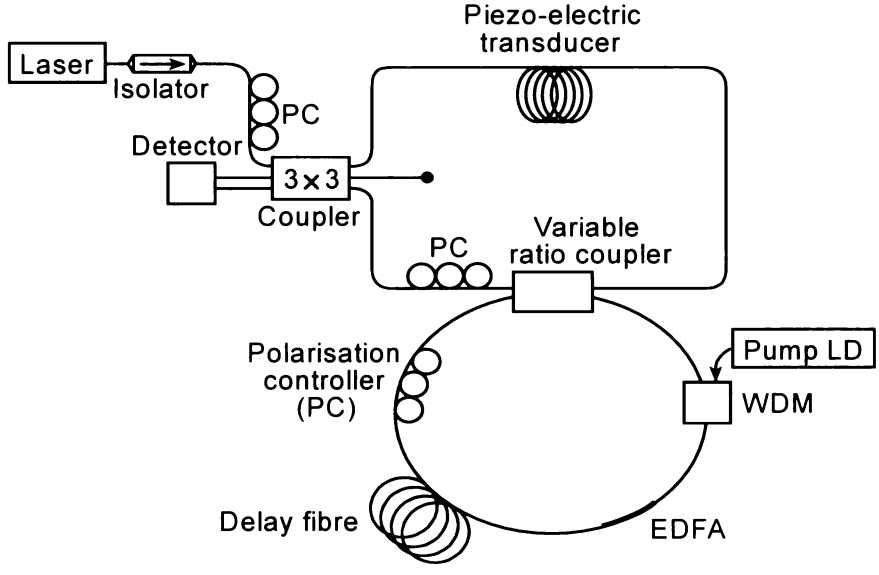

Figure 3. 15 - Schematic diagram of recirculating delay ring laser.

3.3.3 Cavity ring-down spectroscopy

A field of research that uses very similar optical arrangements to the reference beam storage loop discussed in Section 2.3.4 and also investigates the decay of pulse trains is cavity ring-down spectroscopy.

This method involves exciting a cavity and monitoring the decay time of the excitation. For a temporally narrow, pulsed excitation, this is achieved by observing the decaying pulse train using a fraction of the signal weakly coupled out of the cavity. The decay envelope of the pulses will depend on the total cavity loss, which

is caused by the optical components of the cavity as well as any absorbing test samples, like for example a gas cell inside the cavity.

Recently fibre systems have been used in cavity ring down spectroscopy. Brown *et al.* (2002) have demonstrated (Figure 3.16) that by measuring the ring-down times one can accurately determine the absolute transmission of an optical fibre and the losses of other components of the ring cavity. Pulsed, visible and near-infrared laser light is coupled into an optical fibre, which is wound into a loop using a fibre splice connector. The light pulses travelling through the fibre-loop are detected using a photo multiplier. The authors found that once the light is coupled into the fibre it experiences very little loss, and the light pulses do a large number of round trips before their intensity is below the detection threshold.

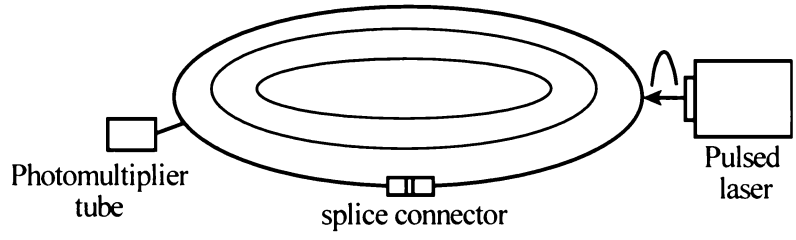

Figure 3. 16 - Schematic diagram of fibre-loop ring-down spectroscopy set-up.

Measurement of the loss-per-pass and the ring-down time allows for characterization of the different loss mechanisms of the light pulses in the fibre and splice connector. This method resembles "cavity ring-down absorption spectroscopy" and is well suited to characterize low-loss processes in fibre optic transmission equipment independent from power fluctuations of the light source.

Unlike with free space cavities, mode-matching optics is not required in the fibre loop system in order to excite only longitudinal modes. To attain a very high finesse, coupling into and out of the cavity must be extremely weak.

The optical arrangement for pulsed Doppler lidar in the current experiment, discussed in Section 2.3, is very similar. This storage loop is designed to have a round trip time slightly longer than the pulse length. An output pulse train generated by a single input pulse shows an exponential decay at a rate dependent on the cavity losses, which can be mainly attributed to the 50:50 fibre coupler.

Stewart *et al.* (2001) have presented a fibre optic system for cavity ring-down spectroscopy, which contains a length of erbium-doped fibre pumped at 980 nm (Figure 3.17). The gain can be adjusted below or above threshold. The fibre loop is constructed from standard fibre optic components and includes a micro-optical gas cell. The set-up is intended for measurement of trace gases, which possess near-IR absorption lines within the gain bandwidth profile of the erbium fibre amplifier. Ring-down times of several microseconds can be obtained, which can be altered through adjustment of the attenuation or gain factor of the loop. It is not necessary to have very high quality output couplers to obtain long ring down times.

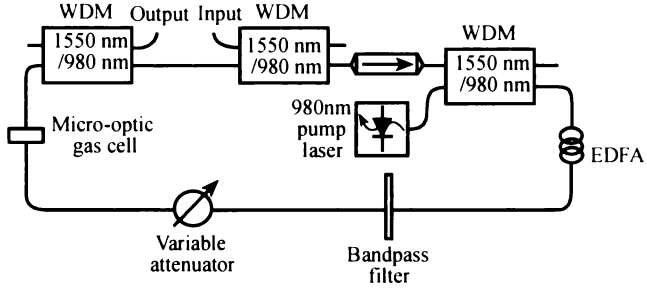

Figure 3. 17 - Schematic diagram of the fibre optical system for ring-down and laser intra-cavity loss measurements.

The new storage loop design that will be presented in Chapter 5 is similar to Figure 3.17 and is based on the concept of using an erbium-doped fibre amplifier inside the storage loop.

Chapter 4

Signal processing

The back-scattered Doppler signal is very weak and for a pulsed system is only present during very short Doppler bursts. In addition to powerful light collection optics, sensitive signal processing methods are required to enhance the signal. The following chapter presents an overview of the signal processing methods used to enhance the experimental data of this work. This chapter covers phase-locked loop demodulation and the discrete wavelet transform both used to reduce the noise of the output burst signal. Finally, the last section will briefly mention the Fourier transform which is used to convert the signal from the time to the frequency domain.

4.1 Phase-locked loop demodulation

Generally optically measured signals scattered back from a target are very weak and unstable, making it difficult to determine the signal among the noise. A large amount of noise will be generated by additional scattering of the Doppler signal along the detection path through the atmosphere and will interfere with velocity calculations. This is the optical equivalent to multipath interference encountered in conventional radio communications. Clark and Moir (1997) have shown that the signal to noise ratio of modulation techniques such as amplitude, frequency or phase modulation can be improved, but there are still some noise problems.

Doppler velocimetry (LDV) to measure vibrations of a target has been a well-established technique during the past thirty years. Only recently the noise problems encountered in this method have been improved by the use of phase lock techniques (Kim and Ha, 1999), which are now very common tools in digital communications.

4.1.1 Introduction

Using modulation techniques a signal can be shifted from its baseband to very high frequencies, which are not affected by the low frequency noise (1/f noise) shown in Figure 4.1. Using the appropriate demodulation method the signal can be recovered without having picked up much noise.

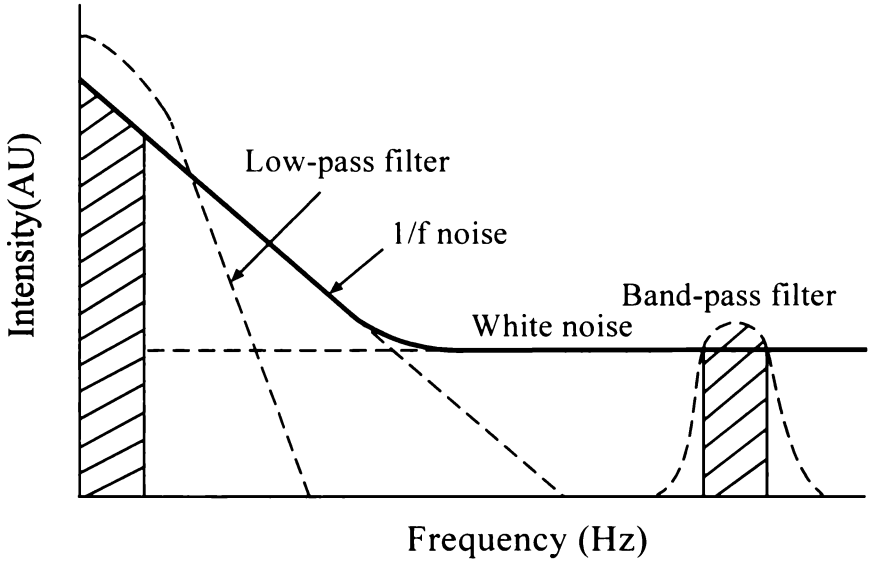

Figure 4. 1 - Signals with and without modulations.

Without modulation we need a low pass filter to deal with the noise. We might use a filter with frequency selectivity, Q, of around 100 for a signal at 400 Hz. However, by adopting a modulation technique the Q variable becomes significantly greater, of the order of $3x10^5$ for 120 MHz carrier frequencies.

In telecommunication systems phase and frequency modulation have become very significant, but there are still various noise problems that are very hard to combat. Clark and Moir (1997) have proven that a phase-locked loop demodulator can overcome many of the noise problems. The phase-locked loop demodulator has been incorporated into the system demodulator to improve very weak signals, to reduce strong noise and to increase the Q values. The phase-locked loop can be applied in modulators, demodulators, frequency synthesiser, multiplexers and various signal processors.

4.1.2 Amplitude and phase modulation

Suppose we have a continuous wave signal, *V(t)*, where, *a(t)* is the amplitude of the signal and *θ(t)* the phase angle:

$$V(t) = a(t)\cos(\theta(t)) \qquad 4\text{-}1$$

In a phase modulation system we consider *a(t)* as a constant, but *θ(t)* will vary with the signal, *f(t)*,

$$\theta(t) = \omega_c t + k_p f(t) + \theta_0 \qquad 4\text{-}2$$

where ω_c is the carrier frequency, k_p is the phase modulation constant, and θ_0 is the initial angle. If the signal *V(t)* is changed by the modulated frequency, we have the frequency modulation formula

$$\theta(t) = \omega_c t + k_f \int_0^t f(\tau)d\tau + \theta_0 \qquad 4\text{-}3$$

where k_f is the frequency modulation constant. If *f(t)* is a square or sine wave as illustrated in Figure 4.2, then $V(t)_{PM}$ and $V(t)_{FM}$ are the corresponding phase modulation and frequency modulation signals.

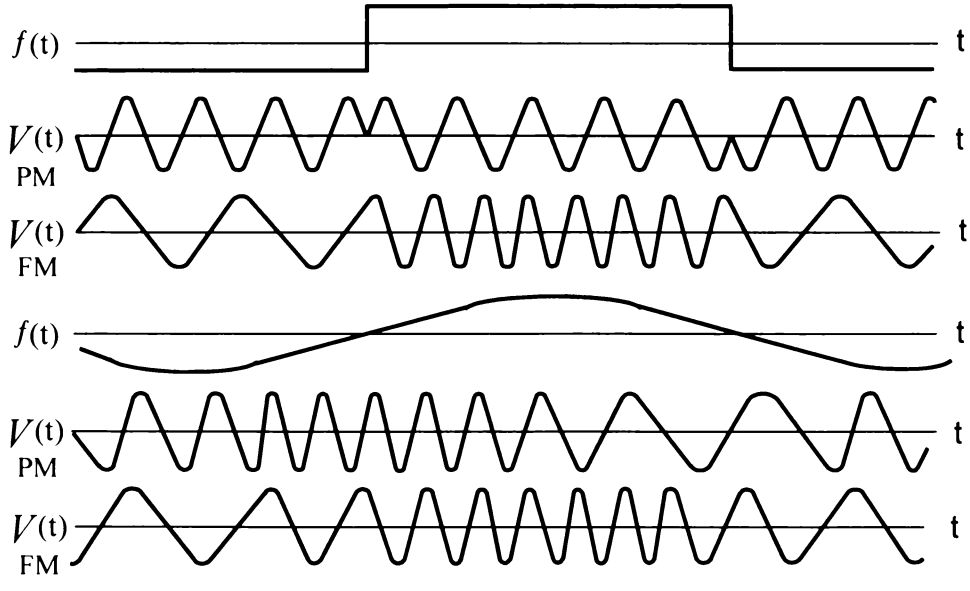

Figure 4. 2 - Examples for phase and frequency modulation.

4.1.2.1 Phase-locked amplifier

The phase-locked amplifier consists of a phase sensitive detector and a narrow band-pass filter shown in Figure 4.3. The phase sensitive detector includes a mixer and a low pass filter. This is the heart of the phase-locked loop demodulator. The phase sensitive detector can identify the phase difference between the input signal and the reference signal.

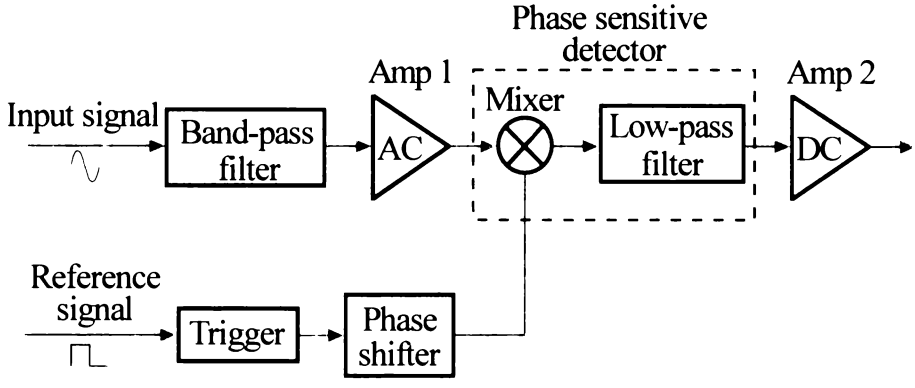

Figure 4. 3 - Block diagram of the phase-locked amplifier.

If φ_s is the signal phase, a_s the signal amplitude, and φ_r and a_r the reference phase and amplitude respectively, then the output of the phase sensitive detector, V_0 is

$$V_0 \propto a_r a_s \cos(\varphi_s - \varphi_r) \qquad 4\text{-}4$$

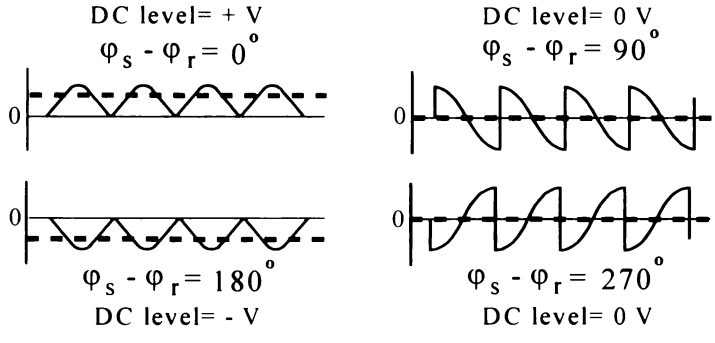

Figure 4. 4 - Output waveforms of phase sensitive detector.

Figure 4.4 shows the signal after the mixer (pink line) and the detector DC output (dashed line), which varies with the difference between φ_s and φ_r. For a phase difference of 0° the DC level is positive, for 180° it is negative, and for 90° or 270° it is 0 V. This pattern repeats with multiples of 2π of the phase difference.

4.1.3 Phase-locked loop

A phase-locked loop consists of a phase sensitive detector, a voltage-controlled oscillator, and a low-pass filter (Figure 4.5).

If the angular frequency, ω_i, of the input signal, v_i, is different from the frequency, ω_o, of the voltage controlled oscillator, an error signal, v_o, is produced which is fed back to the voltage controlled oscillator until $\omega_i \approx \omega_o$. If K_d is the gain of the phase sensitive detector and K_c is the gain of the voltage-controlled oscillator, then the total loop gain is given as

$$K_t = K_d K_c \qquad 4\text{-}5$$

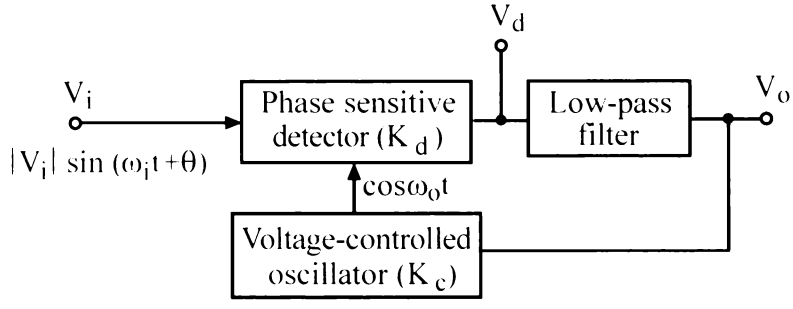

Figure 4. 5 - Basic diagram of the phase-locked loop.

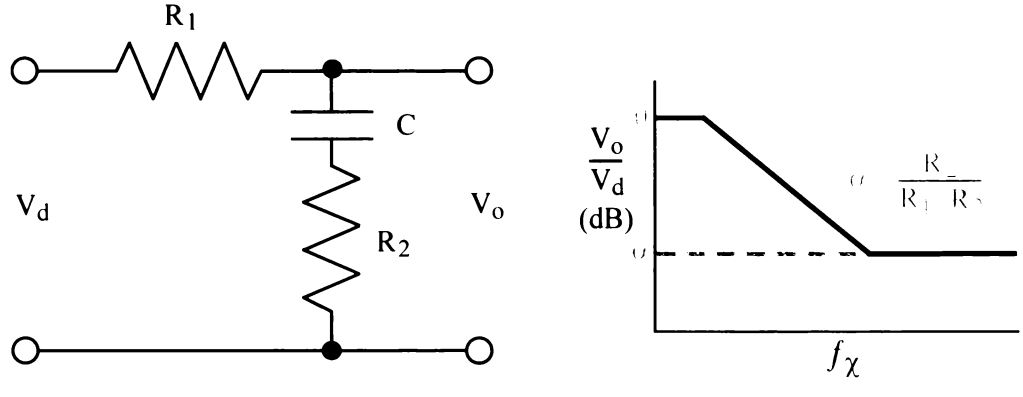

Figure 4. 6 - The circuit and frequency response of low-pass filter for the phase-locked loop.

Since the phase-locked loop uses a low pass filter, this affects the stability of the loop and lowers the frequency response shown in Figure 4.6. Within the phase-locked loop we have two important variables:

$$\Delta f_H = \pm \frac{K_t}{2\pi} \qquad 4\text{-}6$$

$$\Delta f_C \approx \frac{1}{2\pi}\sqrt{\frac{K_t}{CR_1}} \qquad 4\text{-}7$$

Δf_H is called the holding range and Δf_C the capture range (Best, 1984; Kim and Ha, 1999). In the frequency locked status the input frequency, ω_i, and the oscillator frequency, ω_o, are approximately equal. From Equation 4.3 and the voltage controlled oscillator characteristics we know

$$\omega_i = \omega_c + k_f f(t) \qquad 4\text{-}8$$

$$\omega_o = \omega_{oo} + k_o V_o(t) \qquad 4\text{-}9$$

where ω_c is the carrier frequency, $f(t)$ is the modulating signal, ω_{oo} is the voltage controlled oscillator free-running frequency and k_f and k_o are constants. The phase lock loop output then is

$$V_o(t) = \frac{k_r}{k_o} f(t) + \frac{1}{k_o}[\omega_c - \omega_{oo}] \qquad 4\text{-}10$$

Equation 4.10 illustrates that the output of the phase locked loop and the modulating signal have a linear relationship. The DC term disappears when $\omega_c = \omega_{oo}$. In practice, a series capacitor is added to block the DC level at the phase lock loop output.

4.1.4 Phase-locked loop demodulation

In high-speed digital communications, like for example optical fibre communications, phase lock loop demodulation is frequently used. A common method to reduce noise is to combine a phase sensitive detector with a phase lock loop circuit. The signal is multiplied with the output of a precise oscillator, which converts the high frequencies into intermediate frequencies and the small frequency variation to a more convenient range. A phase lock loop is connected to this circuit. The phase locking in the low frequency range provides increased noise reduction (Shirahama *et al.*, 1995).

Figure 4.7 is a block diagram of this arrangement. The input signal has a frequency $f_1 \pm f_d$, which consists of the carrier, f_1, and a small modulation frequency, f_d. In our experiments this modulation would be the Doppler shift imposed on the signal. There

will be significant high frequency as well as low frequency noise, $f_{HFnoise}$ *and* $f_{LFnoise}$, present in the signal.

The second input to the circuit is the carrier frequency, f_1. There are two mixers that are used in this system to merge the signals. Mixer 1 combines the input signal with the frequency, f_L, of a very stable and precise crystal oscillator. This signal is then directed into a band-pass filter with a centre frequency $f_1 + f_L$ and bandwidth $2f_d$. The output from the filter is mixed with the carrier signal, and then passed through a second band-pass filter centred at f_L. The bandwidth of this filter is $2f_d$. This phase lock loop will remove the high frequency noise and only low frequency noise, $f_{LF,noise}$, will be present in the signal centred at the crystal oscillator frequency. The signal is then locked onto by the phase-locked loop and its V_d output (Figure 4.5) is used for further processing. The synchronous detection further reduces the low frequency noise component.

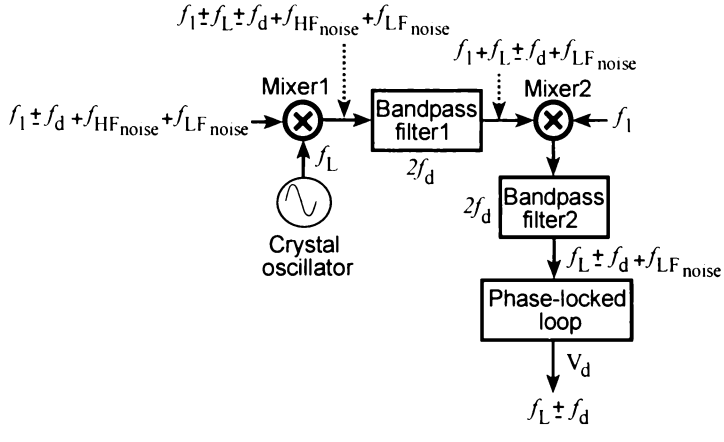

Figure 4. 7 - Block diagram of phase-locked loop.

4.2 One-dimensional discrete wavelet transform

In the previous section, we have used synchronous detection to reduce high frequency noise and a phase-locked loop demodulation to reduce low frequency noise. But as the noise is not totally eradicated, it is difficult to convert the signal from the time domain into the frequency domain, especially when the noise is getting higher. In addition to this hardware solution further signal processing can be applied on the computer. The one-dimensional discrete wavelet transform (Microsoft Corp.,

Autosignal v1 software, Appendix II, Code-1) can be used to reduce noise in the time domain at certain level.

A wavelet analysis is applied to the signal that is coming from the phase lock loop to detect its self-similarity (Mallat, 1998). Then a discrete wavelet transform of the one-dimensional signal is performed, and the result used to de-noise the signal.

Using the Symlet Wavelet transform the signal is decomposed into wavelet coefficients. To extract these coefficients we can pass the original signal through a pair of complementary low-pass and high-pass filters. The low-pass filter yields 'the first level approximation signal' and the high-pass filter yields 'the first level approximation noise'. However, the new signals are over sampled; each approximation signal and approximation noise has the same number of data points as the original signal, so there are now twice as many data points in the analysis. This is more information than is required to represent the signal.

To reduce the number of the data points, we can down sample the approximation signal and approximation noise after filtering, for example by discarding every second data point. We end up with the same number of data points as the original signal, and if we choose the right filters we can down sample without losing any information. This filtering and down sampling yields 'the first-level signal coefficients' and 'the first-level noise coefficients '.

So far, the high-frequency noise of the original signal is primarily captured in the 'first-level noise coefficients', while the 'first-level signal coefficients' capture the low-frequency information and contain much less noise. If needed, we can repeat the filtering and down sampling on the 'first-level signal coefficients' to yield the 'second level signal coefficients' and 'the second level noise coefficients ', and so on until we yield signal and noise coefficients, which represent the signal to noise ratio we want.

If we continue to filter and down sample each successive level coefficient, we increase the scale by a factor of 2 at each level of analysis. At level 1 we yield wavelet coefficients at a scale of 2 or a time window of 2; at level 2 we yield wavelet coefficients at a scale of 4 or a time window of 4, and so on. Thus, the

discrete wavelet coefficients are a function of the scale and position of the fundamental analysing wavelet.

Therefore, wider time windows yield better large scale and low frequency information; narrower time windows yield better small scale and high frequency information. In other words, the low frequency information, slow variation, is used as coarse resolution, wider time window; the high frequency information, fast variation, is used as fine, small-scale resolution and finer time window.

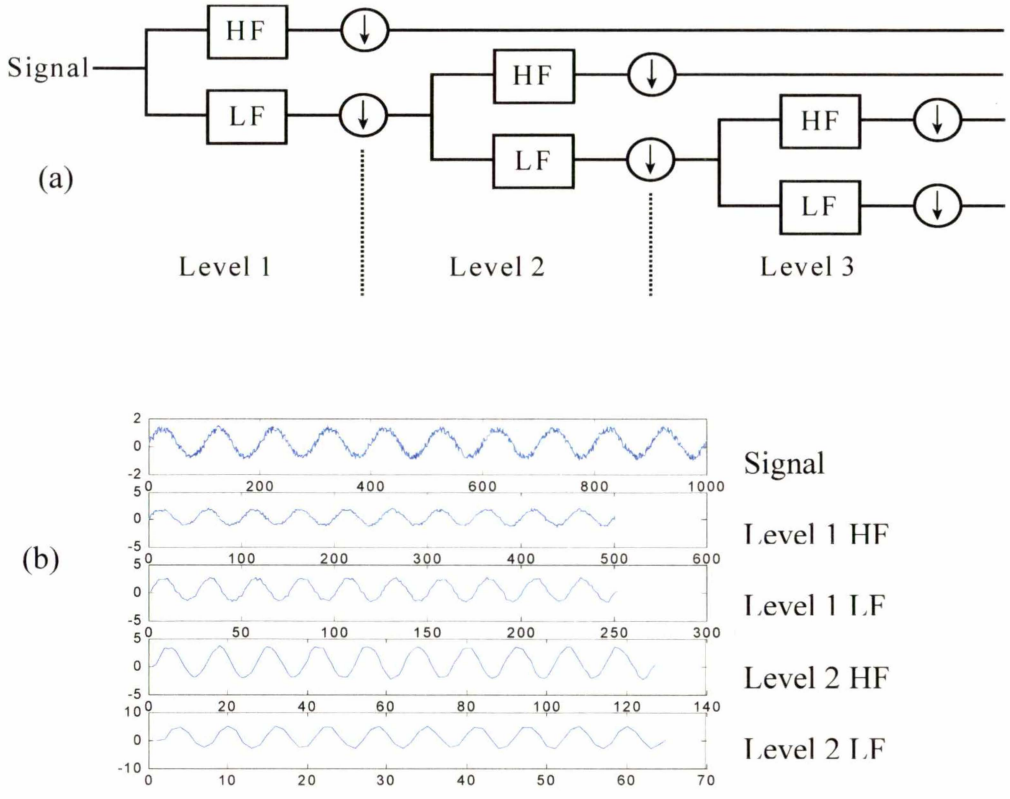

Figure 4. 8 - (a) Wavelet decomposition tree (b) Signal waveform output by using wavelet decomposition for HF and LF of level 1 and level 2.

Using this successive filtering process, the signal is broken down into many lower-resolution components. The process is described by the wavelet decomposition tree as shown in Figure 4.8 (a), which can be plotted as a wavelet coefficient plot for each level. Figure 4.8 (b) shows the signals of level 1 and level 2 after decomposition. Looking at a plot of a signal's wavelet decomposition tree can yield valuable information about the nature of the signal itself.

Next, the coefficients are modified using a wavelet shrinkage technique that removes all low-energy coefficients below a threshold. Then, using the inverse

discrete wavelet transform, a synthesized signal that is the de-noised version of the original signal, is reconstructed from the modified wavelet coefficients.

To de-noise a signal, we remove small-valued coefficients so that the reconstructed signal has less noise. The process of down sampling may introduce distortion into the filtered signals. However, when the appropriate decomposition and reconstruction filters are used, the distortion of down sampling is cancelled out, and it is possible to reconstruct the original signal.

4.3 Fourier transform

The Fourier transformation is an algorithm that breaks a signal into constituent sinusoids of different frequencies. It is a mathematical technique for transforming our view of the signal from the time domain to the frequency domain. For a continuous function of one variable f(t), the Fourier transform F(f) is defined as:

$$F(f) = \int_{-\infty}^{\infty} f(t) e^{-j2\pi ft} dt \qquad 4\text{-}12$$

where f is the frequency and t the time. A computational method to carry out this transformation is the Discrete Fourier Transform (DFT), which can be applied to a set of sampled data points. Consider a complex series f_k of N samples

$$f_0, f_1, f_2, f_3, \cdots, f_k, \cdots, f_{N-1} \qquad 4\text{-}13$$

where f_i is sampled at a certain point in time, t_i. Further, assume that the series outside the range 0, N-1 is extended N-periodic, that is, $f_k = f_{k+iN}$ for all k and i. The Fourier transformation, F_n, of this series also has N values:

$$F(n) = \frac{1}{N} \sum_{0}^{N-1} f(k) e^{-jk2\pi n/N} \quad \text{for } n=0...N \qquad 4\text{-}14$$

The signal should be sampled at a rate of least twice the Nyquist frequency. This is the highest frequency component that should exist in the input series for the DFT to yield "uncorrupted" results. More specifically if there are no frequencies above the Nyquist frequency the original signals can be exactly reconstructed from the samples.

In practice, however, signals are time limited, not band limited. As a result, determining an adequate sampling frequency, which does not lose desired information, could be difficult. When a signal is under sampled, the higher and lower order DFT spectra are overlapping, and it is no longer possible to recover *f(t)* from the sampled signal. The over sampled signal reaches zero very quickly. Much of its spectrum is zero and is not needed to reconstruct the original *f(t)*. The lower and higher order spectra of a critically sampled signal reach zero at their ends. The data in the spectrum of the critically sampled signal is just sufficient to reconstruct the original.

In the transformation process, the time information of the signal is lost. However, the Doppler bursts we are dealing with are not stationary; they contain numerous non-stationary or transitory characteristics. Along with the frequency of the burst, the points where they begin, end or change also provide meaningful information.

There is always a trade-off between the precision of the time-based information and the precision of the frequency-based information. The frequency resolution is determined by the size of the time window, and must use the same fixed time window for all frequencies.

Chapter 5

System design

A new lidar design philosophy (Dorrington *et al.*, 2000) in which the transmitted pulse is sampled and stored in a fibre optic ring resonator has been discussed in section 2.3.4. This approach uses a reference beam which consists of a pulse train that has travelled a distance equivalent to the measurement beam's path length, reducing the coherence requirements and allowing the use of cheaper, smaller and lower coherence sources. However, as demonstrated (Dorrington et al., 2000) this system is limited by the decay of the stored energy. We have further developed this concept to include an erbium-doped fibre amplifier inside the storage loop to compensate for losses, including output energy coupling.

In this chapter we present the overall design of the new system and describe in detail all required components. Wherever possible, low power, fibre pigtailed components were chosen in an attempt to progress towards an economic product.

5.1 Overall design

The intensity of the pulse train output of the storage loop is improved by using five metres of erbium-doped fibre amplifier. Introducing gain into the loop is expected to compensate the losses of the rapidly decaying signal level and maintain the reference beam amplitude. As the feedback gain is set slightly below the lasing threshold, the storage loop is not oscillating, and successive reference pulses can be maintained.

The reference beam storage mentioned in chapter 3 is very similar to a fibre ring laser, if an amplifying medium like erbium-doped fibre were included in the cavity. The overall design can be divided into four segments, namely: signal source, source to fibre couplers, storage loop, mixing and detection, as illustrated in Figure 5.1.

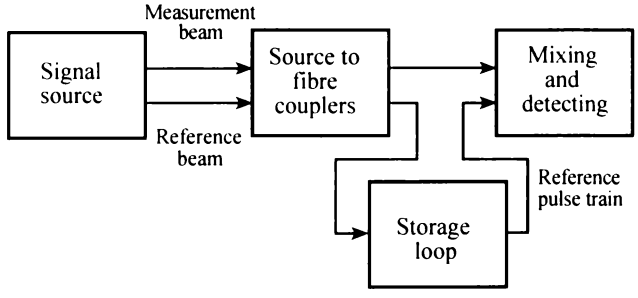

Figure 5. 1 - Block diagram of overall design.

The components that constitute each of these sections and their purpose are now discussed in more detail.

5.2 Signal source

A laser diode was used as the signal source. Its beam was directed through a collimating lens into an acousto-optic modulator, which was modulated by a switched radio frequency signal. The up shifted output beam of the acousto-optic modulator was used as reference beam and the downshifted one as the measurement beam.

5.2.1 1550 nm distributed feedback laser diode

Erbium-doped fibre amplifiers have attracted most attention because they operate near 1550 nm, the wavelength region in which the fibre attenuation is minimum. A multiple quantum well distributed feedback laser diode (ML976H11F, Thorlabs, New Jersey USA) was chosen as the signal source for the new optical system. This laser diode emits a light beam of 1550 nm with a maximum power of 6.0 mW in continuous wave mode. The threshold current is 15 mA and the operating current 35 mA at 5.0 mW.

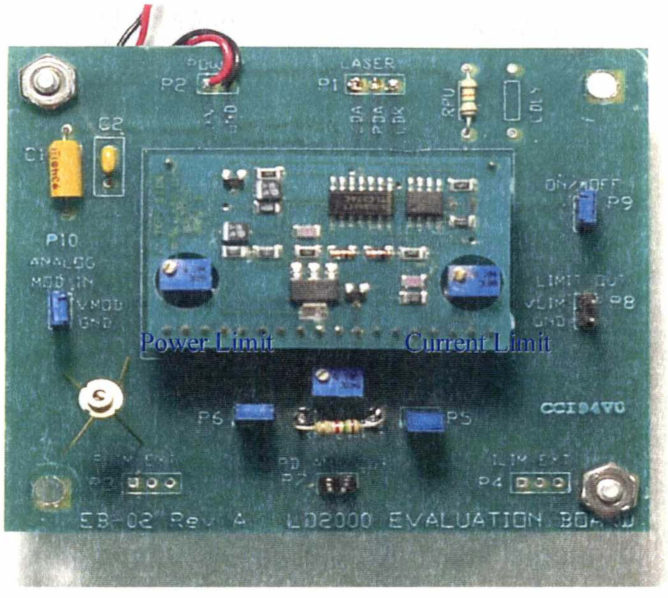

Figure 5. 2 - Photograph of regulated evaluation board (7.5 cm × 9.0 cm) for 1550 nm distributed feedback laser diode.

Figure 5.2 shows a photograph of the evaluation board (LD2000, Thorlabs, New Jersey USA) used as the current source. The LD2000 can be operated with the 1550 nm distributed feedback laser diode, which has a common laser anode and monitor photodiode cathode. Onboard trim potentiometers are provided for controlling the laser power and current limit. Both functions can also be controlled via an external voltage source at a rate of 40 mA/V.

The laser is mounted in a *XY* positioner (SPT1, Thorlabs, New Jersey USA) to ensure proper alignment with the following optical components.

5.2.2 Acousto-optic modulator

The acousto-optic modulator (0103045, Aurora Photonics Inc, California USA) consists of a suitable crystal through which an ultrasonic wave of wavelength λ_s propagates. Because it is a longitudinal or compression wave, it causes the index of refraction of the material to vary sinusoidally with the signal wavelength λ_S.

This variation of refractive index represents a diffraction grating to the incident light. The analysis of the light / acoustic wave interaction is similar to that of Bragg diffraction from crystal planes. The incident light beam strikes the planes at an angle close to normal, and a fraction of the beam is diffracted. For a certain angle θ only, the waves reflected from adjacent planes interfere constructively. Therefore, $sin\theta$ =

$\lambda/2\lambda_s$. For typical ultrasonic frequencies, θ may be a few degrees. Under proper conditions, nearly all of the incident light may be diffracted, or deflected, into angle θ.

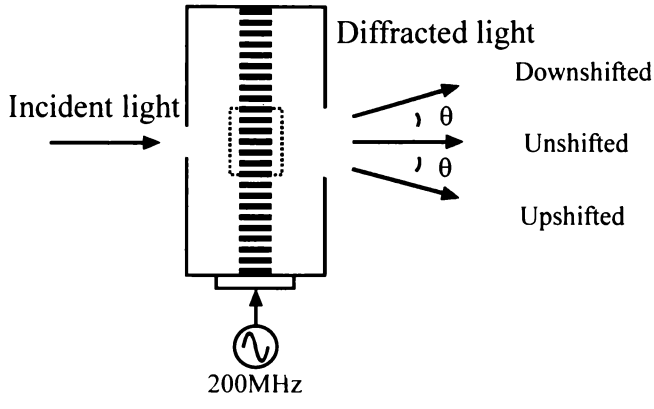

Figure 5. 3 - Diffraction of light by the acoustic wave of an acousto-optic modulator.

Figure 5.3 illustrates that the ultrasonic waves as the solid black lines emanating from the modulator. The intensity of the diffracted light is proportional to the intensity of the ultrasonic wave, which can be controlled by the amplitude of the electronic signal applied to the acoustic transducer (Saleh and Teich, 1991). As the acoustic wave inside the modulator is a travelling wave, the incident light is slightly up-shifted in frequency for the first order diffracted beam and downshifted for the corresponding negative diffraction order.

In the new system, the downshifted beam is used as the measurement beam and the up-shifted one is used as the reference beam, which effectively acts as a local oscillator with a slightly different frequency.

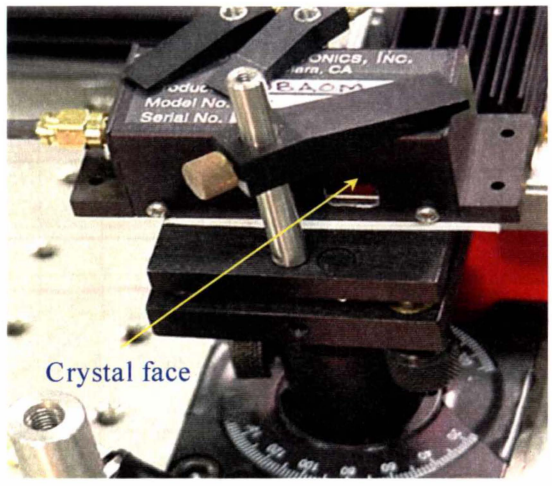

Figure 5. 4 - Photograph of acousto-optic modulator.

The input beam should enter at the geometric centre of the crystal face shown in Figure 5.4. The polarization of the shifted beams is perpendicular to the input beam. The measured angle between un-shifted and shifted output beams is 3.25 °.

Figure 5.5 illustrates the experimental set-up used for the new design. In order to obtain the fastest possible rise time, the laser beam diameter on the acousto-optic modulator was kept as small as possible. The collimating lens (C230TM-C, Thorlabs, New Jersey USA) produced a 0.4 mm ($1/e^2$) beam diameter at the acousto-optic modulator.

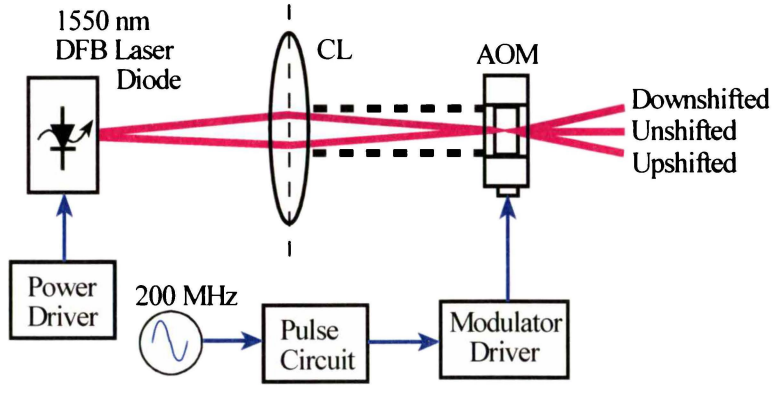

Figure 5. 5 - Experiment set-up for acousto-optic modulator.

At 2.0 W modulation signal the diffracted orders contained 21% of the incident light each. When switching the RF signal on and off the best rise time was measured as 30 ns (10 to 90 % level). An example of a measured output pulse from the acousto-optic modulator is shown in Figure 5.6.

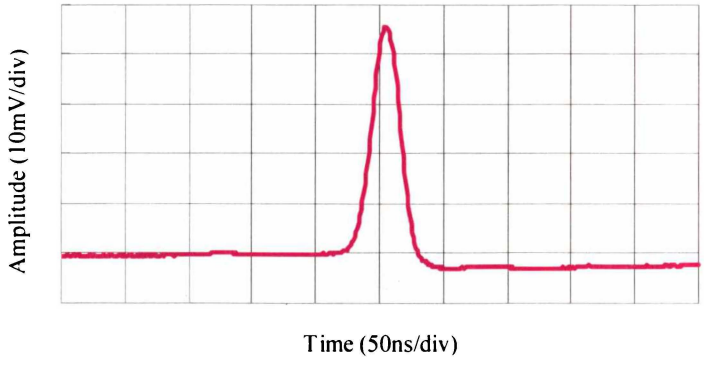

Figure 5. 6 - A typical up-shifted pulse from the acousto-optic modulator.

5.2.3 Modulator driver

The modulator driver (ME-2002, IntraAction Corp., Illinois USA) is a solid-state device that contains a 200 MHz (0.0025% accuracy), radio frequency source and an amplifier. A separate input is available for amplitude modulation of the RF signal. To align and check the laser beams the modulator is operated without external control to deliver a continuous 200 MHz signal to the acousto-optic modulator. In the final set-up a gating circuit is connected to the analogue input to rapidly switch the RF signal on and off and to generate the pulses of up shifted and down shifted radiation.

The block diagram of the circuit is shown in Figure 5.7 (a) and the schematic diagram in Appendix IV. The circuit uses a 74HC132 series of Schmitt trigger high-speed CMOS NAND gates to adjust the duty cycle of the pulse. Figure 5.7 (b) illustrates the measured waveform corresponding to the pulse circuit timing. The circuit has a time constant determined by the product of the resistor R and capacitor C that allows setting the pulse width between 10 ns and 100 ns. The output pulse width shown in Figure 5.7 (b) is 12 ns. Figure 5.8 shows a typical optical pulse from the acousto-optic modulator when the pulse circuit is operated at 500 kHz.

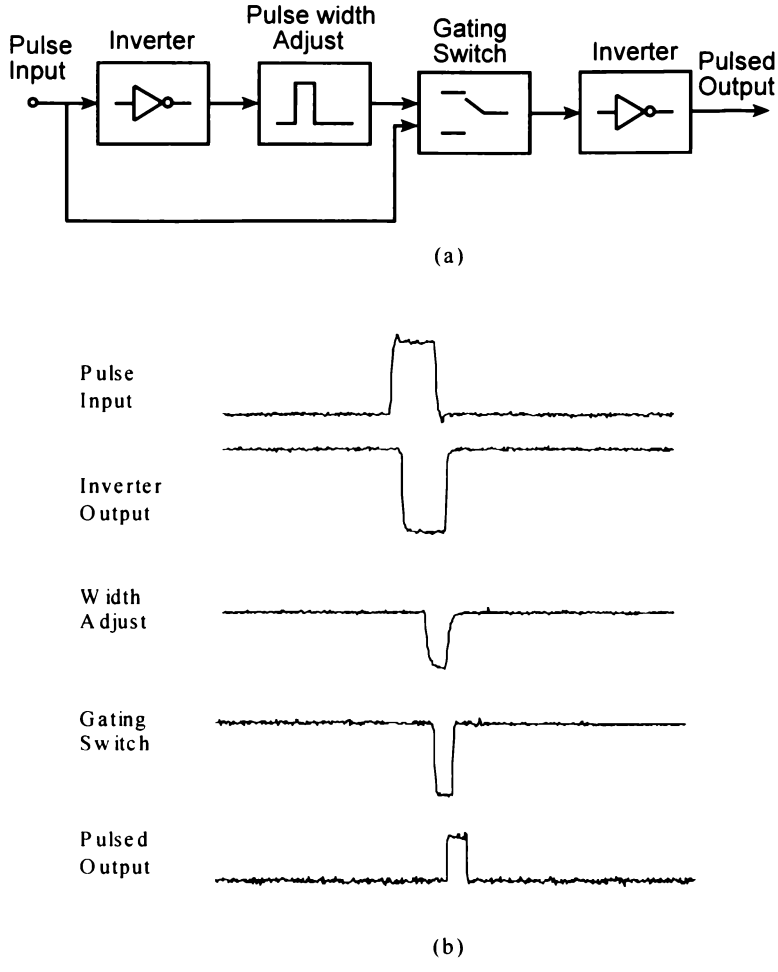

Figure 5. 7 - (a) Block diagram (b) timing for pulse circuit.

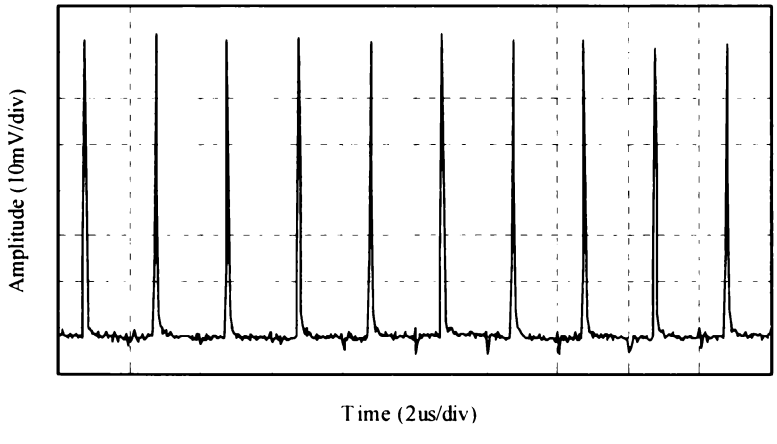

Figure 5. 8 - A typical optical pulse output of the acousto-optic modulator controlled by a pulse circuit at 500 kHz.

5.3 Source to fibre coupling

The up-shifted beam from the acousto-optic modulator is directed onto a rotating mirror (simulating the moving target) and is then focussed by a lens (C220TM-C, Thorlabs, New Jersey USA) via a coupler (KT111, Thorlabs, New Jersey USA) into single mode fibre (Section 5.4.1). The downshifted beam is similarly focussed into another piece of single mode fibre, however a fixed plane mirror is used. Care is taken that the reference and measurement beams have the same path length from the acousto-optic modulator output to the fibre.

The zero order diffraction from the acoustic modulator is blocked by a beam stop.

5.4 Storage loop

The new fibre storage loop consists of a significantly larger number of components than in the previous designs referred to Dorrington. Most of these components are required to improve noise and stability of the amplification process. A schematic diagram of our experimental set-up is shown in Figure 5.9. An erbium-doped fibre amplifier provided the gain of the storage loop which was composed of a length of beam delay fibre, two polarisation controllers, four polarisation independent isolators, a wavelength division multiplexer, 5 m of erbium doped fibre, a tuneable filter, and a 980 nm pump laser diode module.

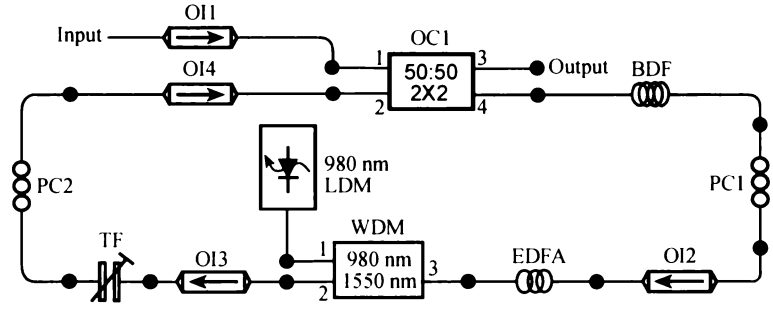

Figure 5. 9 - The experimental configuration of amplified reference beam storage loop. OI1,OI2,OI3,OI4: optical isolators; BDF: beam delay fibre; C1, PC2: polarisation controllers; OC1: optical coupler; LDM: pump laser module; WDM: wavelength division multiplexer; EDFA: erbium-doped fibre amplifier; TF: tuneable filter.

The signal that is focussed into the storage loop by the source to fibre coupler first passes through an optical isolator OI1. Optical isolators only allow light to pass in

the direction indicated by the arrow. OI1 was used to block any reflections from the output ports of the optical coupler OC1. In the amplified reference beam storage loop three optical isolators, OI2, OI3 and OI4, were used to eliminate backward amplified spontaneous emission emitted by the erbium-doped fibre and any reflections from the connectors in the storage loop.

When the pulsed laser signal passes through port 1 of OC1, half is divided off and becomes the stored reference beam, while the other half becomes the first pulse at the output, port 3 of OC1. The stored reference beam passes from port 4 of OC1 through the BDF, PC1, and OI2 into the EDFA. The reference beam is then combined with the pump laser diode radiation by the WDM. The amplified signal propagates through OI3, TF, PC2 and OI4 to the second input port of the optical coupler, OC1. Half of it becomes the second output pulse at port 3 of OC1 and the other half the next pulse in the storage loop. This way successive reference beam pulses are produced.

The components of the storage loop will now be discussed in detail.

5.4.1 Single mode optical fibre

The single mode optical fibre (SMF-28-100, Corning, New Jersey USA) used in our set-up has a 900 μm jacket, 125 μm cladding, and 8.3 μm core diameter. The numerical aperture is 0.13. This small value in conjunction with the small core diameter make is very difficult to efficiently couple light into the fibres. About 20% of each shifted AOM output could be coupled into the fibre. To minimise coupling losses within the storage loop pigtailed components were used whenever possible.

5.4.2 FC/PC connectors

Major causes for additional losses were the insertion losses of the connectors. Each component was terminated with a FC/PC connector (30126D1, Thorlabs, New Jersey USA). The working faces of optical connectors are highly polished and designed for precision alignment. Placing the connector in a metallic housing (polishing disk) and polishing the front face on film in a figure eight arrangement for some time will leave the surface well polished. Signal quality will be seriously compromised if

optical connector faces or the mating sleeve into which they are inserted are mishandled or become dirty. All connector faces were regularly checked with a fibre inspection microscope.

Optical connectors that are used in the system must be of the same type. Use of other types of connectors will result in poor performance, and excessive back reflection could cause damage to the high power pump laser. Optical mating sleeves are used to ensure the precision alignment of connectors.

5.4.3 Optical fiber couplers

Two types of fibre couplers are used within the storage loop. The first one is a 3dB coupler (10202A-50-FC, Thorlabs, New Jersey USA), which has a measured split ratio of 50:50. The second one is a 90:10 coupler (C-NS-AL-10-H-1210-15-FC, Communication Accessories Ltd., Auckland, New Zealand), which can be inserted at any location to monitor the behaviour of the system with low insertion loss.

5.4.4 Erbium-doped fibre

The optical amplifier of the storage loop consists of erbium-doped fibre (FS-ER-7A28, Thorlabs, New Jersey USA), which is pumped via the wavelength division multiplexer by a 980 nm laser. 980 nm were chosen because this is the most efficient pump wavelength for amplifying a 1550 nm signal (Sola *et al.*, 2002). Various lengths of erbium-doped fiber from 1-12 m were used to characterize the performance of the system. For the final set-up a length of 5 m was chosen.

5.4.5 980 nm laser module

The pump laser system (Figure 5.10) consists of a laser diode module (00651, ADC Telecommunications Inc., USA), which has modulation input, a photodiode to sample and monitor output, temperature sensor, and thermo-electric cooler. The module can deliver up to 100 mW at 980 nm from the pigtailed fibre optic cable. Its output is very temperature sensitive, so that the temperature must be carefully controlled. The module has an imbedded thermistor and thermo-electric cooler, which were connected to a controller circuit (DN1220, Thermoptics Inc., USA). An

aluminum heat sink is used to dissipate the excess heat from the pump laser diode. The controller circuit was set at a fixed temperature of 24 °C.

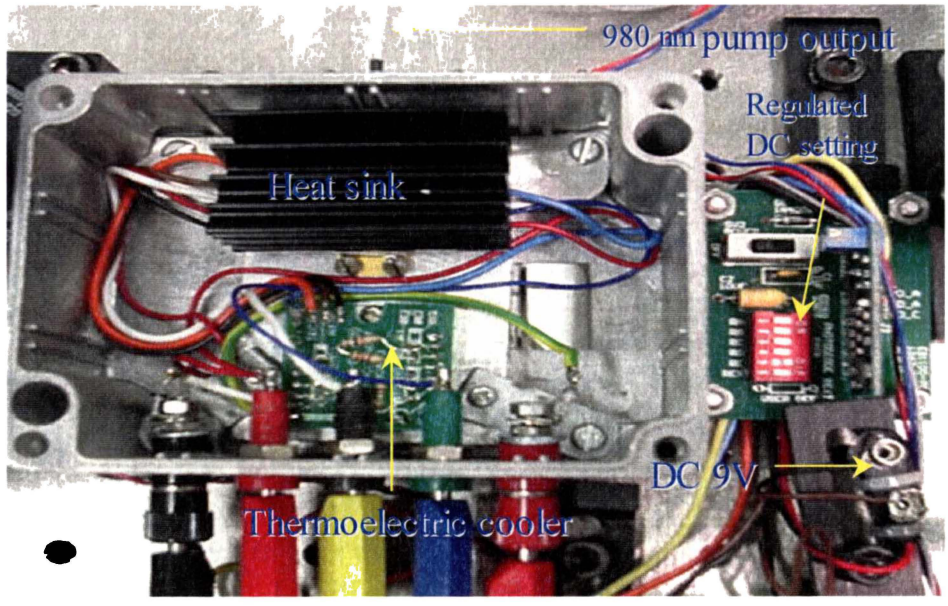

Figure 5. 10 - Photograph of 980 nm laser diode module with a subminiature thermoelectric cooler controller.

Proportional gain and integrator time constant are set independently with resistors, and are optimised to minimize temperature overshoot and stability. In addition, the maximum cooling and heating current supplied to the thermo-electric cooler can be adjusted from 0.0 to 2.0 A with two resistors.

5.4.6 Wavelength division multiplexer

A wavelength division multiplexer allows the combination or separation of optical signals at different wavelengths. In our system, the pump laser and the incoming signal are combined into the erbium-doped fibre amplifier for signal amplification. Our WDM (FWDMC012111414, E-TEK, California USA) uses interference filter technology to separate or combine the light. Its wide operating wavelength range makes it ideal for 980 nm pumped optical fibre amplifiers. It has a low insertion loss of 0.6 dB and low polarisation dependent loss of 0.05 dB.

5.4.7 Optical isolators

The optical isolator (4015SAFC, Thorlabs, New Jersey USA), which provides more than 40 dB optical isolation, was used to block signals that propagate in reverse

direction. For instance, the input optical isolator allows the input signal through and eliminates backward propagation of amplified spontaneous emission (Figure 5.11). The output optical isolator is used to eliminate reflections from devices like connectors that might disturb the fibre amplifier.

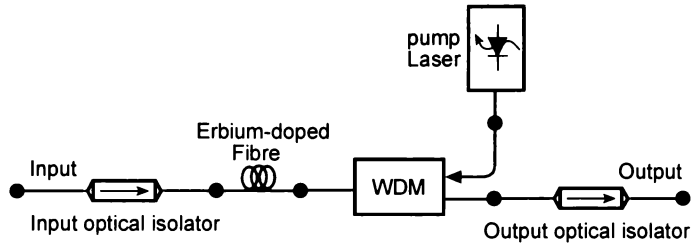

Figure 5. 11 - Optical isolators used in a backward pumping system.

5.4.8 Tunable filter

The filter (TF-11-11-1520/1570-9/125-S-40-3S3S-1-1, OZ Optics ltd., Ontario Canada) is tuned to the wavelength of the signal at 1550 nm, to block unwanted wavelengths in the gain profile of the EDFA. It has a pass band of 50 nm with a loss of 60%, but reduces the amplified spontaneous emission propagating through the loop to that at the signal wavelength only. It was found to be effective in improving the signal to noise ratio (Yokota *et al.*, 2002).

5.4.9 Polarisation controllers

The amplitude of the reference pulse train exiting the storage loop is uneven and has a periodic envelope. Ahmed and Onodera (1996) have given a simple explanation of this phenomenon and attribute it to the mismatch between the radio frequency from the modulator driver and the resonance of the amplifier itself.

We have used a similar approach to that of Li *et al.* (2001), which has been reviewed in section 3.3.1. We have included two polarization controllers (FPC560, Thorlabs, New Jersey USA) in the storage loop to improve the uneven amplitude of the reference beam pulses and increase the signal to noise ratio.

Figure 5.12 illustrates the working principle of the polarisation controller. We assume that the electric field vector of the input signal is linearly polarised in the x- direction

when entering the PC. After the polarisation controller, the field vector is rotated with respect to the *x*-axis.

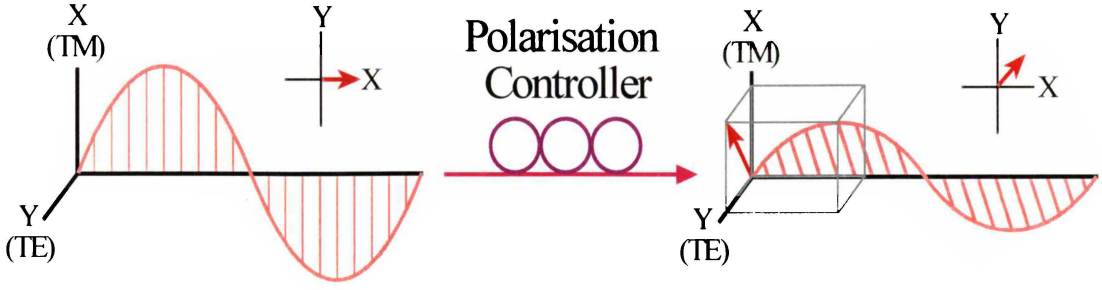

Figure 5. 12 - The working principle of the polarisation controller.

In the polarisation controller a number of coils of optical fibre is wound onto each of the three paddles. It utilizes stress-induced birefringence to create three independent fractional "wave plates" to alter the polarisation of the transmitted light on a single fibre. The fibre is looped into three independent spools, creating three independent fractional fibre retarders. The amount of birefringence induced in the fibre is a function of the fibre cladding diameter, the spool diameter (fixed), the number of fibre loops per spool, and the wavelength of the light. The desired birefringence is induced by the loop in the fibre, not by twisting of the fibre paddles. The fast axis of the fibre, which is in the plane of the spool, is adjusted with respect to the transmitted polarisation vector by manually rotating the paddles.

Generally, the polarisation controller converts one state of polarisation into another one by loading the three paddles with a prescribed number of fibre loops to represent a nominal "quarter wave retarder", a "half wave retarder" and a "quarter wave retarder". The first "quarter wave retarder" transforms the input polarisation state into a linear polarisation state. The "half wave retarder" rotates the linear polarisation state. The last "quarter wave retarder" transforms the linear state into an arbitrary polarisation state. Twisting the paddles with respect to each other rotates the effective plane of polarization. Therefore, adjusting each of the three paddles (fibre retarders) allows complete control of the output polarisation state.

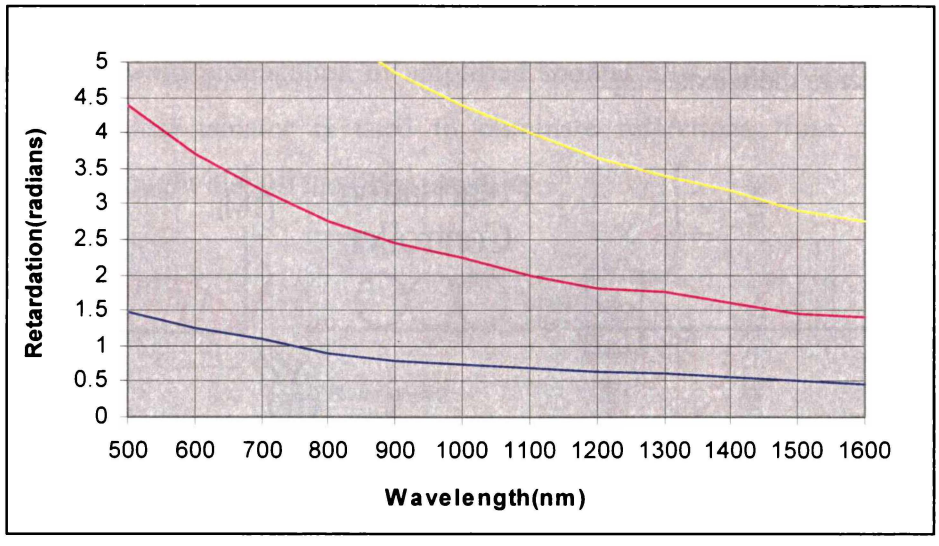

Figure 5. 13 - Plot of retardation per paddle versus wavelength. At 1550 nm for the paddle of "quarter wave retarder" in blue the retardation is 0.5 radians, 1.4 radians for the paddle of "half wave retarder" in purple and 2.7 radians for the paddle of "quarter wave retarder" in yellow. (Doc. # 1167-D01, Thorlabs, New Jersey USA, 1998)

Figure 5.13 shows the plot of retardation per paddle versus wavelength for our PC. At 1550 nm for the paddle of "quarter wave retarder" in blue the retardation is 0.5 radians, 1.4 radians for the paddle of "half wave retarder" in purple and 2.7 radians for the paddle of "quarter wave retarder" in yellow.

5.5 Optical mixing and detection

In section 5.2.2, we discussed that 1550 nm laser light with the frequency f_0 was incident through an acousto-optic modulator driven by a frequency f_m. This generates two beams: the up-shifted beam is used as a reference, E_r, and the downshifted as a measurement beam, E_m. The two beams are given as,

$$E_r = A_r \cos\left[2\pi(f_0 + f_m)t\right] \qquad 5\text{-}1$$

$$E_m = A_m \cos\left[2\pi(f_0 - f_m)t + 2\pi\int f_d dt\right] \qquad 5\text{-}2$$

where A_r is the amplitude of reference beam, A_m the amplitude of measurement beam f_m the modulation frequency, and f_d the Doppler-shifted frequency. After the storage loop, the reference beam is combined with the measurement signal by a 2x2, 3 dB

fibre coupler (10202A-50-FC, Thorlabs, New Jersey USA). Each reference pulse has travelled a distance equal to that of the measurement beam.

The mixing on the detector produces a burst signal. The intensity on the photodetector is given as,

$$I = \varepsilon_0 c[A_r^2 + A_m^2 + 2A_r A_m cos(4\pi f_m t + 2\pi \int f_d dt)] \quad 5\text{-}3$$

5.5.1 Photodetectors

The high-speed and high responsivity InGaAs photodetector (C30617BFC, Warsash Scientific, Australia) is of a mesa-type diode structure. This photodetector is designed for use in 1550 nm single mode fibre-optic communications systems. Two photodetectors are used in a differencing configuration, one on each output port of the mixer.

5.5.2 Radio frequency amplifier

Figure 5.14 illustrates the four stages of the radio frequency amplifier circuit; the full circuit diagram, a more detailed description of the circuit as well as the printed circuit board layout is included in Appendix V: The first stage is a transimpedance amplifier, *OP AMP1 or OP AMP2,* which is used to convert the photocurrent, I_{sc}, into a voltage signal.

The second stage functions as a signal amplifier. The amplified signal then passes into a differencing amplifier (AD8001, Analog Devices) to reduce the noise. In this configuration signals that are in phase at both detectors will be cancelled due to the differencing configuration. However, when the amplified reference pulse train is optically mixed with the Doppler shifted measurement beam at the optical coupler a Doppler burst is produced that is out of phase by π radians at the two output ports of the coupler. Due to this π phase difference, the amplifiers double the Doppler burst amplitude while the in-phase noise is reduced.

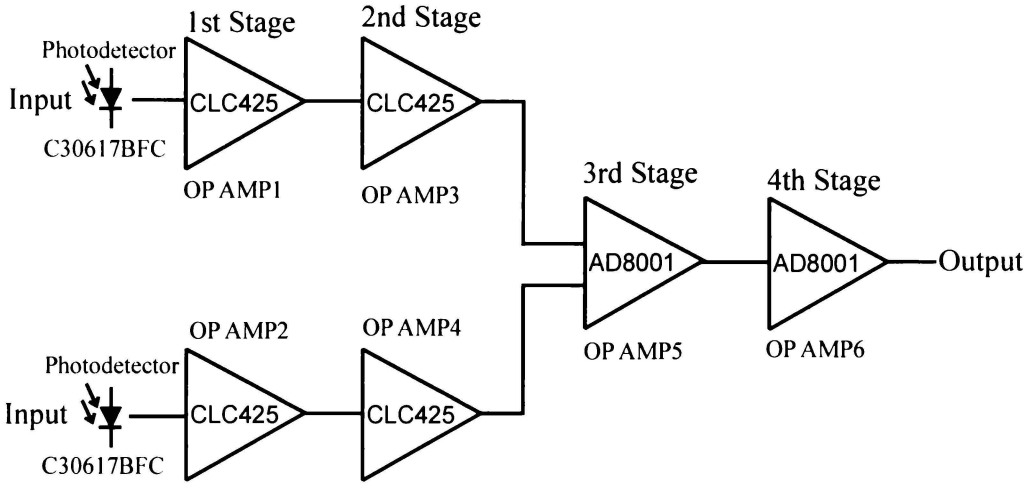

Figure 5. 14 - Block diagram of radio frequency amplifier.

Finally, the voltage follower is designed to match the impedance of the next stage, the input of the oscilloscope, the spectrum analyzer, or the phase lock loop. Figure 5.15 illustrates the photograph of the radio frequency amplifier.

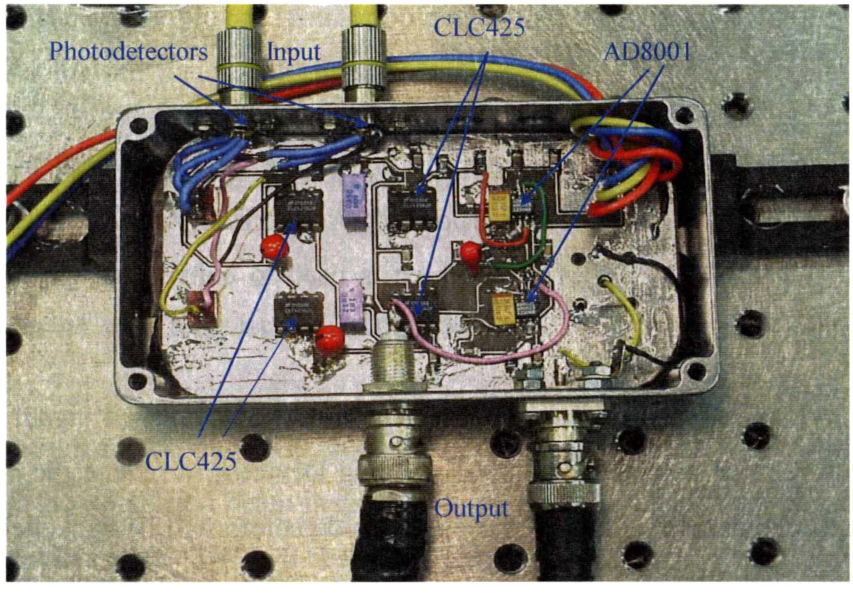

Figure 5. 15 - Photograph of radio frequency amplifier.

5.5.3 Phase-locked loop demodulator

If the optical path of the laser beam is very long random noise might introduce a frequency shift, degrading the accuracy of the Doppler velocimetry. Mixing the signal with the highly stable and accurate frequency provided by a crystal oscillator

can improve the signal to noise ratio. The output signal can be further stabilised by the inclusion of a phase-locked loop that locks the output to the crystal reference.

Figure 5.16 shows the block diagram of the phase-locked loop used for noise reduction in this thesis, which follows the general principle discussed in section 4.1.4.

Input signal 1 is the main carrier frequency of 400 MHz plus a Doppler shifted frequency of typically 30 kHz. The second input signal at input signal 2 is 200 MHz directly from the modulation driver. This is passed through a frequency doubler to become 400 MHz. The crystal oscillator frequency is 10.752 MHz.

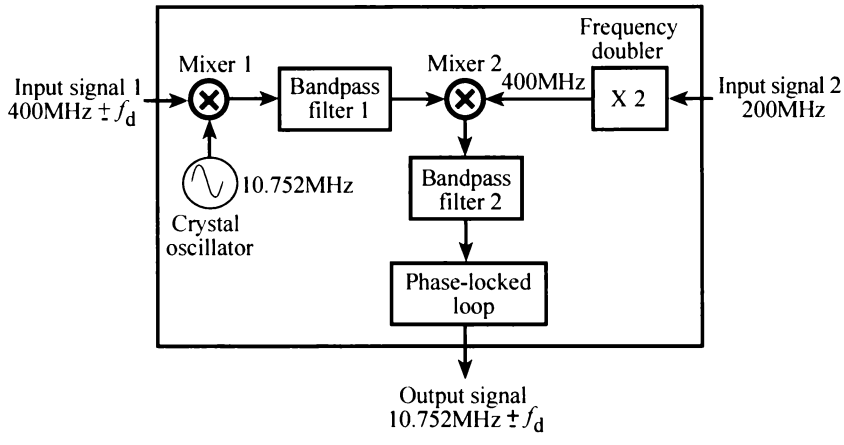

Figure 5. 16 - Block diagram of phase-locked loop for the experimental set-up.

The signal from the radio frequency amplifier is mixed with the local oscillator, the 10.752 MHz crystal oscillator, producing a combined signal as previously mentioned in Chapter 4.1.4. The full circuit diagram of the demodulator is presented in Appendix VI and the printed circuit board layout is shown in Figure 5.17.

As the very weak signal is only present during very short Doppler bursts, sensitive signal processing methods are still needed to determine the Doppler signal.

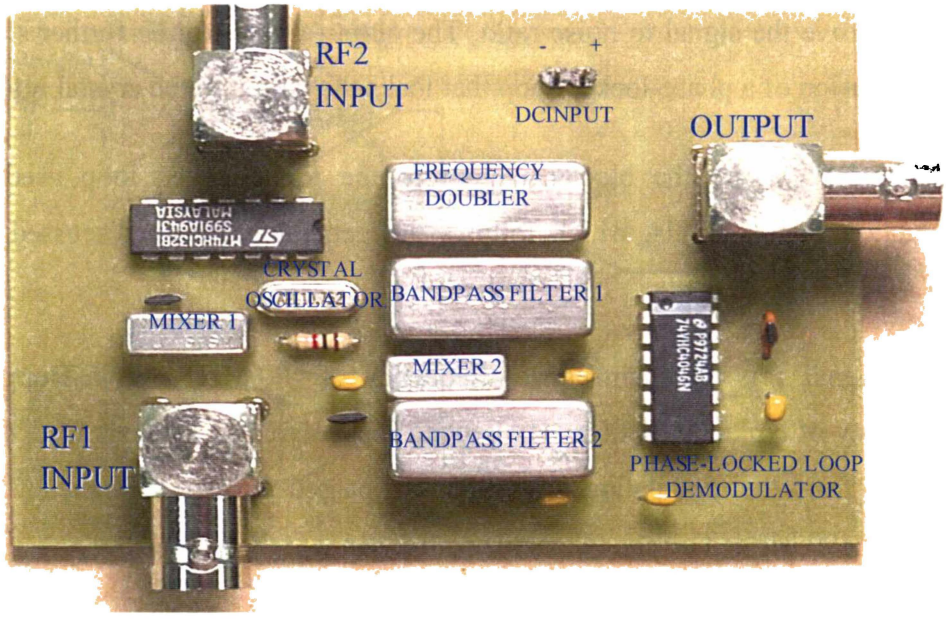

Figure 5. 17 - Photograph of phase-locked loop demodulator for the experimental set-up.

5.5.4 Spectrum analyser and other apparatus

The output spectrum is measured with a spectrum analyser (R3131, Advantest, USA), which has a bandwidth from 9 kHz to 3 GHz. Time series are measured by a fast photo detector and a digital real-time oscilloscope with a sampling rate of 5.0 Giga samples per second at 1.0 GHz bandwidth. All the electronic equipment is shown in Figure 5.18.

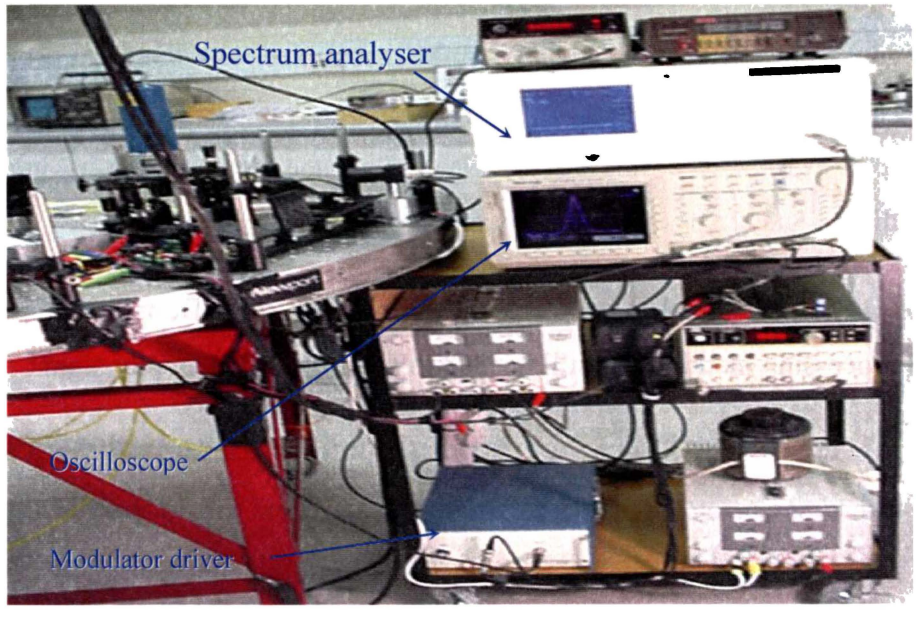

Figure 5. 18 - Photograph of apparatus.

Chapter 6

Results and discussion

In the previous section the main components of the amplified reference beam storage loop have been presented. The various stages of the system need to be characterized, and the performance of the arrangement needs to be evaluated. For this purpose several experiments and analyses have been carried out. The results of this evaluation will be presented in the following sections.

Section 6.1 and 6.2 cover measurements of amplifier gain and noise, respectively. Section 6.3 gives the calculation of gain and loss within the storage loop. A simple optical set-up that generates a simulated Doppler signal, which is mixed with stored reference beam pulses, is discussed in 6.4. Section 6.5 of this chapter presents an optical arrangement for velocity measurements through a tachometer arrangement. An alternative method used to de-noise for signal processing is discussed in 6.6. Signal processing software developed to improve the signal to noise ratio will be presented in 6.7. Finally, at the end of this section the overall performance of the new method of the amplified reference beam storage will be discussed.

6.1 EDFA gain measurements

The erbium-doped fibre amplifier (EDFA) gain measurements were obtained by comparing the input and output of the optical amplifier. Figure 6.1 (a) shows the experimental set-up to obtain the reference power, P_{ref}, of the system without the amplifier. TpA was connected to a photo detector followed by a 50 Ω termination. The reference power level was recorded on a spectrum analyser. The optical amplifier module including a pump laser, wavelength division multiplexer, and 5 m of erbium-doped fibre was then inserted between TpA and TpB, and the amplified output signal level (P_{meas}) was measured (Figure 6.1 (b)). The output power of the

signal laser diode was varied from 10 μW to 70 μW at 10 μW intervals by adjusting the resistor attenuator of its regulated DC power driver.

Gain values, in dB, were then calculated as

$$G = 10log\left(\frac{P_{meas}}{P_{ref}}\right) \qquad 6\text{-}1$$

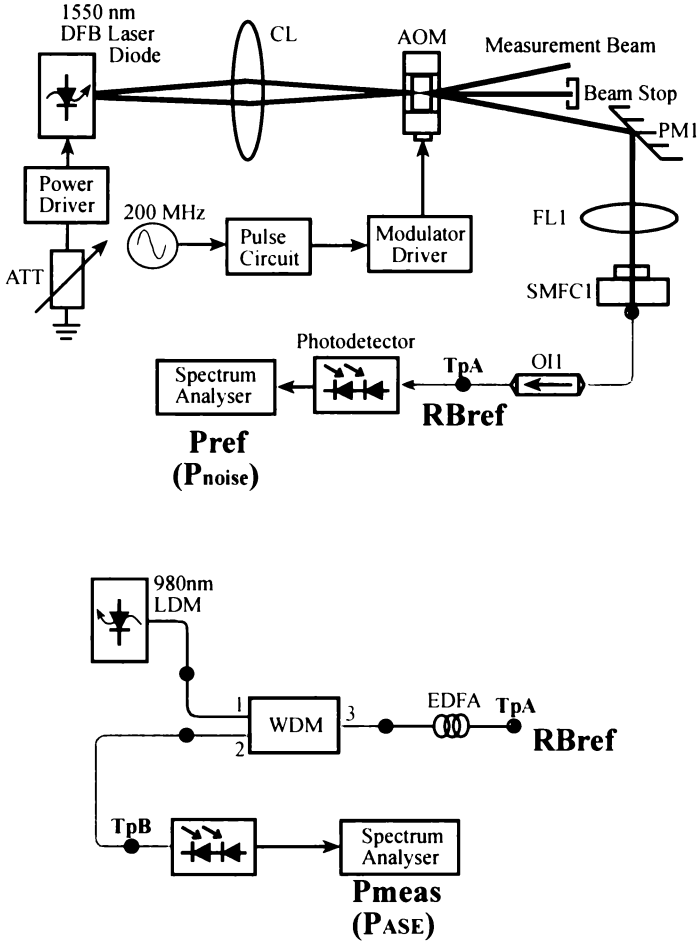

Figure 6. 1 - Experimental set-up (a) the reference power Pref and Pnoise of the laser source; (b) for the output signal power Pmeas and P_{ASE} for EDFA gain and ASE noise measurements.

Figure 6.2 (a) shows the output versus input pulse intensity of the erbium-doped fibre amplifier as a function of pump power and 6.2 (b) the gain vs. pump power as a function input pulse intensity. The pump power ranges from 5 mW to 50 mW and the photodiode voltage at the peak of the input pulse from 10 μW to 70 μW.

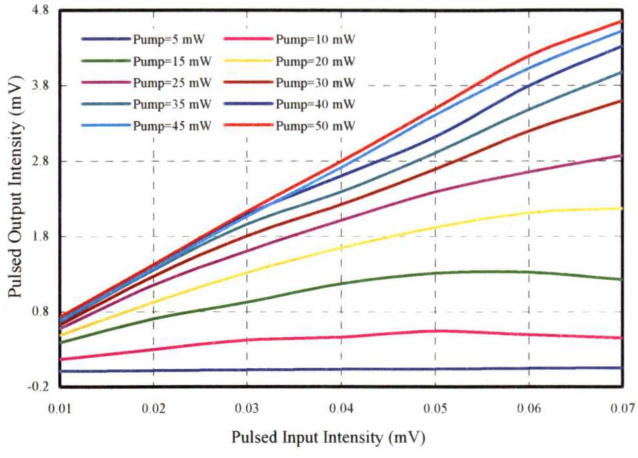

(a)

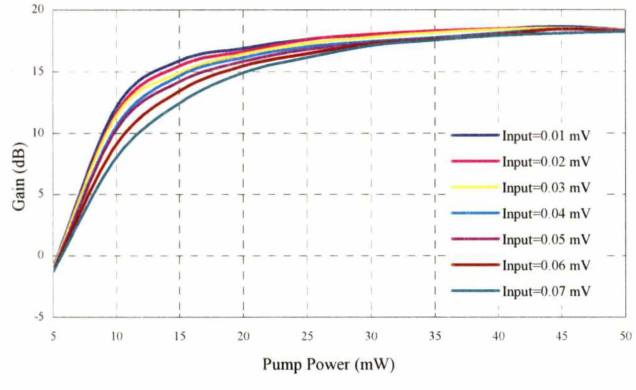

(b)

Figure 6. 2 - (a) The output vs. input pulse intensity; (b) Gain vs pump power.

Figure 6.3 (a) shows the signal to noise and amplified spontaneous emission noise versus pump power. Figure 6.3 (b) shows that at 20 mW pump power, the gain is 15 dB and then saturates at 18 dB as the pump power increases to 80 mW. When gain is equal to amplified spontaneous emission noise, the signal to noise is equal to the signal intensity within the erbium-doped fibre amplifier. The signal-to-noise is saturated at 25 mW within the 5.0 m length of the erbium-doped fibre amplifier, hence as pumping power is increased the amplified spontaneous emission noise also increases and as a result signal-to-noise decreases. This figure was used to determine the optimum pumping power for the erbium-doped fibre amplifier. A pump power of 20 mW was chosen to avoid lasing oscillations, and the signal-to-noise was near maximum.

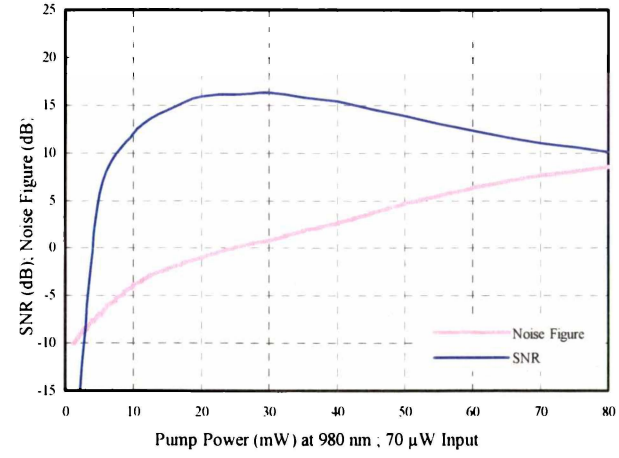

(a)

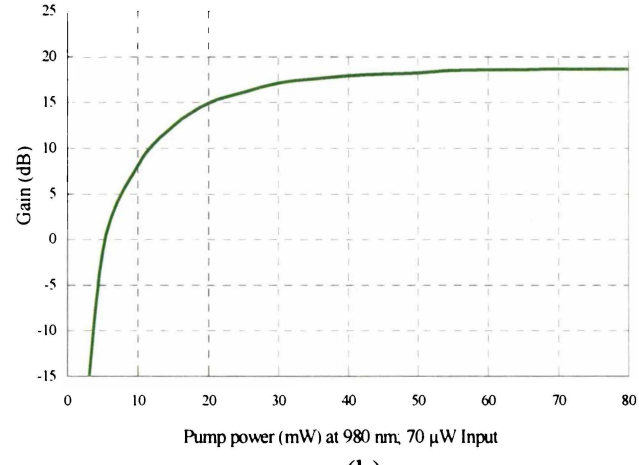

(b)

Figure 6. 3 - (a) SNR and Noise Figure vs. pump power; (b) gain vs pump power.

6.2 Noise sources

Inserting the erbium-doped fibre amplifier into the amplified reference beam storage loop will introduce noise because of the generated amplified spontaneous emission. Besides this there is additional noise introduced: Beating between signal and amplified spontaneous emission causes signal-spontaneous beat noise, and beating between amplified spontaneous emission spectral components causes spontaneous-spontaneous beat noise (Kringlebotn *et al.*, 1995).

The laser source fluctuates in its intensity, phase, and frequency even when the laser is biased at a constant current with negligible current fluctuations. Since such fluctuations can affect the performance of the amplified reference beam storage system, it is important to consider the fundamental noise sources. The incoherent

beating between the various frequency components of the output source causes the intensity noise. The phase noise is caused by slight variations in path lengths through the system, in particular the erbium-doped fibre amplifier, because of vibrations, temperature effects, or the like.

In addition to the optically induced noise there is electrically induced noise such as 1/f and amplifier noise. Precise noise measurements must be performed before constructing the amplified reference beam storage system to limit the interference with the output signal. Experimental results for measurements of amplified spontaneous emission, phase noise, laser intensity noise and electrically induced noise is discussed in the following sections.

6.2.1 EDFA amplified spontaneous emission noise

Noise figure measurements require accurate determination of the level of the amplified spontaneous emission generated by the erbium-doped fibre amplifier itself. However, the true amplified spontaneous emission is masked by the amplified optical signal, making direct measurements difficult. There are a number of possible methods for measuring amplified spontaneous emission levels; the one used for the measurements on this erbium-doped fibre amplifier makes use of level fitting. The level fitting method interpolates the amplified spontaneous emission level occurring at the optical signal from the amplified spontaneous emission level near the signal. This measurement method is relatively simple and when the amplified spontaneous emission around the measurement point is flat, the measurement precision is high.

The experimental set-up for amplified spontaneous emission noise measurements is the same as that presented in Figure 6.1 (a). The laser source spectrum, P_{noise}, was first directly measured with the spectrum analyser and kept in memory for reference. Figure 6.1 (b) shows that the erbium-doped fibre amplifier was then inserted between points *TpA* and *TpB*. The spectrum analyser records the amplified spontaneous emission level.

In addition to the amplified spontaneous emission, the erbium-doped fibre amplifier output also contains amplified optical signal noise and electronic noise from the radio-frequency amplifier and photodetector. The following correction will give a more accurate determination of the amplified spontaneous emission power level,

$$P_{ASE} = P'_{ASE} - G \times P_{noise} \qquad 6\text{-}2$$

where P'_{ASE} is the measured amplified spontaneous emission level, G is the erbium-doped fibre amplifier gain, and P_{noise} is the input noise level.

6.2.2 Intensity noise of the signal laser

The amplitude noise of the heterodyne beat signal arises from laser intensity, photodetector, and electronic amplifier noise. The experimental set-up is similar to that shown in Figure 6.1 (a). Measurements were recorded without pulsing the signal. A 1mW continuous wave signal was available for measurement and reference beam, respectively. Various lengths of beam delay fibre delay the measurement beam. Reference and measurement beam are then optically mixed in a 2 x 2 fibre coupler inserted at *TpA* in Figure 6.1(a). Each output of the fibre coupler is connected to one photodiode of the differencing photo detector, and the beat signal is detected.

The frequency was measured relative to 400 MHz, which is the difference of the up-shifted and downshifted signals. Figure 6.4 (a) and (b) indicate the delayed self-heterodyne spectra at different fibre delay lengths. The shot noise floor for all the spectra in Figure 6.3 lies at 37 dBμV and the electronic noise is measured as -4.08 dBμV/√Hz for all beam delay fibre lengths. The height of the central spike relative to the 'skirt' in Figure 6.4 (b) is related to the effective fringe visibility of the interference. Best visibility is apparent for the pink trace representing a 0.34 m delay fibre.

When the length of beam delay fibre was extended, the excess noise (seen as the skirt on the side of the peaks) rises dramatically, degrading the signal to noise ratio. The visibility decreases as the beam delay fibre length increases. At a length of 450 m, much longer than the measured coherence length of the laser of 0.29 mm (*Appendix VII)*, the interference fringes and the spike of the beat signal disappear from the spectrum. The excess noise is inversely proportional to the laser coherence length and increases proportional to the square of the fibre length, which is described by Harris *et al.* (1998).

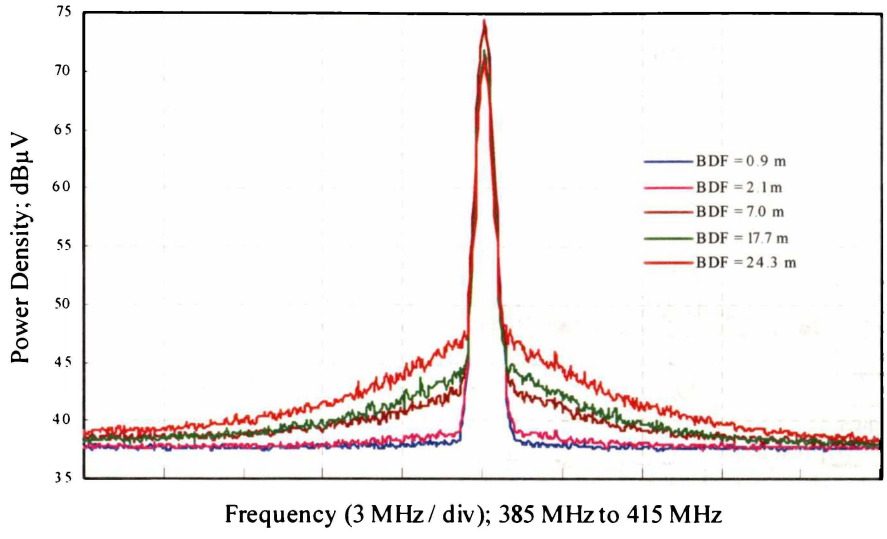

(a)

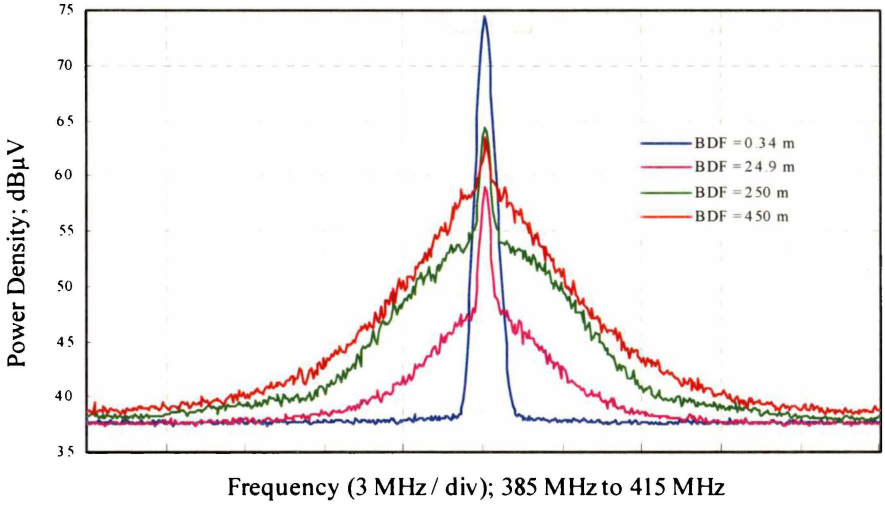

(b)

Figure 6. 4 - Self-heterodyne spectra at different fibre delay. (a) Short delay fibre (BDF); (b) longer range.

6.2.3 Phase noise caused by erbium-doped fibre amplifier

The set up to measure phase noise is almost identical to that used for the intensity noise measurement. However, the erbium-doped fibre amplifier is inserted in the reference beam path before the coupler at *TpA*, and pulse mode is used (Figure 6.5). The travelling path of both the amplified reference and measurement beams is designed to be equivalent in length. The difference between them is within the

coherence length, which allows a number of reference pulses to optically mix with the measurement beam.

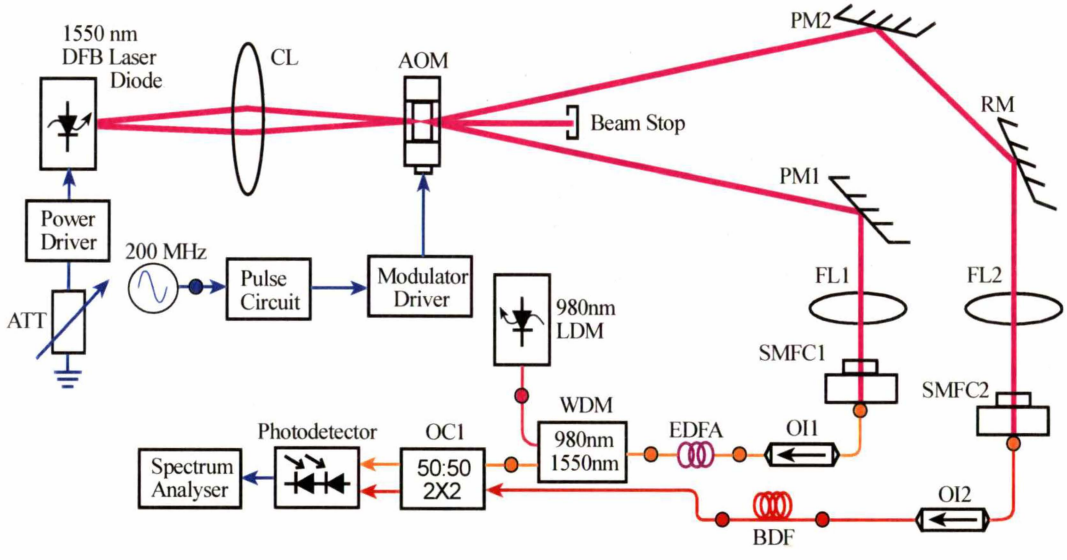

Figure 6. 5 - Optical arrangement for phase noise measurement.

Figure 6.6 illustrates the resulting spectrum. Optically mixing the up-shifted beam with the downshifted beam leads to signal fluctuations owing to phase noise. The pink spike shows the effective beat intensity when using the 5.0 m-long erbium-doped fibre amplifier without any delay fibre. The frequency was measured relative to the 400 MHz beat signal. The height of the beat signal degrades as the delay length increases. When the delay length is greater than 450 m, the spike of the beat signal is completely absent from the spectrum thus leaving only the parabola of the very wide skirt. This is similar to the intensity noise measurement, but the skirt of noise spectrum is broader.

Figure 6.6 also illustrates that the reference level varies between 37.5 dBμV and 60 dBμV; 35 dBμV is the reference level without the EDFA included in the loop. As the delay length increases the noise also increases and hence further degrades the signal to noise ratio. The noise level is very unstable and sensitive to connector properties; that is: interference occurs between the reference beam and the reflection (about 1%) from within the coupler and from the fibre connectors. As the result, the

different travelling path lengths of the interfering beams cause the delayed self-heterodyne signal.

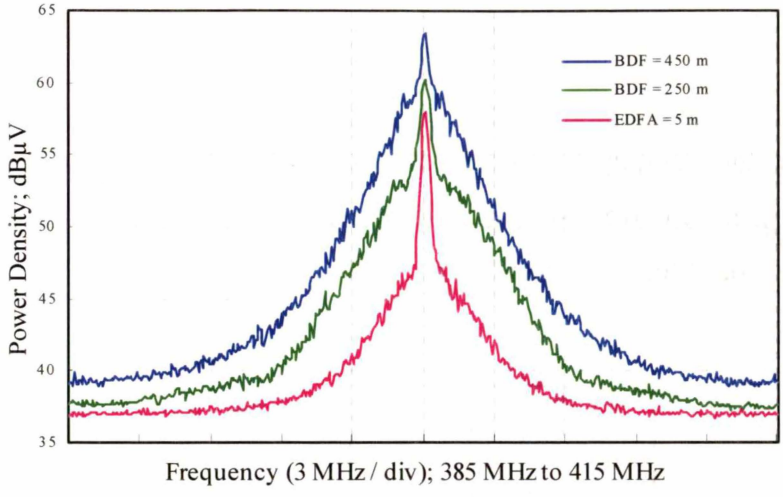

Figure 6. 6 - Self-heterodyne spectra using EDFA of 5.0 m length only and with BDF of 250 m and 450 m length.

6.2.4 Electrically induced noise

Electronic noise mainly consists of noise from the photodetector and the transimpedance amplifier. The lower limits of light detection for photovoltaic detectors are determined by their noise characteristics (Yariv, 1997). The noise current, i_n, is expressed as the sum of the Johnson noise current, i_j, caused by the internal shunt resistance, R_{sh}, and the shot noise current, i_s, resulting from the dark current:

$$i_n = \sqrt{\left(i_j^2 + i_s^2\right)} \qquad 6\text{-}3$$

Generally because photovoltaic infrared detectors have a large dark current, they are usually used at 0 V bias. In this case, the electronic noise is only determined by Johnson noise:

$$i_n = i_j = \sqrt{\frac{4kTB}{R_{sh}}} \qquad 6\text{-}4$$

where k is Boltzman's constant, T is absolute temperature, and B is the noise bandwidth. In contrast, when used with a bias voltage applied, the shot noise is added, as follows:

$$i_s = \sqrt{2qIB} \qquad 6\text{-}5$$

where I is the combined photocurrent and dark current and q is the elementary charge. The noise current shows flat frequency characteristics and is proportional to the square root of the noise bandwidth.

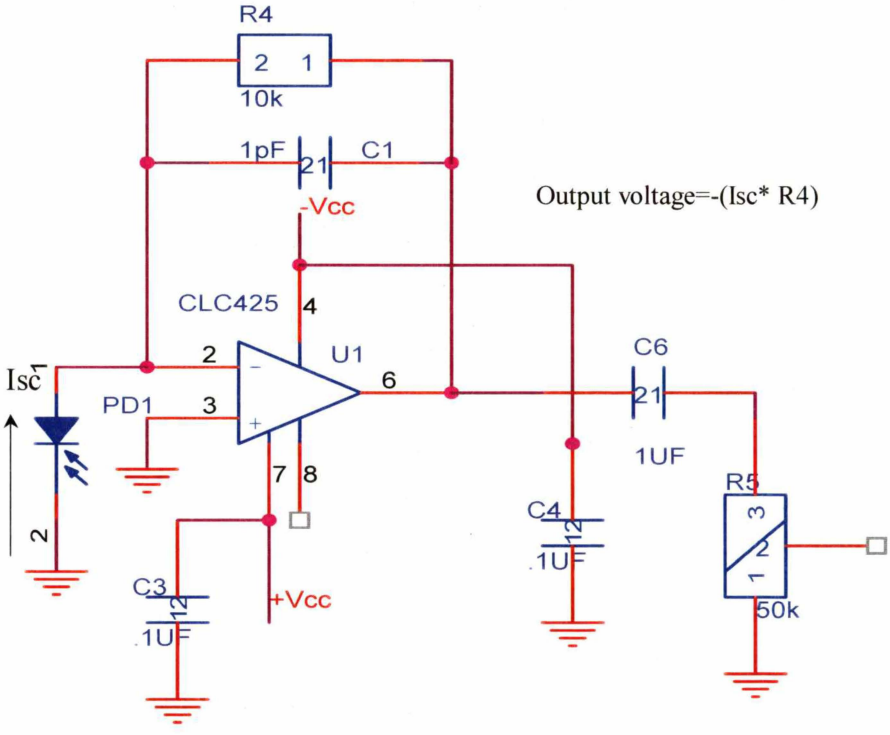

Figure 6. 7 - Basic circuit connection for the front end of radio frequency amplifier.

Figure 6.7 shows the basic circuit connections of such an amplifier as the front end of the radio frequency amplifier shown in *Appendix V*. The output voltage is simply the product of the signal current, I_{sc}, and the feedback resistance, R_4. From the standpoint of noise performance the feedback resistance should be made smaller than the detector's equivalent parallel resistance. The feedback capacitance, C_1, is used mainly to prevent oscillation or ringing and should have a value of several pico farads.

While the circuit of Figure 6.7 makes use of the time constant of C_1 x R_4 to act as a noise filter, it also limits the rise time. The circuit constants should, therefore be

chosen in consideration of the possible application. For applications in which extremely small amounts of infrared energy are to be measured, R_4 can be made larger to increase the output voltage. Care is required however; the operational amplifier noise will increase by a factor of $[1+(R_4/R_{sh})]$.

Figure 6.8 shows the electrical noise at the output of the radio frequency amplifier. The average noise level was measured as1.6 mV and the signal to noise ratio as 30. This radio frequency amplifier has a maximal gain of 121.4 when the input signal is a 0.4 mV, 10 ns long pulse.

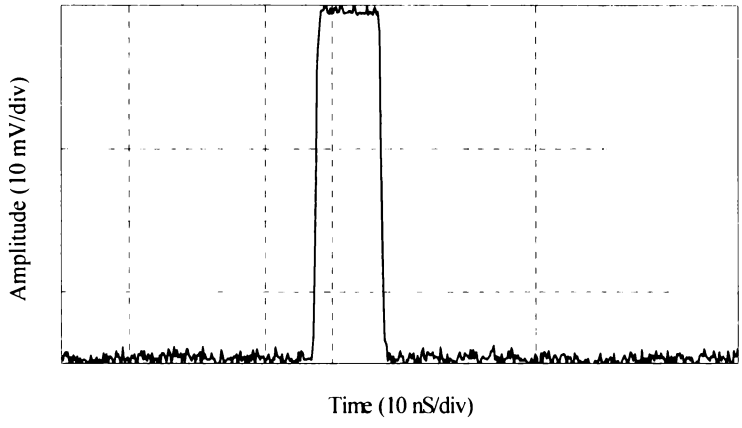

Figure 6. 8 - Electrical noise at the output of the radio frequency amplifier.

6.3 Storage loop measurements

Before the new system can be used to measure the beating between the reference and measurement beams, it is necessary to determine whether the storage loop produces a sufficiently stable pulse train. In section 6.3.1 calculations of the gain and loss in the storage loop are presented that determine if the gain can appropriately compensate the losses incorporated in the storage loop. Using the polarisation controllers and a tuneable filter with other optical components to maintain the pulse train amplitude at a suitable level for mixing with the measurement beam is discussed in 6.3.2.

6.3.1 Calculation of gain and loss

Both gain and noise measurements have been carried out in the previous two sections and in this section we combine these results to calculate the gain and loss in the

storage loop. It is important to know the exact gain and loss of each of the optical components in the loop so that we can determine if the storage loop will go into laser oscillation. This situation is unwanted because it makes the system unstable. Therefore the storage loop is designed so that the total gain is slightly less than unity.

In Figure 6.9, the loss for each optical component and connector (shown as a blue dot) is represented by a negative value. A pulse stored in the storage loop experiences a loss of -15 dB. When the gain of the 5m long erbium-doped fibre amplifier is adjusted to +15 dB this leads to the desired overall gain of 0 dB. An input signal will lose a total of -4.75dB when it reaches the output of the loop.

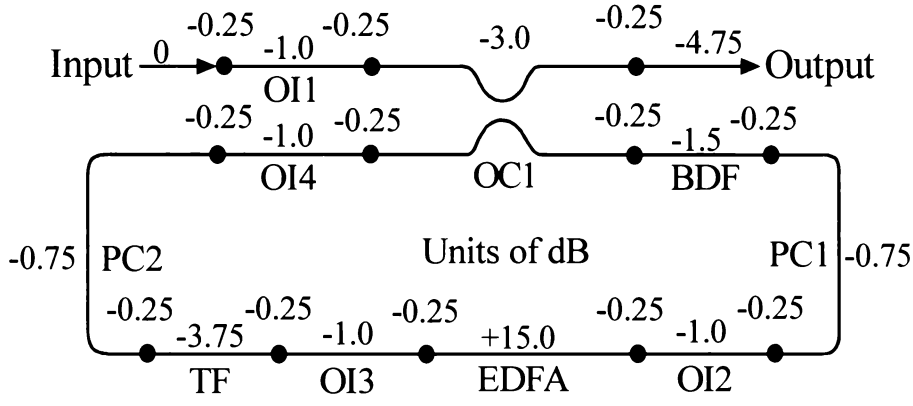

Figure 6. 9 - Calculation of gain and loss in the amplified reference beam storage.

6.3.2 Output pulse train

The pulse output from the storage loop was measured for various configurations. Initially only the basic loop was used without polarisation controllers and tuneable filter.

Without any pump power the gain of the erbium-doped fibre amplifier is negative. No lasing occurs due to the large loss in the storage loop. Then the pump power was adjusted to 5 mW, the amplified spontaneous emission coupled into the loop was so little that the gain of the erbium-doped fibre amplifier was not enough to cause laser oscillation. Changing the pumping power to 20 mW and the input signal to 70 μW, the gain is 14.99 dB as shown in Figure 6.3 (b).

Figure 6.10 shows the resulting pulse waveform from the storage loop. In this case, successive pulses experienced different losses when they propagated through the

storage loop, and their pulse amplitudes become severely uneven. Over a large number of passes through the storage loop the reference pulses still decay.

We found that the amplified reference beam pulses did not remain stable as the pump power was increased to more than 20 mW.

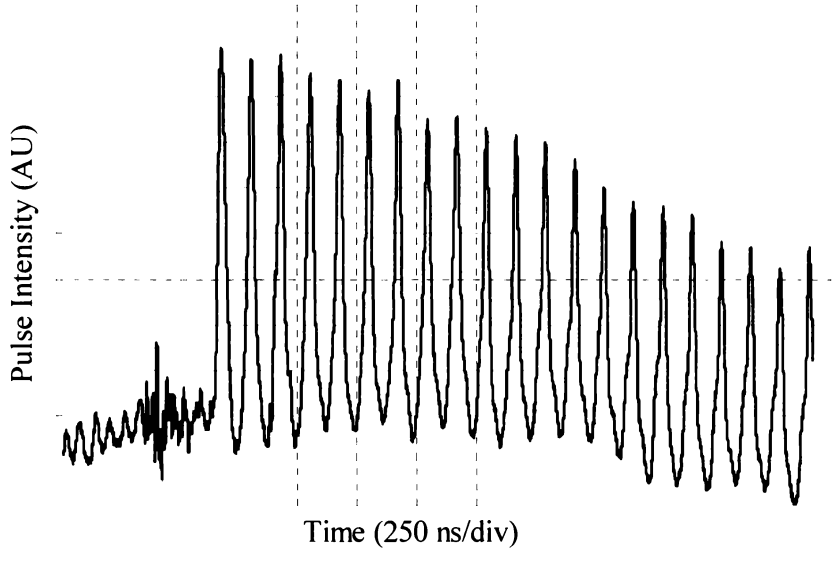

Figure 6. 10 - Output pulse train of the storage loop without PC and TF.

During the overshoot of the gain caused by the noise of the amplified spontaneous emission, the reference pulses show large oscillations. When the pump power is over this critical value, the free running laser oscillation starts, and the gain of the erbium-doped fibre amplifier is clamped. In practice, the pump power should be adjusted just below lasing threshold when the signal is plugged in to avoid lasing oscillations.

After the polarisation controllers and tuneable filter were added into the storage loop, pulses with more equal amplitudes were obtained. The tuneable filter was set to the signal wavelength and the polarisation controllers' angles were precisely adjusted to give the best pulse train.

The waveform is shown in Figure 6.11. It shows that most of the noise has been removed, and only the main peak of the signal remains. The gain of erbium-doped fibre amplifier can compensate for the losses caused by the components of the storage loop and can be adjusted slightly below the lasing oscillating threshold. The reference pulse amplitudes are much more stable (average variation of ± 3.8 %) than

those shown in Figure 6.10 (maximal variation of 47.9 %) The pulse spacing is improved from ± 2.1 % to ± 0.5 %.

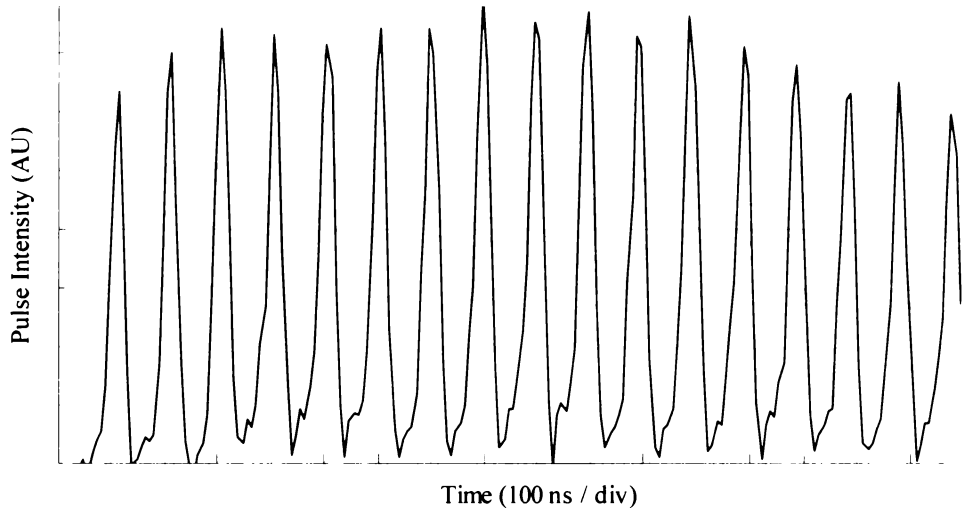

Figure 6. 11 - Output Pulse train waveforms of the storage loop in time domain.

6.4 Beat signals without Doppler shift

To measure small Doppler shifts the measurement beam reflected by some scattering particles in the atmosphere would be optically mixed with a reference beam. To produce a beat signal the reference beam must remain coherent and travel an equivalent path to the measurement beam. This situation can be simulated by mixing the upshifted and downshifted beam after the measurement beam has been delayed by some length of optical fibre.

It has been shown above that the storage loop can generate a reasonably stable pulse train. In this section we will demonstrate that the pulse train remains sufficiently coherent to mix with the measurement beam and generate beat signals at various delays of the measurement pulse.

Beat signals were obtained using the set-up illustrated in Figure 6.12, which is basically a combination of the design shown in Figure 6.5 with an amplified storage loop. Changing the length of the delay fibre produces beat signals at different points in time or different reference pulses. The lengths of the beam delay fibre were from 25 m to 450 m in intervals of 25 m, which corresponds to the length of the storage loop. Figure 6.13 shows the lengths of beam delay fibres. The given values are

nominal only because short pieces were added to either the storage loop or the measurement beam delay to compensate for errors in measuring fibre lengths and to accurately match reference and measurement pulses.

The lengths of beam delay fibre were cut manually. As the path length increases it becomes more and more difficult to match reference and measurement pathlength close to or within the coherence length of the laser. As a result the intensity of the beat signal drops, the signal to noise ratio increases with increasing delay pulse number, and it is very hard to generate beat signals. Beyond the 16^{th} pulse the beat signals were very difficult to distinguish from the overwhelming noise. In total sixteen amplified reference beam pulses were achieved before noise deteriorated the beat signal too much.

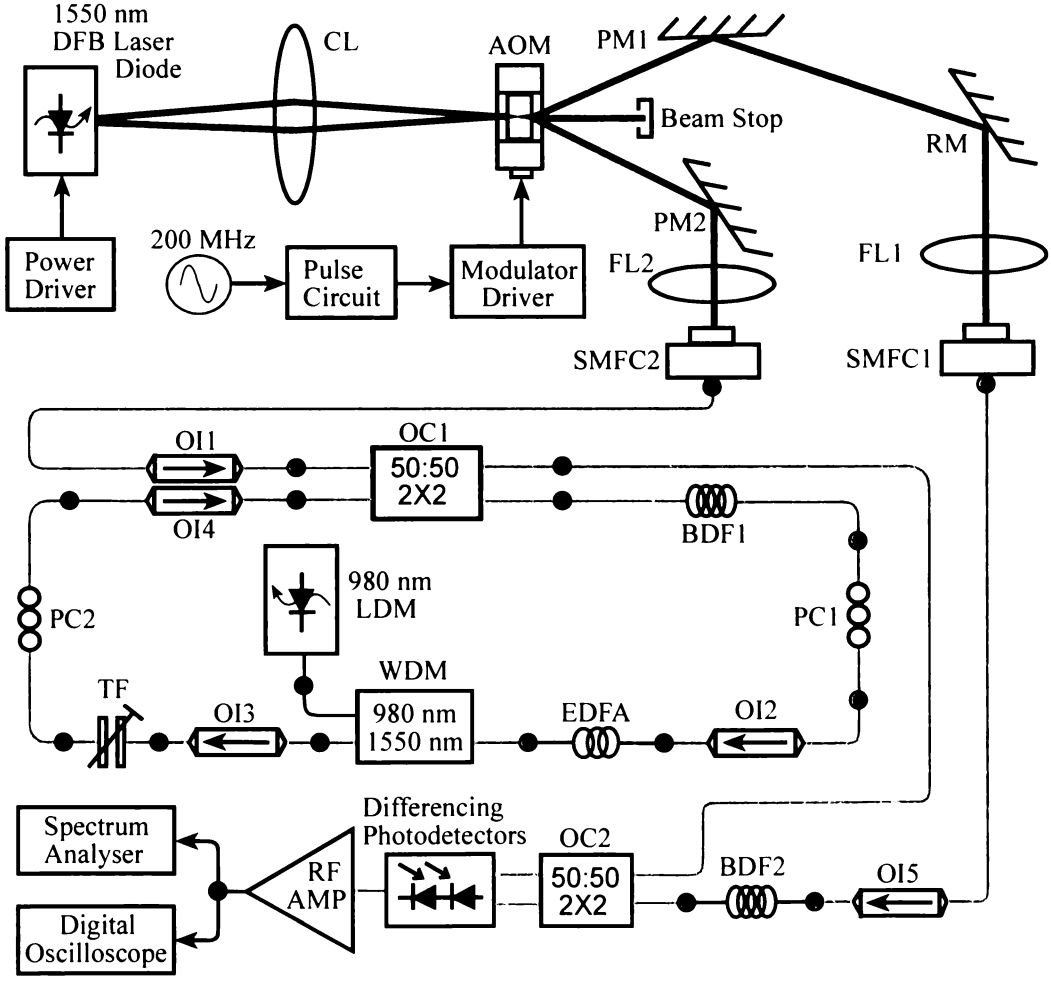

Figure 6. 12 - Experimental setup for measurement of beat signals.

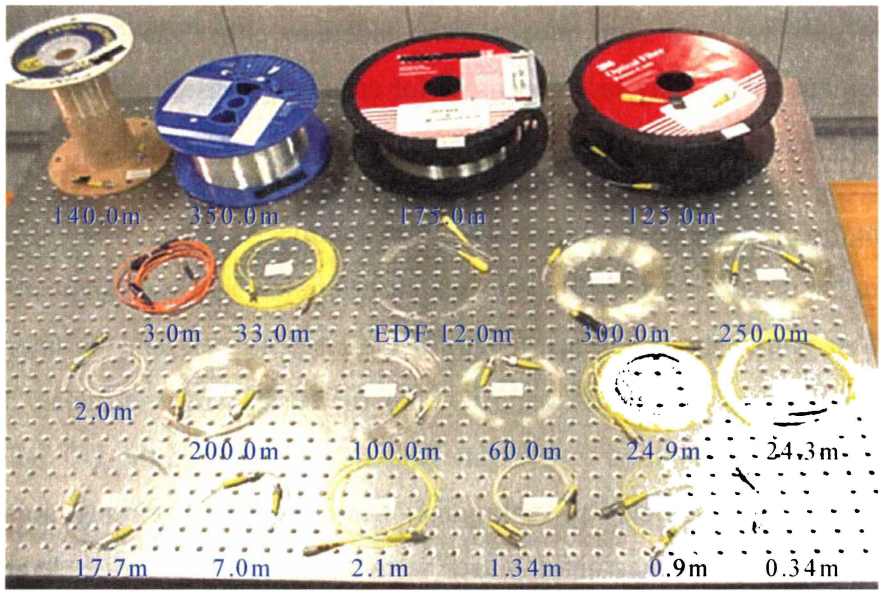

Figure 6. 13 - Various beam delay fibre used in the amplified reference beam storage loop.

Figure 6.14 illustrates the beat signal for some delay fibre lengths. The beat signal for the first pulse (no beam delay) is shown in Figures 6.14 (a) and (b) in time and frequency domain, respectively. The first beat signal has an average peak value of 44.21 dBμV and average noise of 10.76 dBμV/√Hz.

Figure 6.14 (c) and (d) shows the 4th beat signal of 42.07 dBμV average peak value and 11.54 dBμV/√Hz average noise value.

The sixteenth beat signal using a beam delay fibre of 375 m can be seen in Figures 6.14 (e) and (f). The 16th average peak value is 34.98 dBμV with 14.77 dBμV/√Hz average noise value. All of the 16 beat signals show a centre frequency in the region of 400 MHz and a span of 1.0 MHz between left and right peaks as expected from the 500 kHz pulse repetition rate.

The average beat peak value decreases from 44.21 dBμV to 34.98 dBμV whereas the average noise increases from 10.76 dBμV/√Hz to 14.77 dBμV/√Hz. We found that the average beat peak disappears in noise as the beam delay fibre is increased to more than 450 m.

In Figure 6.14 (e) the pulse amplitude decreases because the storage loop has additional fibre added to compensate for measurement error, but the gain and polarization control of the loop is left unchanged from the original set-up.

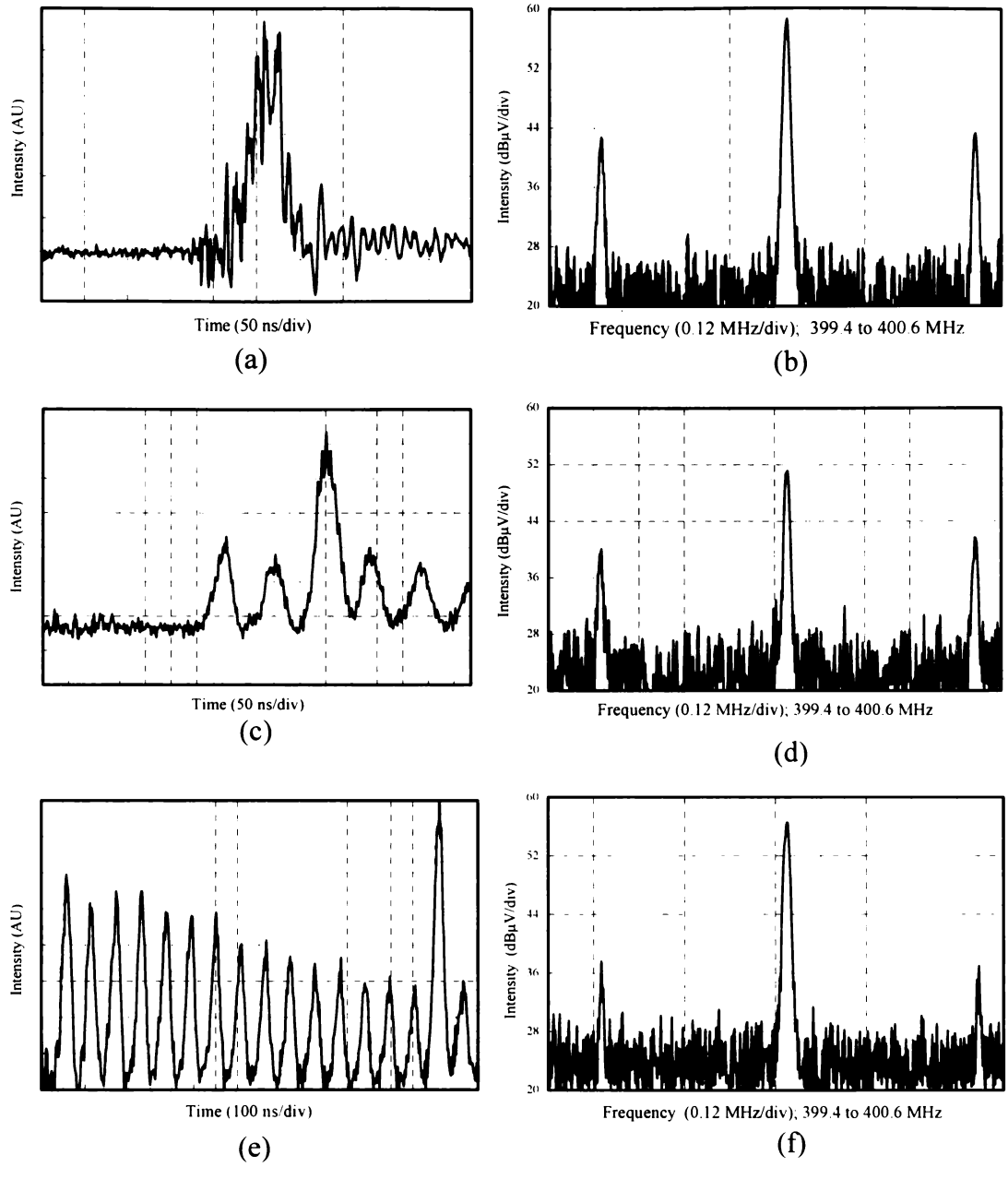

Figure 6. 14 – Intensity of the mixed signal (a), (c), and (e) are the 1st, 3rd, and 16th beat signal in the time domain; (b), (d), and (f) show the frequency spectrum around 400 MHz. Note: The beat signal is the small modulation on the largest pulse.

For further illustration, a program reads data files from the oscilloscope and carries out Wavelet de-noising. The Matlab function Blackman.m is used to break the de-noised data into 17 time slots. A FFT then converts the time sliced data to the frequency domain. Finally the program plots 3-D graphs of the beat frequency versus time.

A flow diagram illustrating the processing algorithm is shown in Figure 6.15, and the code used is included in Appendix I. The signal processing code was written and

produced by MATLAB 6.0 software then executed through STATISTICA 6.0 to produce frequency domain 3D plots.

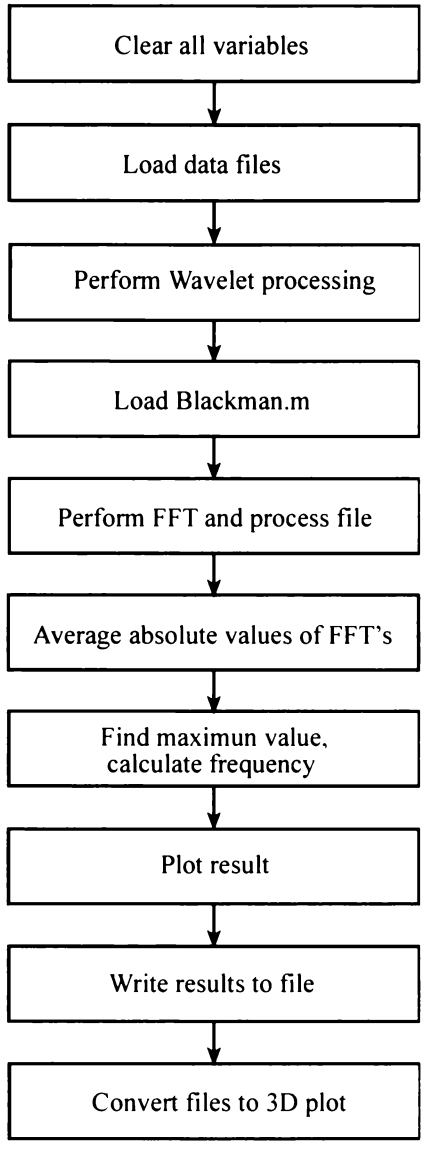

Figure 6. 15 - Flow diagram of the processing algorithm used to execute a FFT producing 3-D plots in time and frequency domains.

Figure 6.16 illustrates the frequency spectra in each time slot for (a) the first beat signal, (b) the third beat signal, and (c) the sixteenth beat signal. A time slot corresponds to a time interval of 100 ns.

(a)

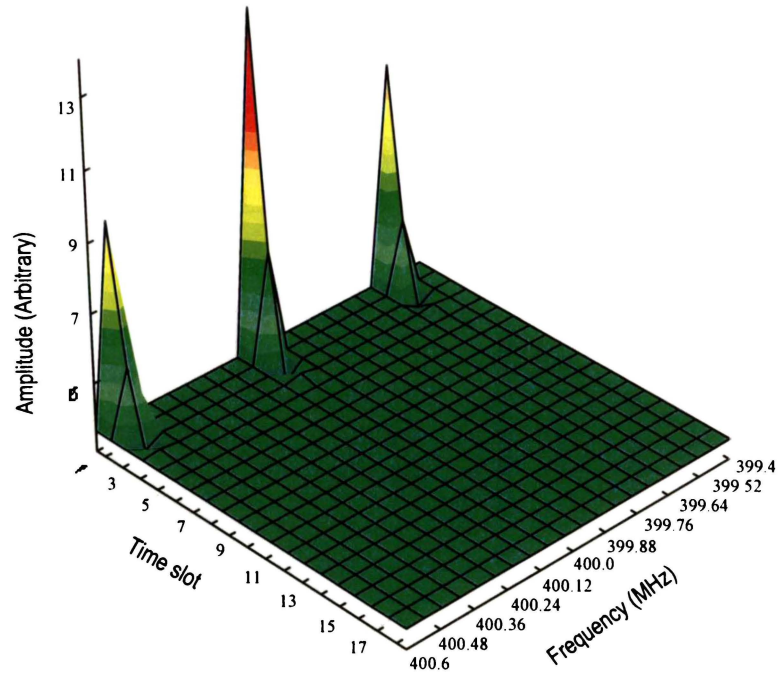
Amplitude (Arbitrary)
13
11
9
7
Time slot
3
5
7
9
11
13
15
17
Frequency (MHz)
399.4
399.52
399.64
399.76
399.88
400.0
400.12
400.24
400.36
400.48
400.6

(b)

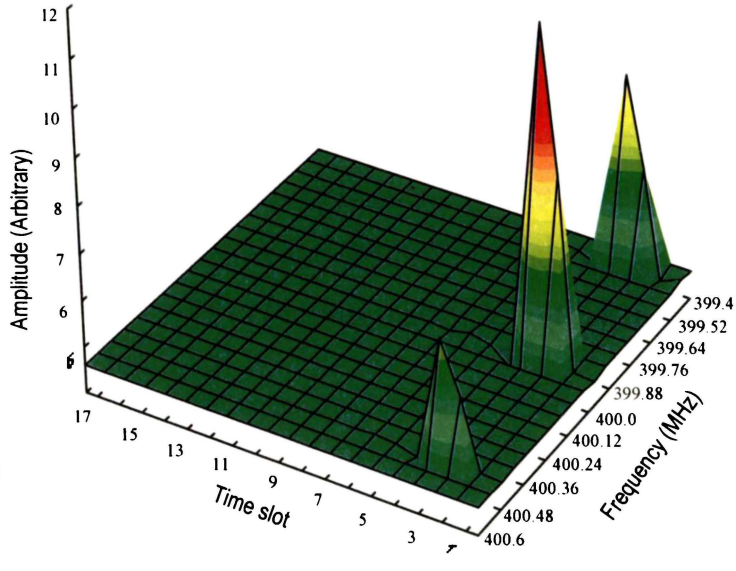
Amplitude (Arbitrary)
12
11
10
9
8
7
6
Time slot
17
15
13
11
9
7
5
3
Frequency (MHz)
399.4
399.52
399.64
399.76
399.88
400.0
400.12
400.24
400.36
400.48
400.6

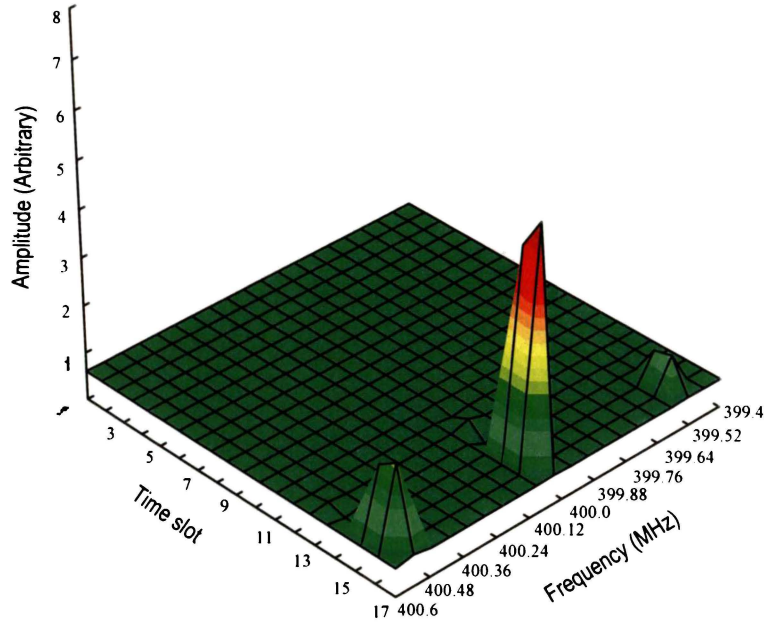

(c)

Figure 6. 16 - Frequency & time domain plots from experimental results for (a) the first beat signal (b) the third beat signal (c) the sixteenth beat signal. Note: Only the top part of the spectrum is shown for clarity. The bandwidth of the spectrum is much wider than what it appears to be here.

Figure 6.17 displays the signal and noise for the first 17 beats between reference and measurement beam pulses. It can be seen that in Figure 6.17 (a) the first 13 beats have the same intensity at a higher signal compared to the last four beats, i.e. above 40 dBμV for the first 13 compared to about 36 dBμV in the last four beats.

Figure 6.17 (b) shows the change of noise level extending from 10 dBμV/√Hz to 15 dBμV/√Hz. There was some little fluctuation over the first 13 beats, followed by an obvious increase of 4 dBμV/√Hz from pulse 14 to 17.

In general, these last four beats show the level of noise increasing steadily while the signal intensity appears to slowly decay. Overall, the system is very stable with little difference in signal and noise from beat one to beat 17.

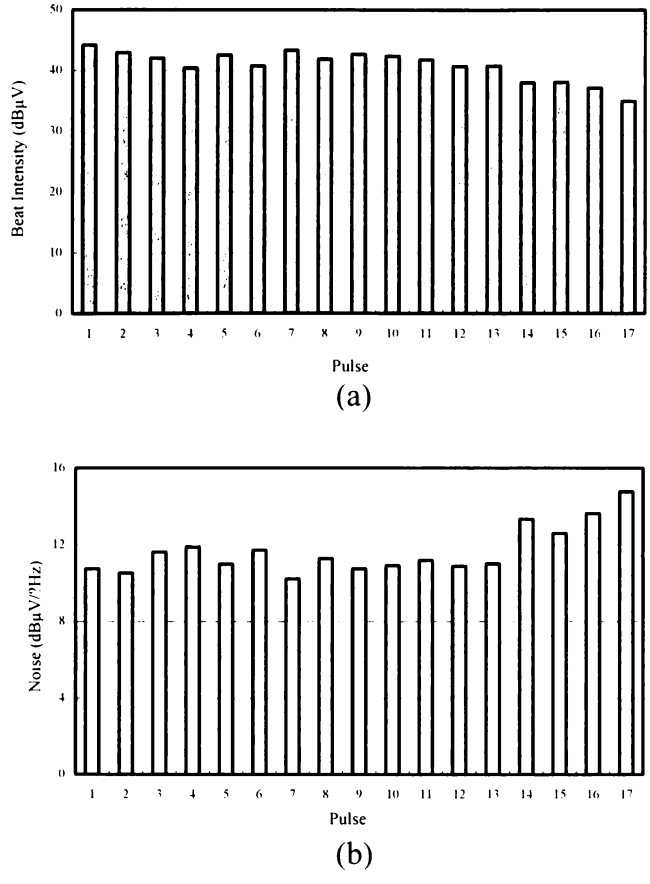

Figure 6. 17 - (a) the signal and (b) noise for each of the 17 beat signals.

6.5 Velocity measurements

In the previous section we have shown that the amplified reference beam storage loop produces a stable pulse train, which can be optically mixed with a measurement beam. However, in practice the measurement pulse would be Doppler shifted by the moving air from which it is scattered. This effect can easily be simulated by the insertion of a rotating mirror into the path of the measurement beam. The experimental design is discussed in more detail in the following sections.

6.5.1 Optical arrangement

By inserting a rotating mirror in the measurement beam instead of a stationary planar mirror the signal will be frequency shifted in proportion to the speed of motor rotation. Varying the rotational velocity of the mirror, which can be altered by an adjustable speed motor, simulates differing velocities of the target.

A schematic diagram illustrating the set-up of the validation experiment is shown in Figure 6.18 and a photograph in Figure 6.19. This is an identical design to that in the previous section, with the exception of the rotating mirror, tachometer and the phase locked loop demodulation circuit. Measurements were taken at ten different rotation speeds, simulating ten different wind speeds. These results were then compared to the mirror velocities obtained by a tachometer. The phased locked loop demodulation circuit decreases noise levels from the radio frequency amplifier as mentioned in Chapter 4.

To obtain an independent velocity measurement a tachometer is included in the set-up. This consisted of a 632 nm laser diode and a photodetector connected to a frequency counter and was used to monitor the rotation rate of the mirror (Figure 6.18 and 6.20). The 1550 nm and 632 nm light beams were shone on opposite sides of the mirror to separate the beams and simplify the optics. The beams need to be off-centre because on the rotation axis the mirror is not actually moving. It is stationary, and no Doppler shift will be generated. The 632 nm laser diode light was reflected by the rotating mirror onto a detector, and its frequency was counted.

The conversion from Doppler shift frequency $\Delta\nu$ to rotation velocity υ is carried out with the equation given by Drain (1980):

$$\Delta\nu = \frac{2\upsilon\cos\theta}{\lambda} \qquad 6\text{-}6$$

where $\Delta\nu$ is the Doppler frequency shift, υ is the speed of a point on the mirror, and θ is half the angle between the incident and the reflected measurement beam. The angle 2θ is approximately $2/3\,\pi$ radians by construction. Hence the Doppler shift frequency is

$$\Delta\nu \cong \frac{\upsilon}{\lambda} \qquad 6\text{-}7$$

where the speed υ is determined by

$$\upsilon = 2\pi\, r \times \frac{f_c}{2} \quad . \qquad 6\text{-}8$$

r is the radial distance of the measurement spot, and f_c the rotating frequency displayed by the frequency counter. The lidar beam was positioned at a distance r = 0.005 m ± 10 % from the rotation axis. Therefore, a tachometer frequency, f_c, of 63.66 Hz corresponds to a velocity of 1.0 m/s ± 5 % at the measurement location.

f_c (Hz)	64.7	127.3	191.0	254.7	318.3	382.0	445.6	509.3	573.0	636.6
υ (m/s)	1	2	3	4	5	6	7	8	9	10

Table 6. 1 - Tachometer frequency versus velocity.

By adjusting the autotransformer, we can vary the output AC voltage to the motor of the rotating mirror, and select the velocities indicated in Table 6.1.

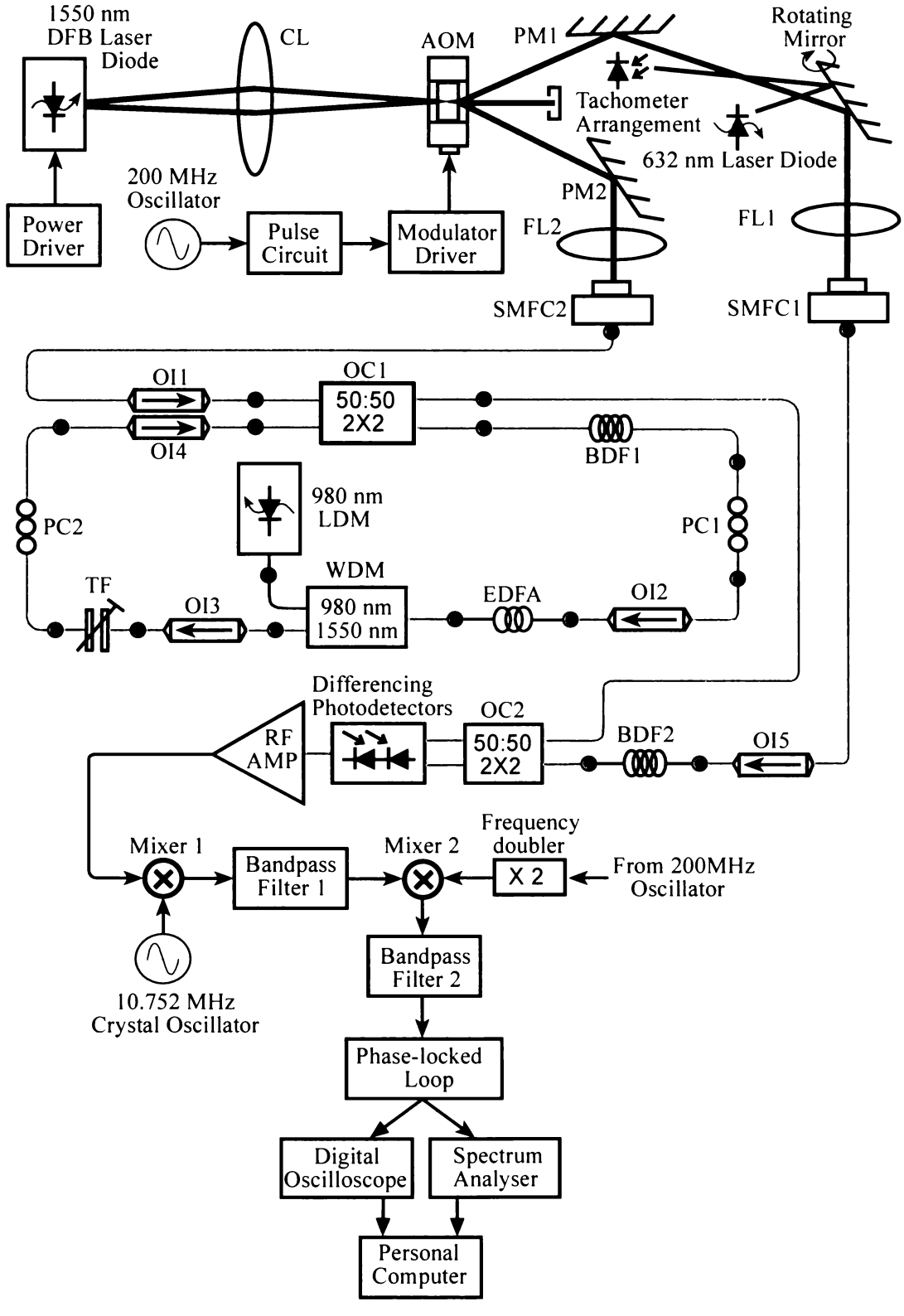

Figure 6. 18 - The full experimental set-up of lidar system used for velocity measurement.

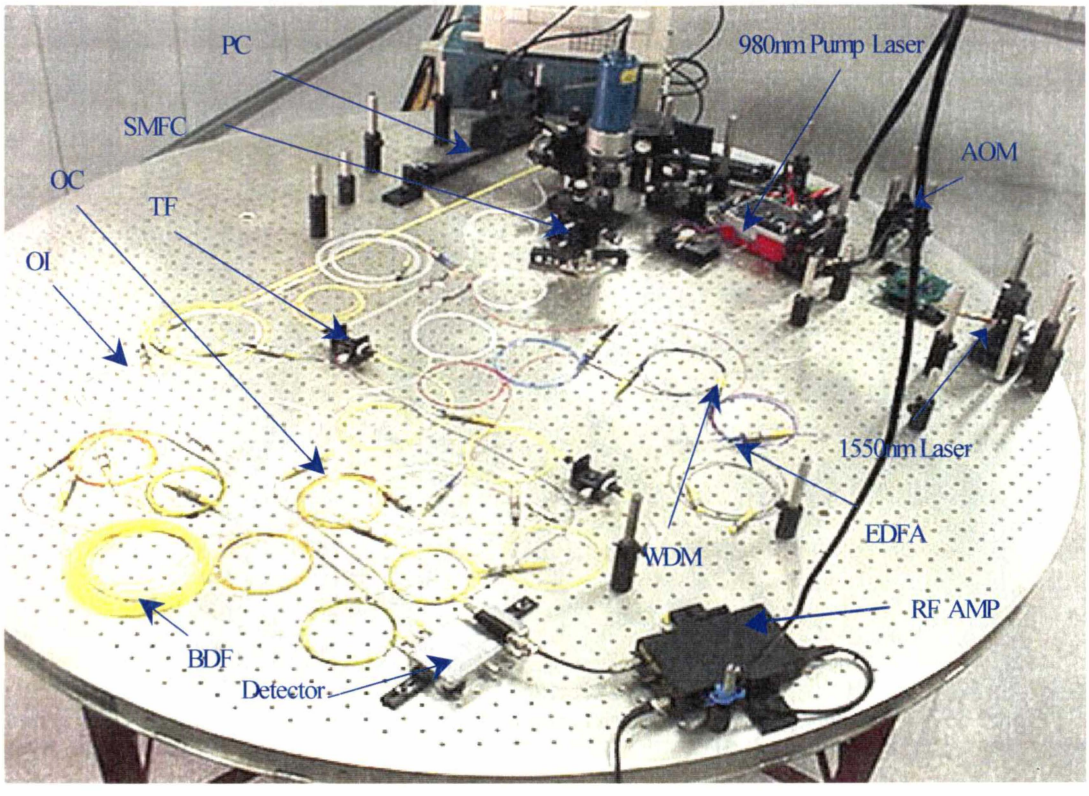

Figure 6. 19 - The photograph of the full experiment set-up of lidar system.

6.5.2 Experimental validation

To optimise the rotating mirror set-up we need several separate steps: Firstly, we need to ensure sufficient light is reflected from the rotating mirror; then we measure the Doppler shifted beat signal and finally make a direct conversion from frequency shift to speed.

6.5.2.1 Light reflected from a rotating mirror

The 1550 nm light is undetectable by the human eye, and the window in the rotating mirror is too narrow to fit a sensor card as shown Figure 6.20. Two methods were used to test that the 1550 nm light is on the correct spot of the mirror and produces maximum reflection of light.

The first step of the alignment was to use a continuous wave and the next step was to use a pulsed laser. The second step monitors the rotation speed of the mirror using a tachometer arrangement and calculates the Doppler shift of the beat signals. By knowing the Doppler shifted frequencies, we can then calculate the velocity of the rotating mirror.

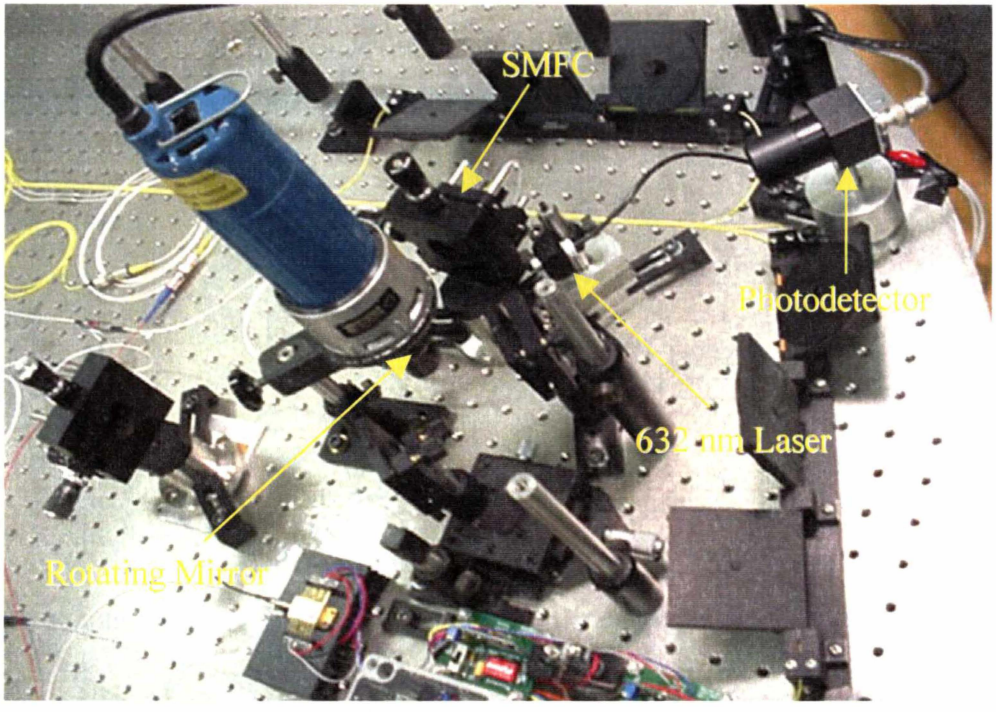

Figure 6. 20 - The enlargement of tachometer optical arrangement in the new design lidar system.

6.5.2.1.1 Continuous wave mode

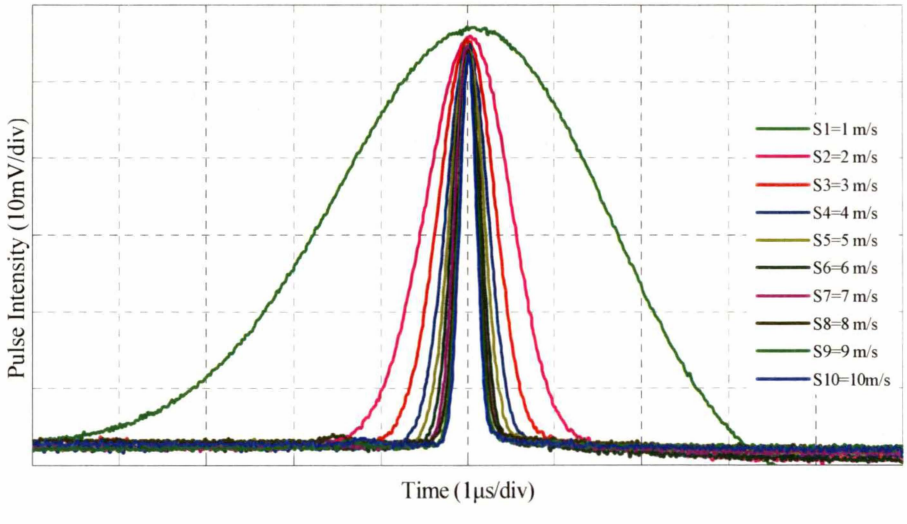

Figure 6. 21 - The reflected beam from the rotating mirror in continuous wave mode.

The results from the continuous wave mode are shown in Figure 6.21 using the set-up from Figure 6.18 with the reference beam disconnected, no pulse circuit, and no phase lock loop arrangement. In addition, the modulator driver was adjusted to a maximum power of 2.0 W.

The results are for ten speeds of the rotating mirror from 1.0 m/s through to 10 m/s (referring to Table 6.1). It is evident that at lower speeds the intensity is spread over

a larger time period. As the speed increases the intensity becomes sharp, that is a high intensity over a short time interval. The pulse width is in the range from 0.5 μs to 2.5 μs for all speeds except 1.0 m/s at 7 μs. It is also evident that the noise from the rotating mirror does not affect the light beam. This is desirable as the intensity from the original signal is the same as the reflected signal.

6.5.2.1.2 Pulsed mode

The results from the pulse mode are shown in Figure 6.22 using the set-up from Figure 6.18 without the reference beam. The same ten speeds as for the continuous wave mode were used to measure the reflecting light from the rotating mirror. At all speeds, except for 2 m/s, the intensity is about the same.

Figure 6.22 (a) shows the output signal that has not passed through the phase locked loop demodulator circuit. With an appropriate phase-locked loop arrangement the noise is significantly reduced. Figure 6.22 (b) shows the improvement at 34.93 dB signal to noise ratio. An explanation for the difference between the figures is that the rotating motor caused vibrations.

By using the phase locked loop demodulator circuit, the reflected light signal is a stable pulse, whereas the peak of the bypassed signal varies by 6.75 dB, is unstable, and affected by high frequency noise (measured noise is 11.99 $dB\mu V/Hz^{1/2}$ at 400.053 MHz). When the signal is passed through the phase locked loop, the noise is reduced to 5.24 $dB\mu V /Hz^{1/2}$ at 400.029 MHz.

The pulse width of approximately 108 ns (FWHM) does not vary with rotation rate unlike in the continuous wave mode. This makes the pulsed laser mode better suited to the situation, as the time spent on the mirror would be long enough to obtain the information to detect Doppler shifts.

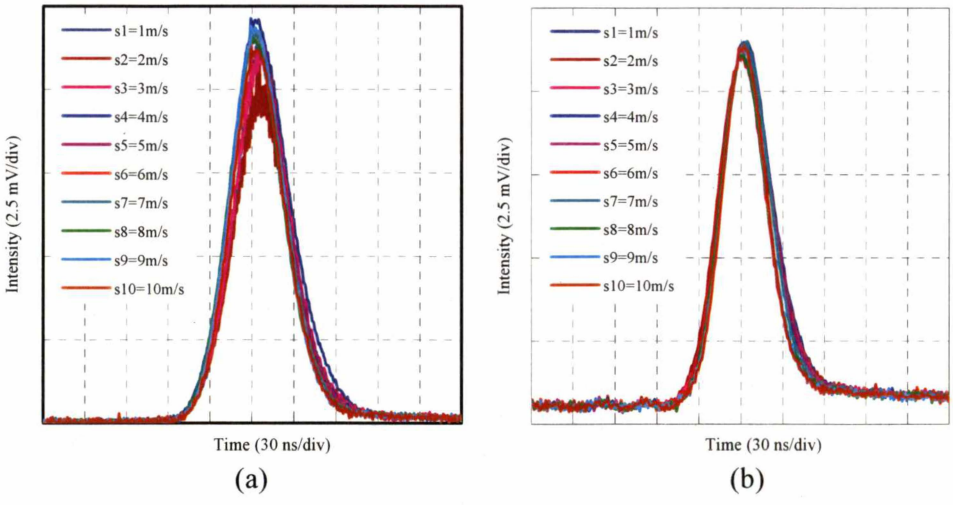

Figure 6. 22 - The reflected light from the rotating mirror for pulsed laser mode (a) without phase-locked loop circuit; (b) with phase-locked loop demodulation.

6.5.2.2 Doppler shift measurements

Suppose the frequency of the incident laser beam is v_0 and the frequency shift from the acousto-optic modulator is f_S, then the upshifted and downshifted beams have a frequency v_R (reference beam) and v_M (measurement beam) respectively (Figure 6.23). The up-shifted frequency is the addition of the initial beam and the shift frequency. The downshifted frequency is the difference between v_0 and f_S.

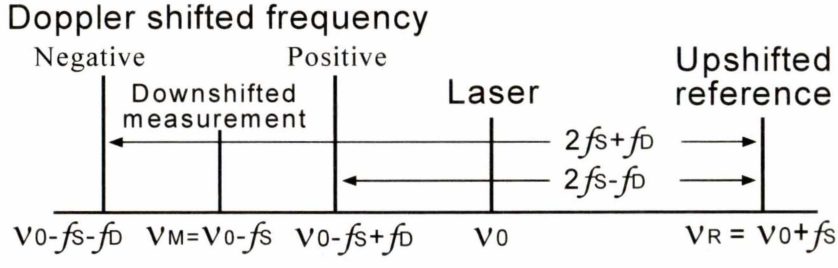

Figure 6. 23 - Diagram illustrating the beating of two Doppler shifted beams with a frequency shifted measurement beam.

If the Doppler shift frequency is f_D, the frequency of the scattered light is either (v_M + f_D) or (v_M - f_D) dependent on the direction of velocity. Beating with light of the measurement frequency v_M produces a signal of frequency f_D in either case, but if the reference beam is used the corresponding beat frequencies are ($2f_S$+ f_D) and ($2f_S$ $-f_D$). Thus, directional discrimination is possible.

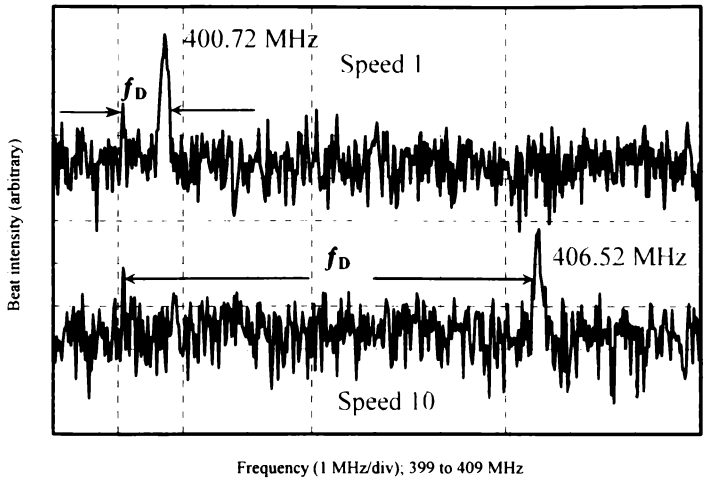

Figure 6. 24 - Beat frequency spectrum using reference pulse one at speed 1 (upper trace) and speed 10 (lower trace).

Figure 6.24 illustrates the frequency spectrum of the beat signal for the first reference pulse. The top trace is measured at speed 1 generating a beat signal at 400.72 MHz and the lower trace at speed 10 resulting in a frequency peak at 406.52 MHz. The Doppler shift frequencies f_D can be found from

$$f_D = f_p - 2f_s \quad , \qquad 6\text{-}9$$

where f_p is the beat peak frequency, and f_S the modulation frequency, as

$$f_{D,\text{ speed 1}} = 400.72 \text{ MHz} - 400.072 \text{ MHz} = 0.648 \text{ MHz}$$

$$f_{D,\text{ speed 10}} = 406.52 \text{ MHz} - 400.072 \text{ MHz} = 6.448 \text{ MHz}$$

The velocities derived using equation 6.7 are then

$$V_1 = f_D * \lambda = 0.648 \text{ MHz} * 1.55 \text{ μm} = 1.0044 \text{ m/s.}$$

$$V_{10} = f_D * \lambda = 6.448 \text{ MHz} * 1.55 \text{ μm} = 9.9944 \text{ m/s.}$$

The beat signal for speed ten has a beat intensity of 39.41 dBμV and a noise of 19.17 dBμV/√Hz at 406.52 MHz.

Figure 6.25 illustrates the Doppler burst spectra for three-selected reference pulses at ten various speeds of the rotating mirror. Figure (a) is the superposition of 10 spectra each at a different speed for reference pulse one, Figure (b) for pulse 3, and (c) for

pulse 16. The first peak in each diagram is noise produced by the modulator driver at a frequency of 400.072 MHz. The following peaks are beat signals corresponding to the ten different speeds.

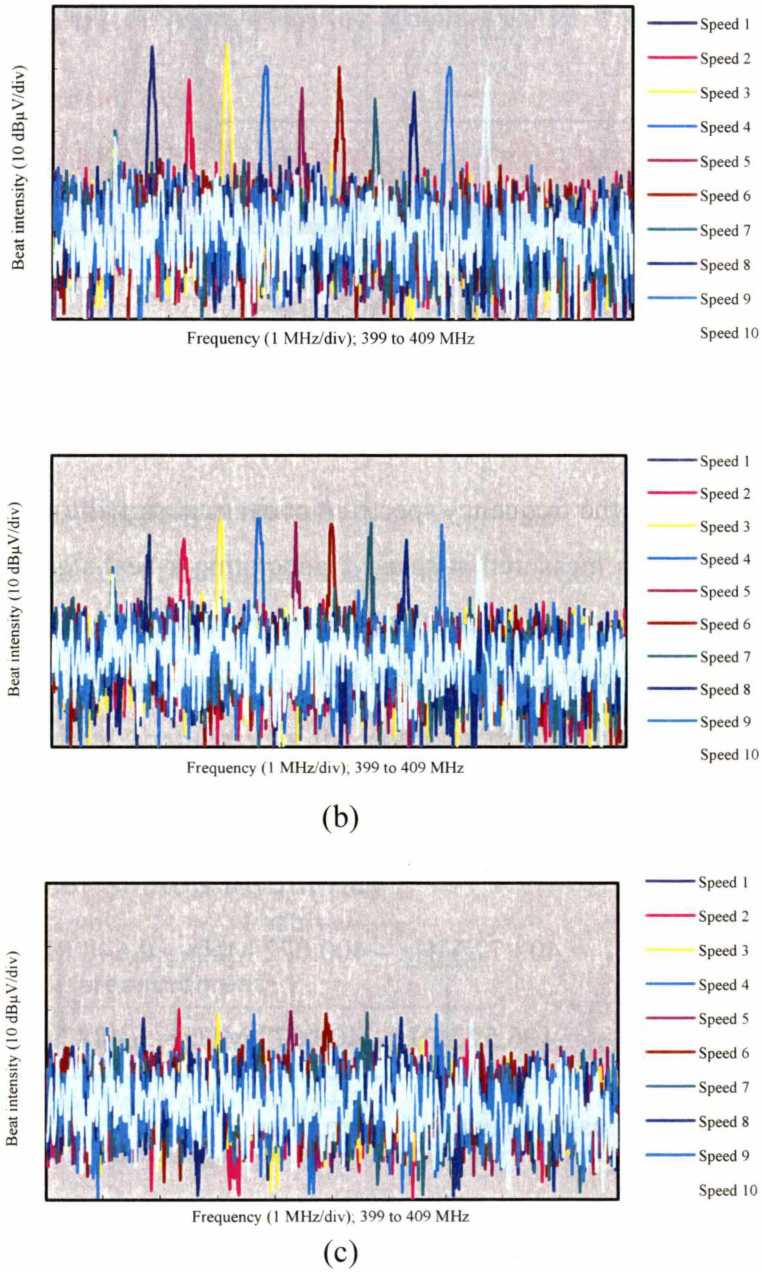

Figure 6. 25 - Doppler burst spectra at 10 speeds for the first (a), third (b) and sixteenth (c) reference pulse.

It can be seen from Figure 6.25 that the intensities of the beat for pulses 1, and 3 are relatively constant and well above the noise level. However, the beat intensity of pulse 16 (Figure 6.25 (c)) is almost overcome by noise, making it very hard to distinguish between noise and burst signals.

The decrease in signal for long delay fibre lengths is not surprising as these fibres consist of several pieces connected by FC/PC connectors, for example 375 m (nominal) of beam delay fibre was made up of 17.7 m, 24.3 m, 33.0 m and 300 m of beam delay fibre. Consequently, extra pumping power is needed to compensate the loss caused by the fibre connectors, Harris *et al.* (1998).

6.5.3 Velocity measurement results

Figure 6.26 is a box plot of the validation experiments. The mean, the standard deviations, and the maximum values of the measured velocities for each of the sixteen reference pulses is plotted versus tachometer measured velocity.

The mean value for the first nominal speed of 1 m/s is 1.11 m/s (±0.14 m/s) for all sixteen pulses. The minimum and maximum values are between 0.86 m/s and 1.30 m/s. Speed one has the largest standard deviation and difference between minimum and maximum value. These values decrease with speed and reach a minimum at 8 m/s after which they increase.

The correlation between the Doppler and Tachometer measured velocities is very good: R^2=0.9998. Only speed 1 seems to deviate slightly from the nominal velocity. All speeds agree with the nominal velocity within plus or minus one standard deviation, and all measured data lies within three standard deviations of the actual velocity. This means that the system can accurately measure the velocity of the rotating mirror to well within ±0.14 m/s.

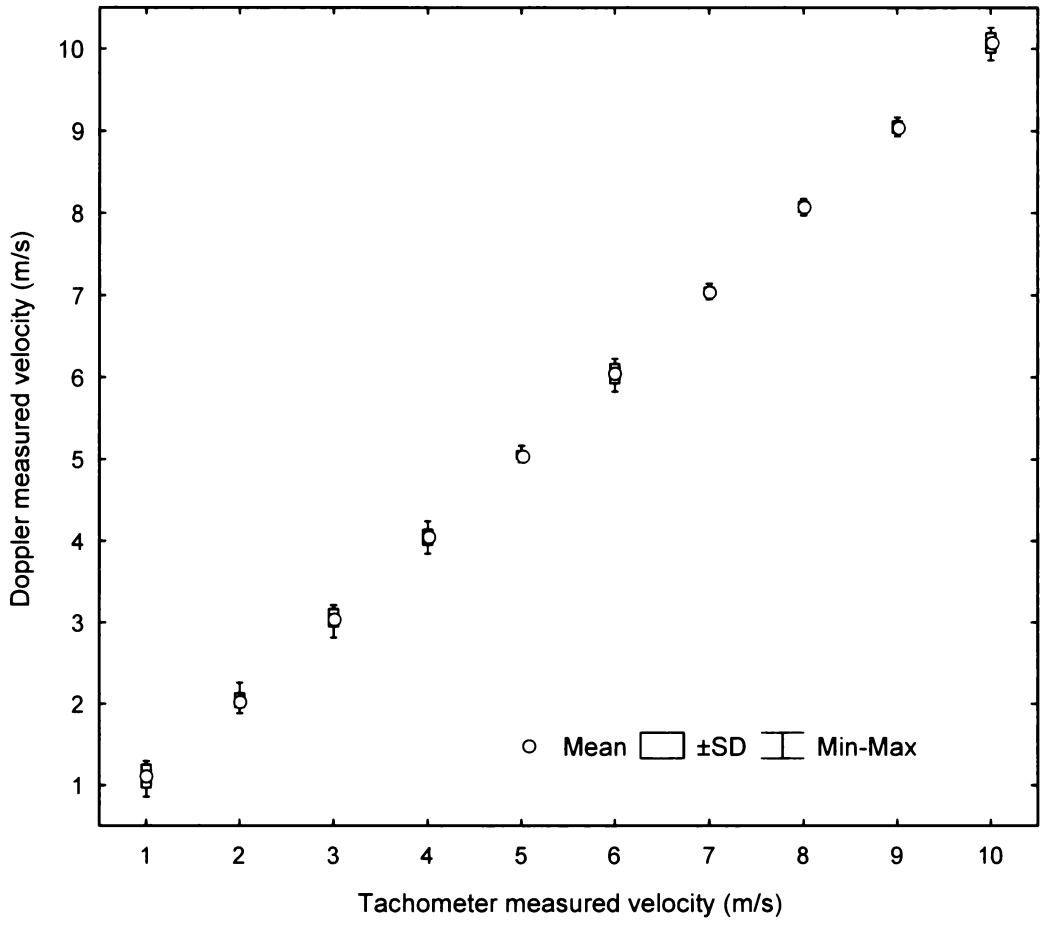

Figure 6. 26 - Doppler measured versus tachometer-measured velocity for pulse 1 to 16.

To analyse the results from the previous section, we consider the relative difference, Δv, between the tachometer velocity, v_T, and the Doppler measured velocity, v_D, that was derived in the previous section:

$$\Delta \upsilon = \frac{\upsilon_D - \upsilon_T}{\upsilon_T}. \qquad 6\text{-}10$$

Figure 6.26 illustrates that the relative velocity difference (in percent) at low rotation speeds is much greater than that at higher speeds. A drift in the motor speed might cause this. The tachometer uses a frequency counter, which averages over a relatively long period compared to the very fast Doppler measurement pulse. During this time interval the speed can change without the tachometer displaying any difference. Also, at low rotational speed the rotating mirror is less stable and vibrations might cause the measuring spot to move radially away from the axis. This would result in different speeds observed by the measurement beam.

The maximum relative velocity difference between the Doppler measured velocity and tachometer-measured velocity for the first four pulses is 3 % (Figure 6.27(a)), for the second four pulses 3.8 % (Figure 6.27(b)), for the third pulses 5 % (Figure 6.27(c)), and for the last pulses 6 % (Figure 6.27(d)). This means that the system could be accurate to 95.5 % over all sixteen pulses. Generally all pulses show a ± 2 % velocity difference at 2 m/s improving to within ± 0.6 % at higher speeds.

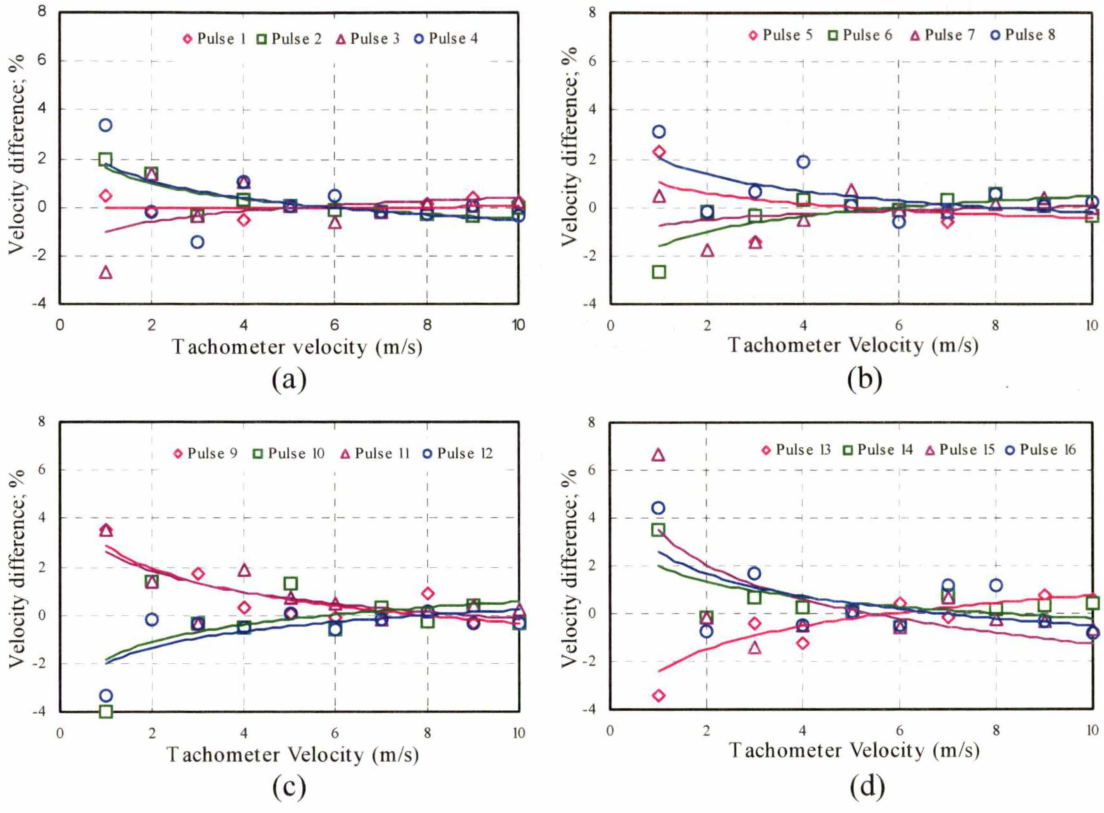

Figure 6. 27 - Doppler measured velocity difference in percentage.

Figure 6.28 illustrates the signal to noise ratio for pulses one to sixteen. It averages about 20 dB for the first pulses, and then decreases to 14.5 dB for pulse 16. A trend line shows the variation of the signal to noise ratio with velocity for each pulse. Pulses one to four show a rise in signal to noise ratio from 1.0 m/s to 10.0 m/s; for the following twelve pulses there is a slight linear decrease in signal to noise ratio.

This can be explained by the insertion of fibre connectors after pulse four, which are required to make up the necessary delay fibre length and has already been discussed in section 6.4 to increase the beam delay fibre length. Therefore, the gain of the

erbium doped fibre amplifier cannot maintain the amplitude of the later reference pulses and hence the signal to noise ratio decreases.

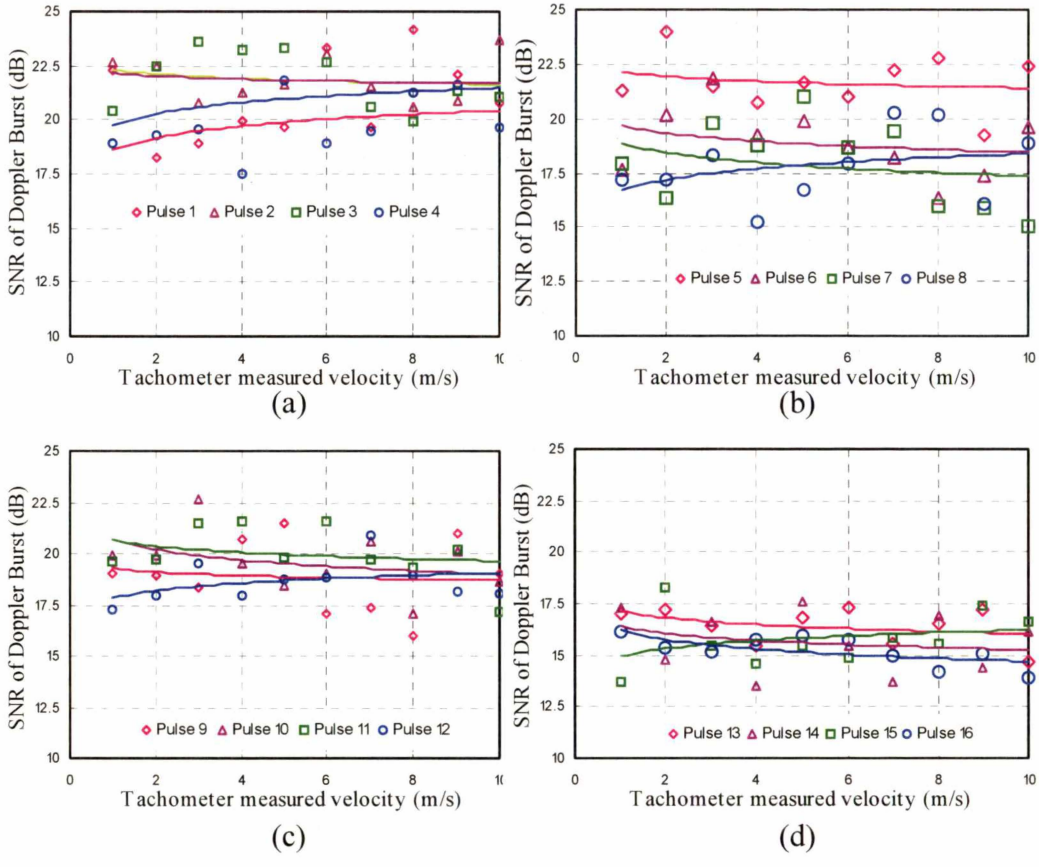

Figure 6. 28 - Signal to noise ratio of Doppler burst signal.

6.6 Signal processing and noise

In the previous section, we have used the frequency data from the spectrum analyser to convert the Doppler signal into velocity. Due to the nature of the burst signal and the low number of data points available per sweep (500), the accuracy of the speed calculation is limited to 0.6 %, and it is very difficult to identify the frequency maximum when the noise is getting higher.

An alternative method, which would also be more relevant to a real, low cost measurement system, is to use time domain data and process these on the computer. Therefore, time domain data measured by the oscilloscope was recorded and was processed by using a one-dimensional continuous wavelet transform that offers the means to de-noise signals in the time domain (Matlab 6.0 software). The code is

provided in Appendix II, Code-1. When a signal's spectral content varies over time, this processing readily isolates undesired components that appear and disappear. Components that undergo changes in amplitude and frequency with time can also be characterized. This procedure also offers a greater flexibility than the previous hardware processing for noise removal.

Figure 6.29 (a) shows a signal that has not been processed. With appropriate wavelet processing, the noise in the Level 1 LF signal is significantly reduced. Figure 6.29 (b) shows the improvement (bottom trace). The top trace represents the Level 1 HF signal, which has a significant high frequency noise component. For illustration of the process a beat signal output from phase locked loop is used.

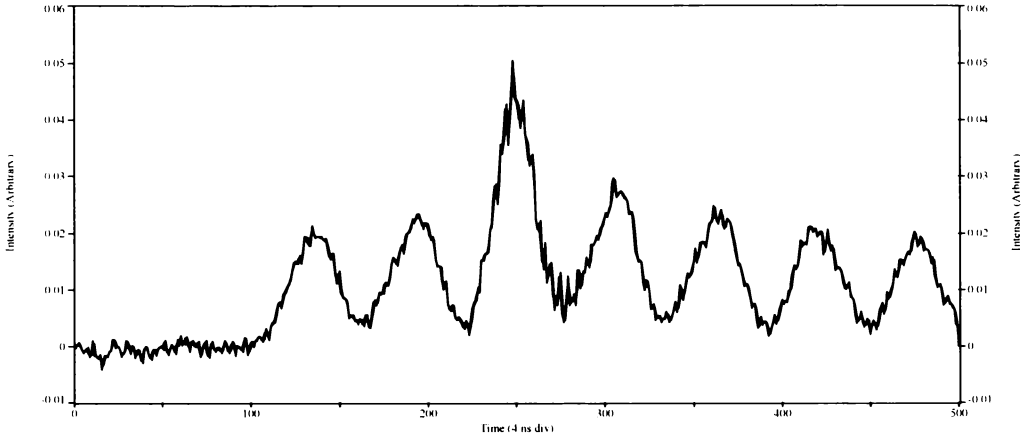

(a)

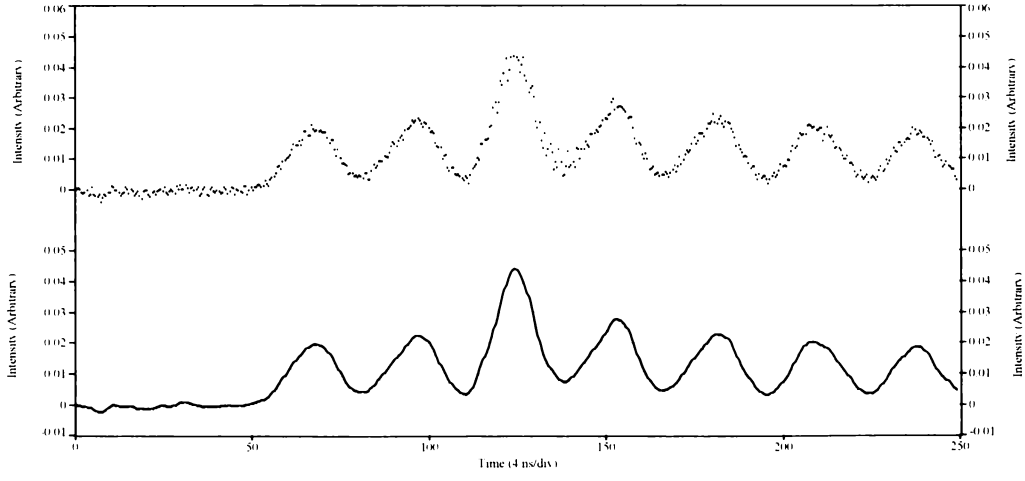

(b)

Figure 6. 29 - (a) without any wavelet processing; (b) Wavelet processed signal. Bottom: Denoised Level 1 LF signal; Top: Level 1 HF signal.

After the wavelet processing, a FFT is applied to derive the frequency of the burst signal (The code is provided in Appendix I.). The frequency can then be converted to velocity in the same manner as before.

At a sampling rate of one 1 Gsample/s of the oscilloscope, the FFT has a Nyquist upper frequency limit of 500 MHz. For 500 time domain points the FFT produces 250 frequency domain points, providing a frequency resolution of 2.0 MHz. At a laser wavelength of 1550 nm, the minimum desired velocity resolution of 0.1 m/s corresponds to 64.5 kHz, which is much lower than the FFT frequency resolution.

The time domain data collected from the experiment by the oscilloscope was converted into frequency, and each frequency point of the wavelet de-noised data was expanded 128 times resulting in a total of 16,000 data points. This obviously increases the FFT frequency resolution and simplifies the determination of the frequency maximum of the Doppler burst, but has the side effect of broadening the peaks, which is called "interpolation theorem" (James, 1995).

The signal processing can now easily find the frequency maximum of the experimental data, but another consideration is whether the method is still successful at higher noise levels. To test this elevated noise levels were simulated.

The flow diagram shown in Figure 6.30 illustrates the signal processing (The Matlab code is included in Appendix II-Code-2). It begins by reading the first simulated burst signal for a given speed (Figure 6.31 (a)). White noise is then generated (Figure 6.31 (b)) and is combined with the burst signal (figure 6.31 (c)). This data is then transformed from the time domain into the frequency domain by a FFT. The process is repeated until all 16 pulses have been read and transformed.

The FFT data is then averaged, because all the burst data were obtained under the same conditions at speed 1 to speed 10 for each reference pulse 1 to 16. After that, the absolute value is calculated and the frequency maximum, f_{max}, is determined and recorded. The whole process is repeated until all ten speeds have been processed. f_{max} is converted into a velocity by equation 6.8, is compared to the actual velocity of the rotating mirror, and the regression co-efficient is calculated from equation 6-11.

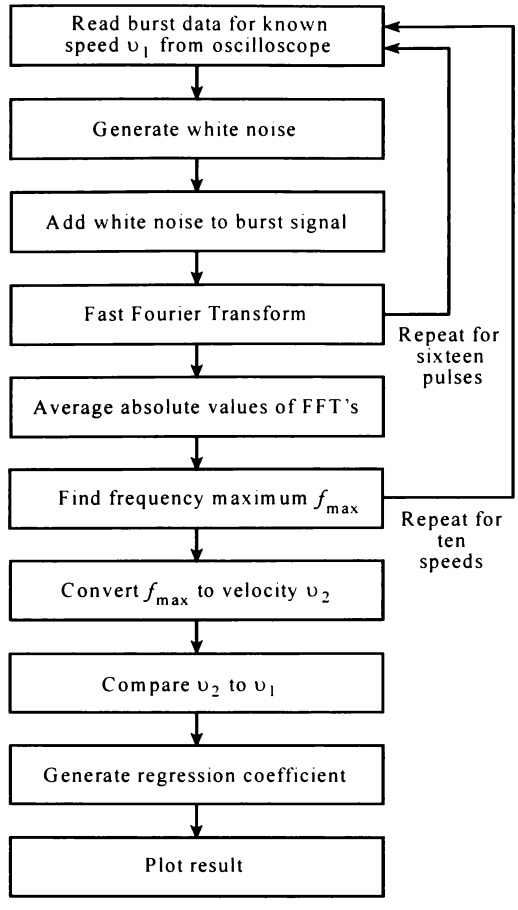

Figure 6. 30 - Flow diagram of the processing algorithm used to perform regressing from experimentally recorded Doppler data.

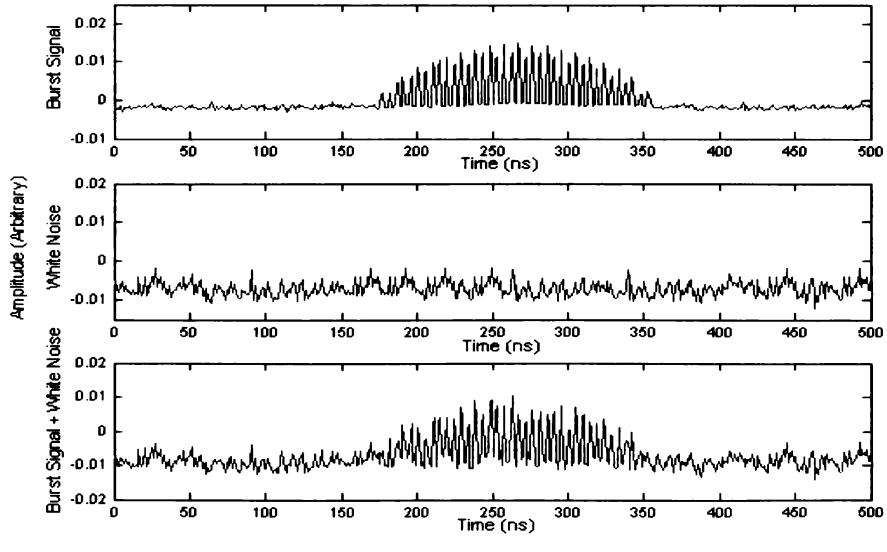

Figure 6. 31 - The waveforms in time domain (a) simulated burst signal; (b) white noise of 31.75 dBμV/√Hz generated by Matlab software; (c) an addition of (a) and (b).

$$R = \frac{\sum_{i}\left(Y_{i1} - \bar{Y}_1\right)\left(Y_{i2} - \bar{Y}_2\right)}{\sqrt{\sum_{i}\left(Y_{i1} - \bar{Y}_1\right)^2 \sum_{i}\left(Y_{i2} - \bar{Y}_2\right)^2}} \qquad 6\text{-}11$$

where Y_1 is the burst signal and Y_2 is the white noise.

Figure 6.32 illustrates the correlation coefficient as a function of white noise, which is given as a multiple of the experimentally measured noise at a level of 12.5 dBμV/√Hz. The value of R^2 remains constant at about 1.0 up to a noise level of 31.75 dBμV/√Hz, about 2.5 times the experimentally measured level. The accuracy of the speed calculation was about 0.5 % for this range. After that R^2 rapidly drops as white noise increases.

It is worth to mention that this test indicated that the expected frequency resolution was achieved by the alternate method and a 2.5 time higher noise level can be tolerated.

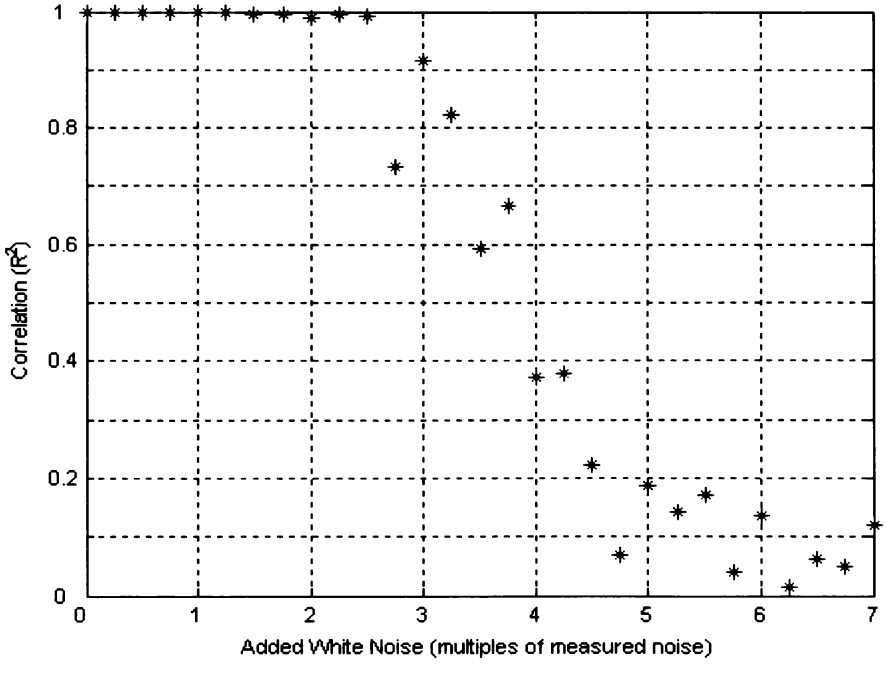

Figure 6. 32 – Correlation coefficient (R^2) for artificial Doppler signals versus white noise, which is in multiples of the measured noise with burst of 12.5 dBμV/√Hz.

6.7 Simulation

To find the maximal number of pulses that could produce useful beat signals in a future commercial system a simulation of the optical arrangement was performed using Matlab 6.0 software (Appendix III). The simulation program will investigate how far this new system can go until it is too much affected by signal losses and noise.

The modelling included the calculation of both measurement and reference beams in forward and backward directions at all the nodes shown in Figure 6.33. The nodes are formed at the connections between two optical components and are indicated by a blue dot. The red arrows show the direction of light propagation and reflection throughout the system.

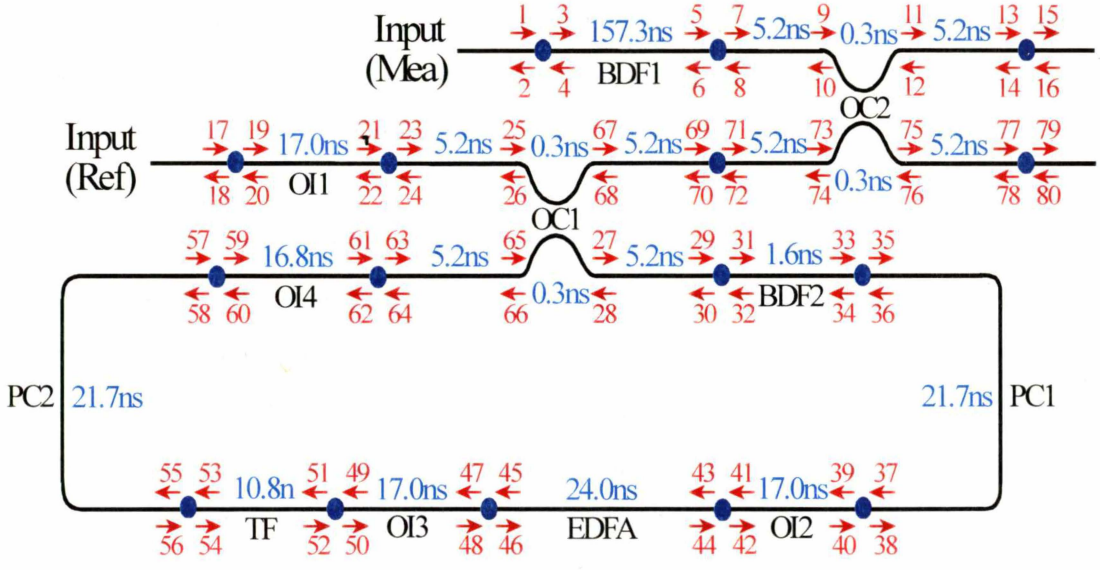

Figure 6. 33 - Schematic diagram of simulation. Nodes are shown in blue, and delay times in light blue.

Figure 6.34 shows the sequence of tasks that the software executes to simulate the storage loops operation. This begins by setting all of the data points that represent the signal propagating throughout the storage loop. The delay time follows and is determined by the component fibre length. Some fibre delay is considered because of different pigtail lengths of the optical components. The delay time is calculated by the total length between connections for each component and is then converted to a time t_d.

$$t_d = \frac{l}{c_0} \times n \qquad 6\text{-}12$$

where l is the connector-connector length of the component, c_0 is the velocity of light in free space and n is the refractive index (1.458 for of the single mode fibre used).

All noise such as ASE, phase noise, laser intensity noise, and electrically induced noise must be considered in the simulations except laser intensity noise. Because the length of the beam delay fibre can be set accurately by the simulation, there are no measuring errors that occur in the real set-up. The noise that is introduced into the simulation is 12.5 dBμV/√Hz; this is the same as the experimentally measured noise.

At each fibre connection the intensity of the measurement beam was reduced to 98 %, and 1 % of the incident intensity was reflected with a π phase change. This is more than an order of magnitude greater than the specifications for the fibre connectors. However, it would be a worst-case approximation for a poorly aligned system. Also, a small absorption factor of 1% of the incident intensity is introduced to simulate fibre absorption and other losses within the storage loop. To overcome this reduction of signal intensity, gain is then provided at the appropriate level so that the system has an entire gain slightly less than unity. Some additional ASE needs then to be suppressed. Due to our backward pumping arrangement the travelling directions of the signal and pump beams are opposite, so that the isolators in the storage can block the ASE noise by 99 %. Using a random number generator noise is then introduced into the system in the form of amplified spontaneous emission and phase noise, which are estimated to be 0.2 dBμV/√Hz and 0.5 dBμV/√Hz for each pass.

The next step of the algorithm is to define the input signals, both the measurement and reference pulses. Results are plotted to illustrate the artificial Doppler bursts after mixing and the number of pulses created by the storage loop.

As the first simulated beat signal produced is produced, the noise can be adjusted to the same level as the measured noise of 12.5 dBμV/√Hz. The simulation can then run the code forward to producing more beat signals. The simulation for the first 16 pulses gave similar results to the experiment confirming the theoretical approach.

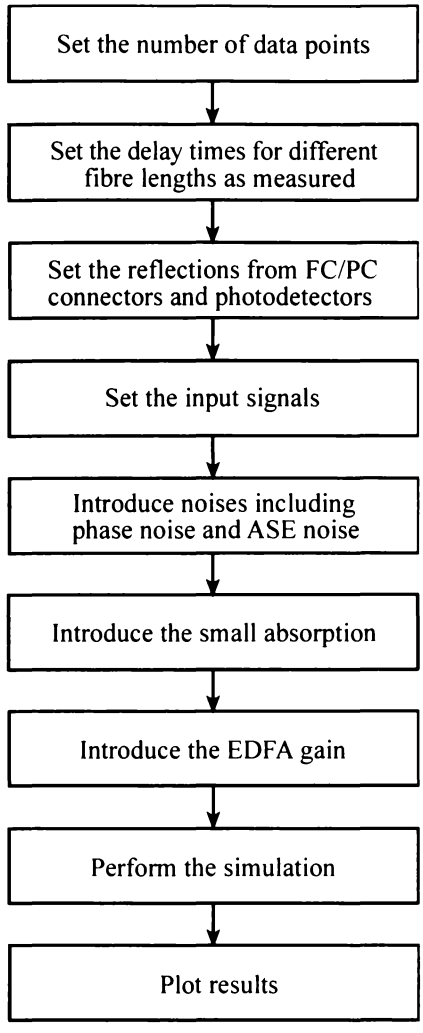

Figure 6. 34 - Flow diagram of the the storage loop experiment simulation.

Figure 6.35 shows the simulation beat signals for (a) the 2nd (b) the 51st (c) the 101st pulse. The beam delay fibre within the storage has successfully delayed the simulated measurement beam (Node 9) when compared to the amplified reference pulse train (Node 73). The measurement beam exhibits some small beat signals from reference pulses that have reflected off the detector or connectors at the output. This figure also proves that successful mixing between the delayed measurement and amplified reference pulse train has occurred and Node 15 shows the output. The difference between the two output signals (Nodes 15 and 79) is shown in the bottom graph, which illustrates the beat signal.

It is evident from Figure 6.35 (c) that the noise is getting bigger from pulse 70 onwards and a small oscillation begins. This situation will cause the reference pulse to be overridden by the noise. Comparing the simulation with the experiment, Figure

6.14, we find that the amplitude of the simulated beat signals is 1.0 dB larger than that obtained from the experiment. Some small, undesirable beat signals are introduced in the simulation due to mixing with reflections. This result can be explained by the fact that the optical fibre couplers do not have the exact theoretical split ratio, and the reflection percentage is not exactly that of the datasheets.

The maximum useful reference pulse number is conservatively estimated to be about 70, even though the 101st beat signal can be produced. The simulations show that the system can be applied over a measurement range of up to 2,550 m, significantly longer than the result of 583 m proven by the sixteen experimental reference pulses.

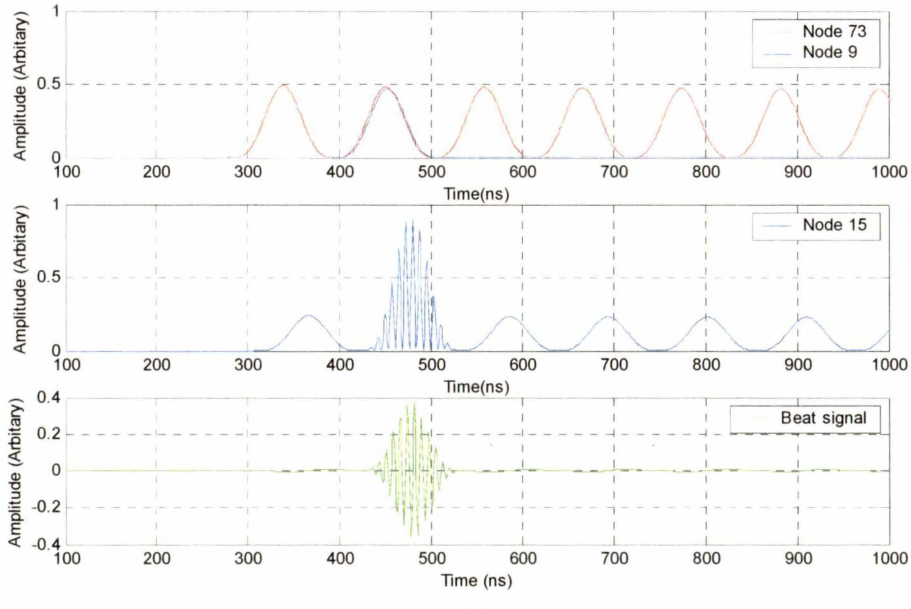

(a)

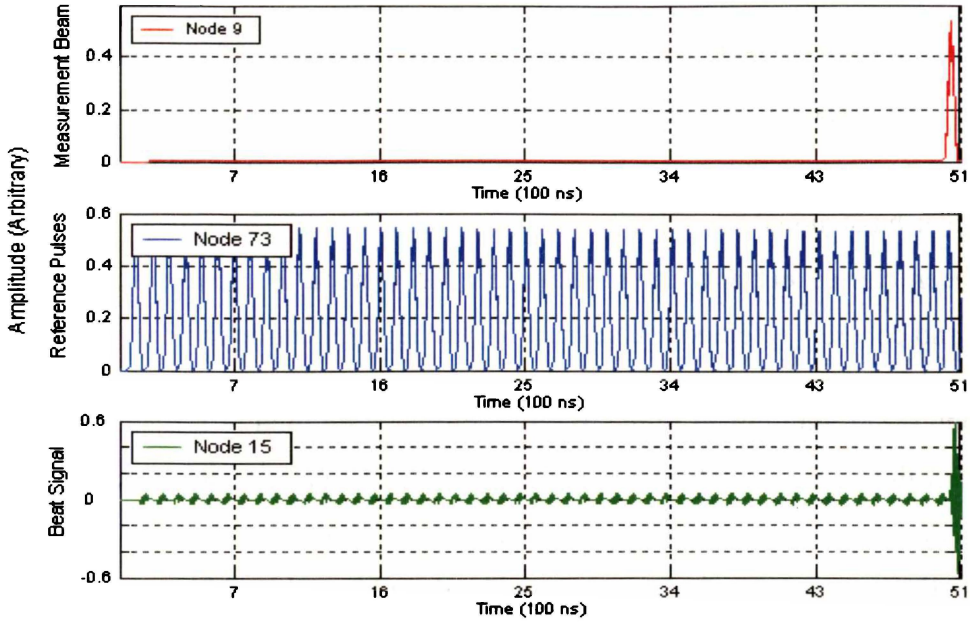

(b)

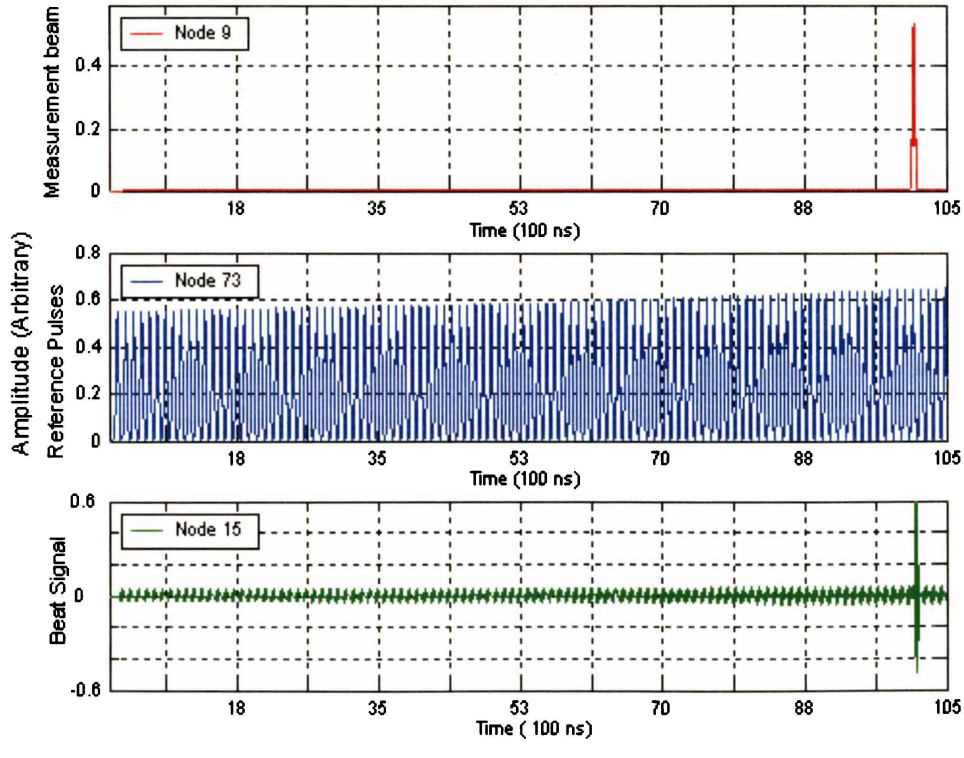

(c)

Figure 6. 35 - Simulated beat signals for (a) the second (b) the fifty first (c) the one hundred first.

6.8 Discussion

We have described and demonstrated a novel method for lidar reference beam storage that uses an erbium-doped fibre amplifier within the loop. The method produces a reference pulse train which mixes with the measurement beam generating a Doppler burst signal for velocity measurements. Several experiments and analyses have been carried out and demonstrate that the method is capable of generating a stable and coherent reference pulse train for further application in lidar systems.

Inserting the erbium-doped fibre amplifier into the amplified reference beam storage loop will introduce noise because of the generated amplified spontaneous emission. Noise figure measurements require accurate determination of the level of the amplified spontaneous emission generated by the erbium-doped fibre amplifier itself.

It is important to know the exact gain and loss of each of the optical components in the loop so that we can determine if the storage loop will go into laser oscillation. Therefore the storage loop is designed so that the total gain is slightly less than unity.

We have inserted a rotating mirror into the path of the measurement beam to simulate the effect in a velocimetry lidar system. We have also designed a phase locked loop demodulator circuit to reduce the noise of the measurement beam to 5.24 dBμV /$Hz^{1/2}$ at 400.029 MHz.

The system is accurate to 95.5 % over all sixteen pulses hence making amplified reference beam storage useful for wind shear and turbulence measurements. Generally all pulses show a ± 2 % velocity difference at 2 m/s improving to within ± 0.6 % at high speeds.

The data shows that the presented experimental set-up is suitable for Doppler velocimetry up to a range of 583 m. A simulation of the optical arrangement was performed in Matlab 6.0 software to investigate how many useful pulses could be achieved by this method. The simulations show that it should be possible to use the method up to a distance of 2,550 m.

6.8.1 Experimental limitations

There are several limiting factors in this experiment:

- The main limiting factor in the current set-up is the efficiency of the optical components. In particular, the loss in signal intensity through the acousto-optic modulator is in the order of 21 % for each shifted beam, and 60 % of the signal is lost at each single mode fibre coupler leaving only 8.4 % of the original 6.0 mW laser signal. Only 0.504 mW can be input into the amplified reference beam storage. Improving the efficiency of these components will greatly enhance the system. At present it takes quite some skill to take the optical set-up to the limit of its performance ability.

- The accuracy of the measured results drops from the sixteenth pulse, whose signal-to-noise ratio is somewhat lower than the first fifteen pulses. A main limitation is the experimental equipment available. A better means to determine fibre length and more accurate time measurement would improve the experimental results. The simulation has proven that the number of pulses can be extended to more than 70. Improving the equipment, in particular using more precise measurement equipment might extend the practical number of pulses beyond that reached by simulation. This would make the amplified storage loop a very attractive proposition for a low cost lidar system.

- The amplified reference beam storage used pulse lengths of approximately 100 ns, which provided Doppler bursts of equivalent times. Compared to other lidar systems, these very short pulses provide a high spatial measurement resolution of 37 m and a measurement volume length of less than 30 m. The short Doppler bursts however make it difficult to transform the frequency into a velocity due to the weak signal that is produced by mixing the reference beam pulse train and a faint Doppler shifted measurement beam.

6.8.2 Theoretical limitations

The fibre attenuation and dispersion are two major limitations in the amplified reference beam storage. The main theoretical limitation is the fibre dispersion, which determines the ability to distinguish the individual output pulses, and tends to be the limiting factor for use. Dispersion is an effect, which causes broadening of pulses in an optic fibre cable, because the material of the fibre has different refractive indices at different wavelengths. As the laser is not monochromatic, the input pulse includes a spread of frequencies centred on the laser's wavelength. Each frequency component experiences a different refractive index in the fibre and therefore travels at a different velocity causing the output pulse at the output of the fibre to be spread in time.

The broadened pulse width, τ, of a Gaussian pulse after travelling a specified distance, d, in a fibre can be calculated as (Saleh and Teich, 1991)

$$\tau(d) = \tau_0 \left[1 + \left(\frac{d}{d_0} \right)^2 \right]^{1/2} \qquad 6\text{-}13$$

The Gaussian pulse is spreading as a function of distance. At large distances, the width increases at the rate $|D_v| / \pi \tau_0$, which is inversely proportional to the initial width τ_0. D_v is the material dispersion coefficient for the centre wavelength.

The dispersion coefficient of a typical optical fibre at a wavelength of 1550 nm is approximately 17 $ps.km^{-1}.nm^{-1}$. Considering our pulse length and the line width of about 2 nm of the laser leads to a maximum storage length in of about 88 km. This is a considerably longer distance than that achieved experimentally (583 m) or even in the simulations (2,550 m). Unless the measurement range is much increased pulse spreading will not have a significant effect.

In practice, other effects such as attenuation would limit the range, but in contrast to dispersion there is no practical limit to the amplified reference pulse storage.

Chapter 7

Conclusion

The concept of using a reference beam storage loop for low coherence lidar systems, which has previously been reported in the literature, has a number of limitations that make it unpractical for use in commercial systems. The main problems are the number of pulses that can be used for Doppler velocimetry, the high noise, and the low signal to noise ratio.

A novel design for amplification of the reference beam pulse inside the loop has been presented in this thesis. The technique compensates for the decay of the reference beam signal and thereby increases the number of pulses that can be used for Doppler measurements. The new approach relies primarily on the use of an erbium-doped fibre amplifier, which provides a gain slightly less than one to avoid laser oscillation. The system has the ability of measuring the velocity of moving targets in the direction of measurement beam propagation.

The optical design and the components necessary to generate the required gain have been presented and characterised. Electronic as well as software-based methods to improve the signal to noise ratio of the final signal have been included in the design. The experimental results prove that the stored amplified reference beam pulses optically mix with a Doppler shifted measurement beam. Velocity measurements of a hard target have been carried out and show that the system is accurate in measuring Doppler shifts. Software simulations were performed which show that it should be possible to use the system over a much larger range than the experimental results proved. Both simulation and the amplified reference beam storage loop demonstrate that the system might be effectively applied to measuring wind shear and turbulence.

This thesis has significantly advanced the concept of reference beam storage for low coherence lidar in several areas, specifically:

- The operating wavelength has been transferred to the telecommunication range around 1.55μm. This leads to a measurement system that is more eye-safe than the previous storage loop design and allows the use of readily available optical components.
- An all-fibre-pigtailed, amplified reference beam storage has been designed.
- The pulse train output from the storage loop does not decay as in previous systems, as it is amplified while passing through an erbium-doped fibre amplifier. This increases the number of reference beam pulses that are useful for velocimetry measurement.
- The noise of the Doppler signal has been reduced by electronic (synchronous detection and phase-lock loop) and software techniques (wavelet transform).
- Optical mixing between 16 amplified, stored reference pulses and a Doppler shifted measurement was successful at a signal to noise ratio 30 dB. This is equivalent to a maximum measurement distance of 583 m. Simulations show that it should be possible to extent the measurements to 70 pulses (15 dB signal to noise ratio) which corresponds to a range of 2,550 m.
- The Doppler measured velocities agree with reference measurements to within ±0.14 m/s over the range 1 to 10 m/s.

This study has advanced the storage loop concept further towards a practical lidar system. However, there are still several problems that need to be solved before this approach will lead to a commercially viable design. This work has not investigated how the backscattered light can be efficiently mixed with the reference beam. Coupling the measured signal into single mode fibres will be very inefficient and will increase the noise. Overall, it would be desirable to further improve the signal to noise ratio of the current design, so that the system will be able to cope with very weak backscattered signals.

These are difficulties that can be overcome with further work, and a low coherence, long range, pulsed Doppler system based on a compact storage loop design remains a feasible alternative to current commercial systems.

Appendix I - Time sliced FFT processing

The following signal processing code was written and executed using MATLAB 6.0 software. This program reads data files from the oscilloscope, then performs Wavelet de-noising, Blackman.m to break the de-noised data into 17 time slots, and FFT, to convert the time sliced data to frequency domain. Finally plots 3-D graphs of the time sliced FFT data by performing Statistica 6.0.

% Time sliced FFT processing
% Jyi-Lai Shen
% July 2002

```
%Time Sliced FFT Code
% Clear all variables
clear;

% Find number of points in each block
N = ceil (1000/17);

% Find total blocks
blocks = ceil (1000/N);

% Load data files
infile = fopen('E:\files\TEK00001.csv');
a1 = fscanf(infile,'%f',[N, blocks]);
fclose (infile);
infile = fopen('E:\files\TEK00003.csv');
a2 = fscanf(infile,'%f', [N, blocks]);
fclose (infile);
infile = fopen('E:\files\TEK00016.csv');
a3 = fscanf(infile,'%f', [N, blocks]);
fclose (infile);

% Perform the wavelet processing of a1
[CA1,CD1]=dwt(a1,'db2');
[CA2,CD2]=dwt(CA1,'db2');
[CA3,CD3]=dwt(CA2,'db2');
[CA4,CD4]=dwt(CA3,'db2');

% Perform the wavelet processing of a2
[CA5,CD12]=dwt(a2,'db2');
[CA6,CD22]=dwt(CA5,'db2');
[CA7,CD32]=dwt(CA6,'db2');
[CA8,CD42]=dwt(CA7,'db2');

% Perform the wavelet processing of a3
[CA9,CD13]=dwt(a3,'db2');
[CA10,CD23]=dwt(CA9,'db2');
```

```
[CA11,CD33]=dwt(CA10,'db2');
[CA12,CD43]=dwt(CA11,'db2');
%Setup Blackman matrix
Id(1,1:blocks)=1;
Blk2=blackman(N)*Id;

% Define number of points in FFT
M = 1000;

%process pulse1 file
a = CA4(1,1).*Blk2;
b = fft(a, M);
c = abs(b);

%write results to data file
outfile = fopen ('files/Timesliced_FFT1.csv', 'W');
for f = 1:M/2;
fprintf (outfile,'%f', 1000000/M*f);
fprintf (outfile,'%f', c(f,1:blocks-1));
fprintf (outfile,'%f\n', c(f,blocks));
end
fclose (outfile);
%process pulse3 file
a = CA8(1,1).*Blk2;
b = fft(a, M);
c = abs(b);
%write results to data file
outfile = fopen ('files/Timesliced_FFT3.csv', 'w');
for f = 1:M/2;
fprintf (outfile,'%f', 1000000/M*f);
fprintf (outfile,'%f', c(f,1:blocks-1));
fprintf (outfile,'%f\n', c(f,blocks));
end
fclose (outfile);

%process pulse16 file
a = CA12(1,1).*Blk2;
b = fft(a, M);
c = abs(b);

%write results to data file
outfile = fopen ('files/Timesliced_FFT16.csv', 'w');
for f = 1:M/2;
fprintf (outfile,'%f', 1000000/M*f);
fprintf (outfile,'%f', c(f,1:blocks-1));
fprintf (outfile,'%f\n', c(f,blocks));
end
fclose (outfile);
```

Appendix II - Signal processing codes

The following signal processing code is written using MATLAB 6.0 software. Code-1 is used to de-noise the signal from the output of the phase-locked loop demodulator. It reads burst data from the oscilloscope and performs a wavelet transformation on this data. Code-2 is used to convert the frequency maximum fmx into velocity, add noise, and to determine the regressing coefficient.

% Signal Processing Wavelet de-noises Code-1
% Jyi-Lai Shen
% June 2002

```
% Clear all variables
clear;

% Define input signals and noise
sn=sin(20.*linspace(0,pi,1000))+0.5.*rand(1,1000);

% Perform the wavelet processing
[CA1,CD1]=dwt(sn,'db2'); %Signal and noise at Level 1
[CA2,CD2]=dwt(CA1,'db2');%Signal and noise at Level 2
[CA3,CD3]=dwt(CA2,'db2');%Signal and noise at Level 3
[CA4,CD4]=dwt(CA3,'db2');%Signal and noise at Level 4

%Show graphs
figure(1)
subplot(711)
plot(1:length(sn), sn)
subplot(712)
plot(1:length(CD1), CD1)
subplot(713)
plot(1:length(CA1), CA1)
subplot(714)
plot(1:length(CD2), CD2)
subplot(715)
plot(1:length(CA2), CA2)
subplot(716)
plot(1:length(CD3), CD3)
subplot(717)
plot(1:length(CA3), CA3)
shg;
```

```
% Signal Processing Code-2
% Jyi-Lai Shen
% June 2002

clear;clg;
   m = 1;

%  Find number of points in each blocs
N = ceil(500/1);

%  Find total blocks
Blocks = ceil(501/N);

%  Read burst data from oscilloscope
infile1 = fopen('burstNoise01.txt');
a1 = fscanf(infile1,'%f',[N, Blocks]);
fclose(infile1);

% Define the range for noise
   for n = 0:0.05:1.4;
     k = 1;
     for f = 0.1:0.02:0.9;

% Define the number of data points
       N =32;
       for t = 1:N;

% Initiate the noise
         xn(t) = rand* 2 - 1;

%Define the white noise
         xn(t) = (log(1-abs(xn(t)))/1.49*sign(xn(t)))*n;

% Define input signals
         x1(t) = sin(pi* (t/N));          x2(t) = cos(2* pi* (f*
       N/2)* (t/N));
         x3(t) = cos(2* pi* (f/2* N/2)* (t/N));
       end

% Add white noise to burst signals
    B1 = x2.* x1.^2;B1n = B1 + xn;
       B2 = x3.* x1.^2;B2n = B2 + xn;B2pn = B2 + xn;
       B2mn = B2-xn;DB2n = B2pn + B2mn;
       B1np2n = B1n + B2n;B1nm2n = B1n - B2n;
       DBB1n = B1np2n + B1nm2n;  AN2B = xn + a1;
   % Perform the signal processing
       N1 = 4096;
       yDBB1n = fft(DBB1n, N1);
       aDBB1n = abs(yDBB1n(1:N1/2));[mDBB1n indexDBB1n] =
       max(aDBB1n);
```

```
        fmxDBB1n = (indexDBB1n -1)/(N1/2);
        yAN2B = fft(AN2B, N1);
        aAN2B = abs(yAN2B(1:N1/2));[mAN2B indexAN2B] = max(aAN2B);
        fmxAN2B = (indexAN2B -1)/(N1/2);

% Report progress
        figure (1);
        subplot (211);
        plot(f,fmxB1n,'b*',f,f,'ro');hold on;grid on;
        subplot(212);
        plot(f,fmxAN2B,'b*',f,f,'ro');hold on;grid on;
        title('Trend of Burst AN2B with Noise 0:0.05:1.4');
        xlabel('I/P Frequency');ylabel('O/P Frequency ');
        P(k) = f;
        F(k) = fmxDBB1n;
        K = k+1;
        X = P';
        Y = F';
      end

% Convert frequency maximum fmx into velocity
    Δf = fmxAN2B - 400.072;
    υ 2 =  Δf * 1.55;

% Compare  υ 1 and  υ 2
    Δυ = υ 1 -  υ 2;

% Perform Regressing
   X1 = [ones(41,1),X];
      [r1,r2,r3,r4,r5] = regress(Y,X1);
      R(m) = r5(1,1);
      figure (2);
      plot(n,R(m),'b*');hold on;grid on;
      title('Trend of Burst DBB1n with Noise 0:0.05:1.4');
      xlabel('White Noise');ylabel('Correlation (R^2) ');
      m = m + 1;
    end
    shg
```

Appendix III - Amplified reference beam storage loop simulation code

The Amplified reference beam storage loop simulation was performed in MATLAB 6.0, using the following code.

```
% Simulation of amplified reference beam storage loop experiment
% Jyi-Lai Shen
% June 2002
  % Define the number of data points per nanosecond
  dppns = 10;
  %Define the delays in time between nodes
  m=50;
  td1 =157.3*m*dppns;%BDF1%
  td2 =5.2*dppns;%Input of OC2%
  td3 =0.3*dppns;%OC2%
  td4 =5.2*dppns;%Output of OC2%
  td5 =17.0*dppns;%OI1%
  td6 =5.2*dppns;%Input of OC1%
  td7 =0.3*dppns;%OC1%
  td8 =5.2*dppns;%Output of OC1%
  td9 =1.6*dppns;%BDF2%
  td10=21.7*dppns;%PC1%
  td11=17.0*dppns;%OI2%
  td12=24.0*dppns;%EDFA%
  td13=17.0*dppns;%OI3%
  td14=10.8*dppns;%TF%
  td15=21.7*dppns;%PC2%
  td16=16.8*dppns;%OI4%
  td17=5.2*dppns;%Input of OC1%
  td18=0.3*dppns;%OC1%
  td19=5.2*dppns;%Output of OC1%
  td20=5.2*dppns;%Input of OC2%
  td21=0.3*dppns;%OC2%
  td22=5.2*dppns;%Output of OC2%
  %Define the reflections from the connectors
  InputReflect = 0.2;%Input reflection from single mode fibre
        coupler%
  OutputReflect = 0.2;%Output reflection from photodetectors%
  Reflect = 0.01;%Reflection from FC connectors%
  Absorption = 0.01;
  Propagate = 0.98;%Transmission in propagating direction%
  %Define the amplifier gain and absorption within the storage loop
  EDFAGain = 31.6;
  %Define the input signals for the storage loop
  MeasInput(1:500*dppns) = 0;
  RefInput(1:500*dppns) = 0;
  a = 100*dppns:160*dppns;
  MeasInput(a) = sin((a-(100*dppns))/(60*dppns) *
        pi).^2.*exp(i*2*pi*12.5*(a-(100*dppns))/dppns);
  RefInput(a) = sin((a-(100*dppns))/(60*dppns) *
        pi).^2.*exp(i*2*pi*12.76*(a-(100*dppns))/dppns);
```

```
%Define phase and ASE noises
for n=0:0.05:1.4;
N=32;
for t=1:N;
xn(t)=rand*2 - 1;
PhaseNoise(t)=(log(1-abs(xn(t)))/1.49*sin(xn(t))) * n;
end
PhaseNoise(1:3500*dppns) = 0;
ASENoise(1:3500*dppns) = 0;
ASENoise(a)= sin((a-(100*dppns))/(60*dppns) *
       pi).^2.*exp(i*2*pi*25.0*(a-(100*dppns))/dppns);
%Define starting period of no signals
P(1:500*dppns,1:81) = 0;
% Perform the simulation
for t = 100*dppns+1:500*dppns
    P(t,1) = MeasInput(t)+P(t-4,2)*InputReflect + PhaseNoise(t);
    P(t,2) = P(t,4)*Propagate+P(t-4,1)*Reflect;
    P(t,3) = P(t,1)*Propagate+P(t-4,4)*Reflect;
    P(t,4) = P(t-td1,6);
    P(t,5) = P(t-td1,3);
    P(t,6) = P(t,8)*Propagate+P(t-4,5)*Reflect;
    P(t,7) = P(t,5)*Propagate+P(t-4,8)*Reflect;
    P(t,8) = P(t-td2,10);
    P(t,9) = P(t-td2,7);
    P(t,10)= P(t-td3,12)*0.707+P(t-td3,76)*0.707;
    P(t,11)= P(t-td3,9)*0.707+P(t-td3,73)*0.707;
    P(t,12)= P(t-td4,14);
    P(t,13)= P(t-td4,11);
    P(t,14)= P(t,16)*Propagate+P(t-4,13)*Reflect;
    P(t,15)= P(t,13)*Propagate+P(t-4,16)*Reflect;
    P(t,16)= P(t-4,15)*OutputReflect;
    P(t,17)= RefInput(t)+P(t-4,18)*InputReflect + PhaseNoise(t);
    P(t,18)= P(t,20)*Propagate+P(t-4,17)*Reflect;
    P(t,19)= P(t,17)*Propagate+P(t-4,20)*Reflect;
    P(t,20)= P(t-td5,22);
    P(t,21)= P(t-td5,19);
    P(t,22)= P(t,24)*Propagate+P(t-4,21)*Reflect;
    P(t,23)= P(t,21)*Propagate+P(t-4,24)*Reflect;
    P(t,24)= P(t-td6,26);
    P(t,25)= P(t-td6,23);
    P(t,26)= P(t-td7,68)*0.707+P(t-td7,28)*0.707;
    P(t,27)= P(t-td7,65)*0.707+P(t-td7,25)*0.707;
    P(t,28)= P(t-td8,30);
    P(t,29)= P(t-td8,27) *1.469 + ASENoise(t);
    P(t,30)= P(t,32)*Propagate+P(t-4,29)*Reflect;
    P(t,31)= P(t,29)*Propagate+P(t-4,32)*Reflect;
    P(t,32)= P(t-td9,34);
    P(t,33)= P(t-td9,31);
    P(t,34)= P(t,36)*Propagate+P(t-4,33)*Reflect;
    P(t,35)= P(t,33)*Propagate+P(t-4,36)*Reflect;
    P(t,36)= P(t-td10,38);
    P(t,37)= P(t-td10,35);
    P(t,38)= P(t,40)*Propagate+P(t-4,39)*Reflect;
    P(t,39)= P(t,37)*Propagate+P(t-4,40)*Reflect;
    P(t,40)= P(t-td11,42);
    P(t,41)= P(t-td11,39);
    P(t,42)= P(t,44)*Propagate+P(t-4,41)*Reflect;
    P(t,43)= P(t,41)*Propagate+P(t-4,44)*Reflect;
    P(t,44)= P(t-td12,46)*1.5;
```

```
    P(t,45)= P(t-td12,43)*1.5;
    P(t,46)= P(t,48)*Propagate+P(t-4,45)*Reflect;
    P(t,47)= P(t,45)*Propagate+P(t-4,48)*Reflect;
    P(t,48)= P(t-td13,50);
    P(t,49)= P(t-td13,47);
    P(t,50)= P(t,52)*Propagate+P(t-4,49)*Reflect;
    P(t,51)= P(t,49)*Propagate+P(t-4,52)*Reflect;
    P(t,52)= P(t-td14,54);
    P(t,53)= P(t-td14,51);
    P(t,54)= P(t,56)*Propagate+P(t-4,53)*Reflect;
    P(t,55)= P(t,53)*Propagate+P(t-4,56)*Reflect;
    P(t,56)= P(t-td15,58);
    P(t,57)= P(t-td15,55);
    P(t,58)= P(t,60)*Propagate+P(t-4,57)*Reflect;
    P(t,59)= P(t,57)*Propagate+P(t-4,60)*Reflect;
    P(t,60)= P(t-td16,62);
    P(t,61)= P(t-td16,59);
    P(t,62)= P(t,64)*Propagate+P(t-4,61)*Reflect;
    P(t,63)= P(t,61)*Propagate+P(t-4,64)*Reflect;
    P(t,64)= P(t-td17,66);
    P(t,65)= P(t-td17,63);
    P(t,66)= P(t-td18,28)*0.707+P(t-td18,68)*0.707;
    P(t,67)= P(t-td18,25)*0.707+p(t-td18,65)*0.707;
    P(t,68)= P(t-td19,70);
    P(t,69)= P(t-td19,67);
    P(t,70)= P(t,72)*Propagate+P(t-4,69)*Reflect;
    P(t,71)= P(t,69)*Propagate+P(t-4,70)*Reflect;
    P(t,72)= P(t-td20,74);
    P(t,73)= P(t-td20,71);
    P(t,74)= P(t-td21,76)*0.707+P(t-td21,12)*0.707;
    P(t,75)= P(t-td21,73)*0.707+p(t-td21,9)*0.707;
    P(t,76)= P(t-td22,78);
    P(t,77)= P(t-td22,75);
    P(t,78)= P(t,80)*Propagate+P(t-4,77)*Reflect;
    P(t,79)= P(t,77)*Propagate+P(t-4,80)*Reflect;
    P(t,80)= P(t-4,79)*OutputReflect;
end
 %progress
    if mod(t,100)==0
        fprintf('%d / %d\n',t,500*dppns);
    end
end
% Write data files for each node
for f=1:81
  filename = sprintf('.\\ARBSsimulation\\ressqr%02d.csv', f);
  P(:,f) = abs(P(:,f)) .^ 2;
  outfile = fopen (filename, 'w');
  fprintf(outfile,'%f\n', P(:,f));
  fclose(outfile);
end;
t=size(P(:,1));
time=[t(2):t(1)];
beat = P(:,17)-P(:,19);
figure(1);
subplot(311)
plot(time,P(:,41),'r-', time,P(:,37),'b-');
legend('Node 73', 'Node 9')
grid on;
axis([100 3200 0 1])
xlabel('Time(ns)');ylabel('Amplitude (Arbitary)');
subplot(312)
```

```
plot(time,P(:,17),'b-');
legend('Node 15')
axis([100 3200 0 1])
grid on;
xlabel('Time(ns)');ylabel('Amplitude (Arbitary)');
subplot(313)
plot(time,beat,'g-');
legend('Beat signal')
grid on;
xlabel('Time (ns)');ylabel('Amplitude (Arbitary)');
set(gca,'ytick',[-0.6:0.2:0.6]);
axis([100 3200 -0.6 0.6])
shg
```

Appendix IV - Pulse circuit

The pulse circuit used in the amplified reference beam storage loop experiment was designed using ORCAD 9.0. The circuit schematic is illustrated below and the PCB is shown on the following page with both a photograph and PCB layout (bottom side).

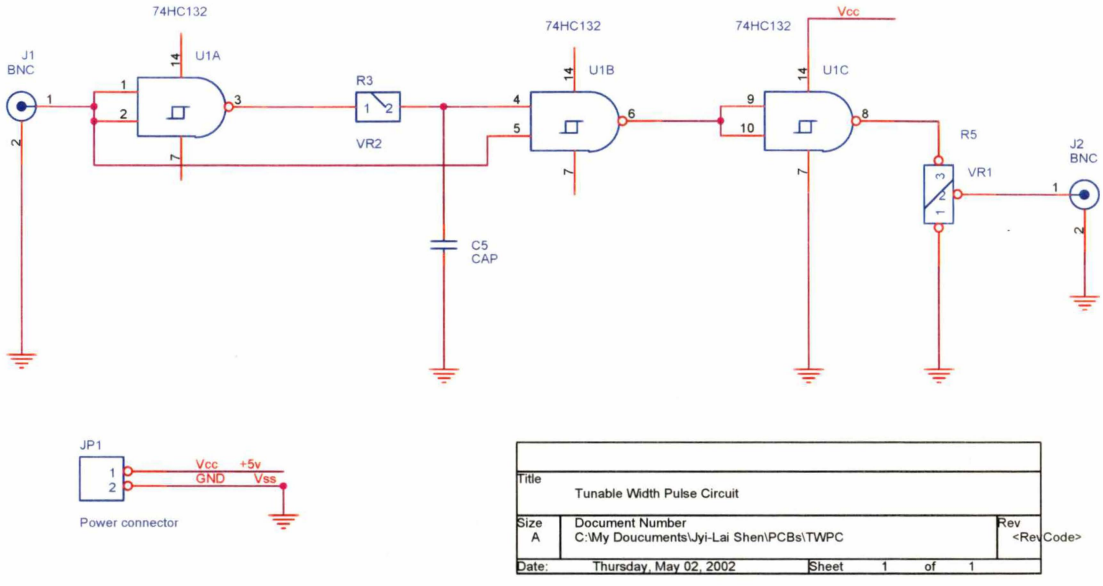

Figure 7. 1 - The schematic diagram of pulse circuit.

The schematic diagram uses a series of Schmitt trigger high-speed CMOS NAND gates (74HC132, Farnell, New Zealand) to adjust the duty cycle of the pulse. The circuit has a time constant determined by the product of the variable resistor R_3 and capacitor C_5 that allows setting the pulse width between 10 ns and 100 ns.

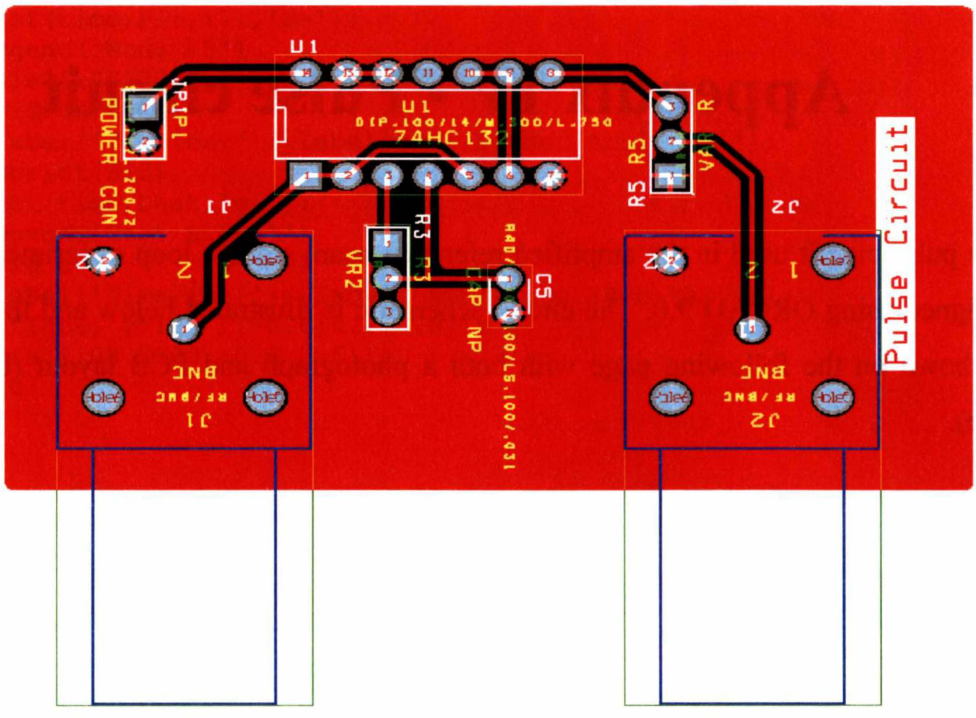

(a)

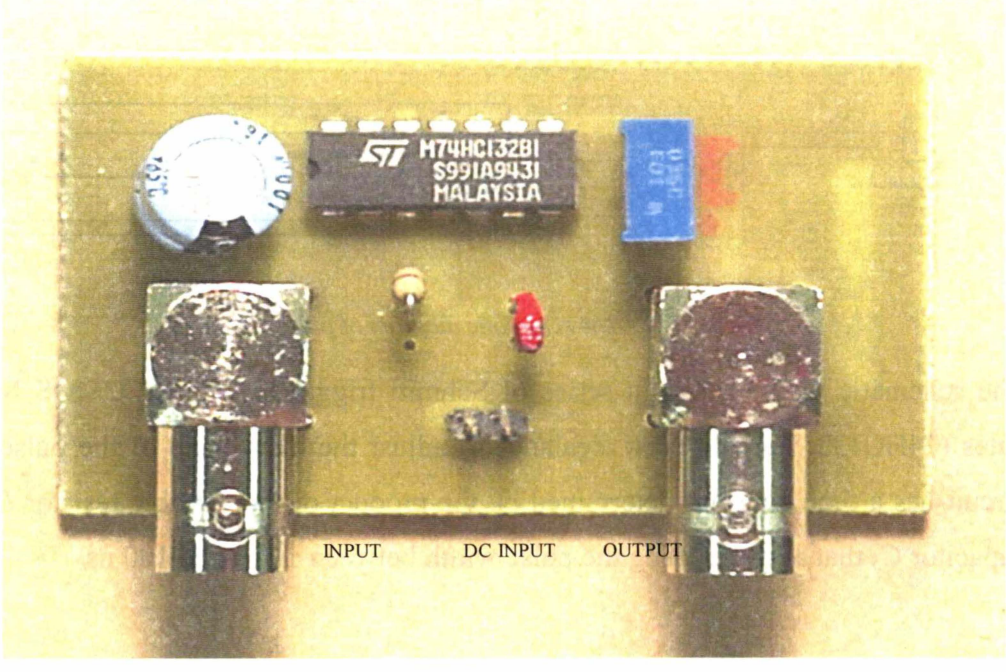

(b)

Figure 7. 2 - (a) Bottom side of pulse circuit PCB and (b) the photograph.

Appendix V - RF amplifier circuit

The RF amplifier circuit used in the amplified reference beam storage loop experiment was designed using ORCAD 9.0. The circuit schematic and the PCB are illustrated below. The PCB is shown with both top and bottom sides of the board.

The first two stages of the RF amplifier use the CLC425 operational amplifiers from National Semiconductor. This integrated circuit combines wide bandwidth (1.9 GHz GBW) with very low input noise (1.05 nV/√Hz, 1.6 pA/√Hz), low DC errors (100 μV VOS, 2 μV/°C drift) and provides a precise, wide dynamic-range at gains of ≥10. The first stage is a transimpedance amplifier, where the gain and output voltage, V_0, is determined by the feedback resistor, R_f:

$$V_o = I_{sc} \times R_f \qquad 7\text{-}1$$

where R_f is 10 kΩ, and the photocurrent, I_{sc}, typically only several μA. The second stage is a voltage amplifier with a gain of 15 dB. The final two stages consist of a differential amplifier and a voltage follower and use the AD8001 (Analog Devices). This is a low power, high-speed amplifier designed to operate off a 5 VDC supply consuming only 50 mW of power. It is a current feedback amplifier and features gain flatness of 0.1 dB to 100 MHz while offering differential gain and phase error of 0.01 %.

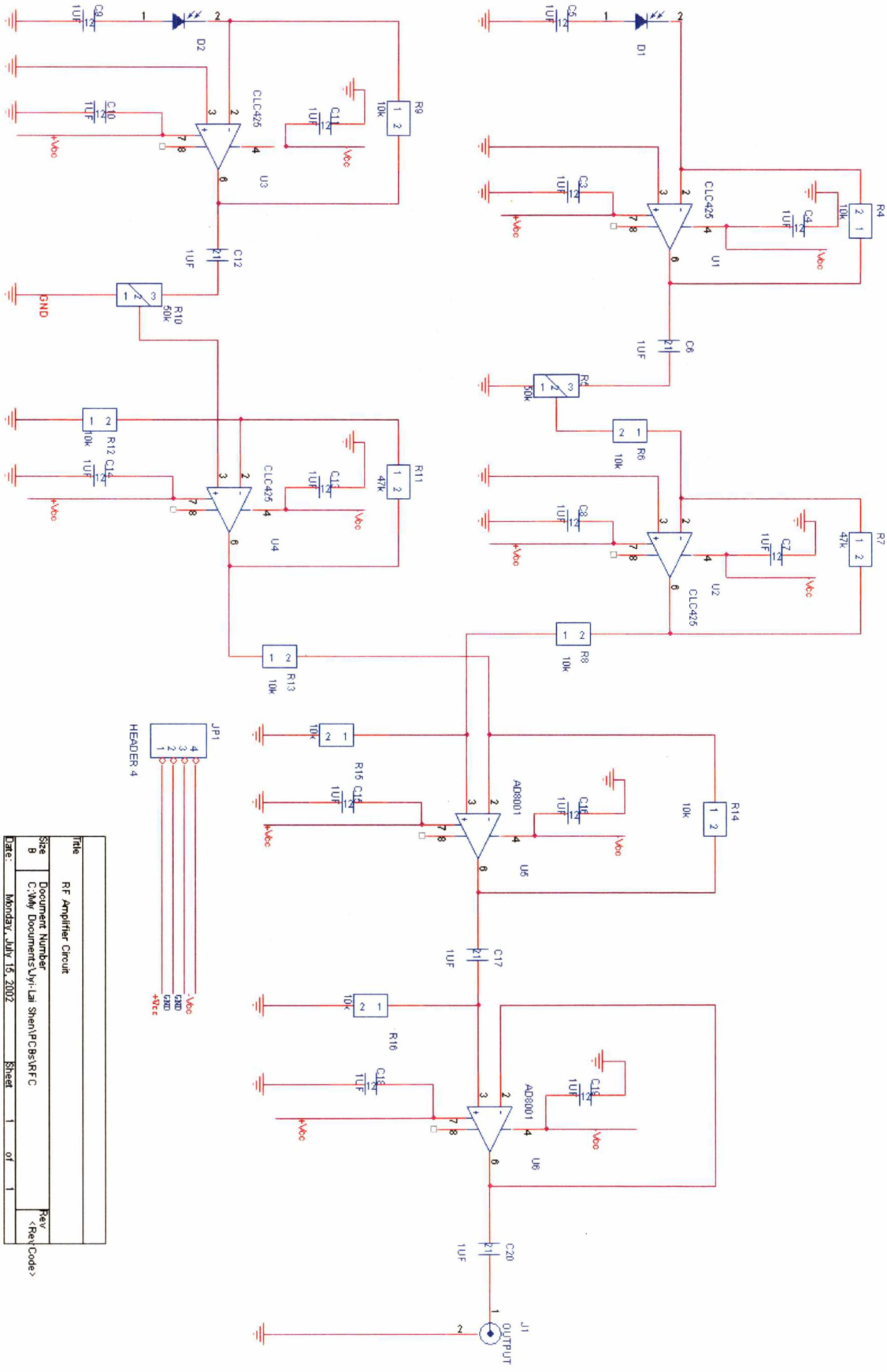

Figure 7. 3 - The schematic diagram of RF amplifier circuit.

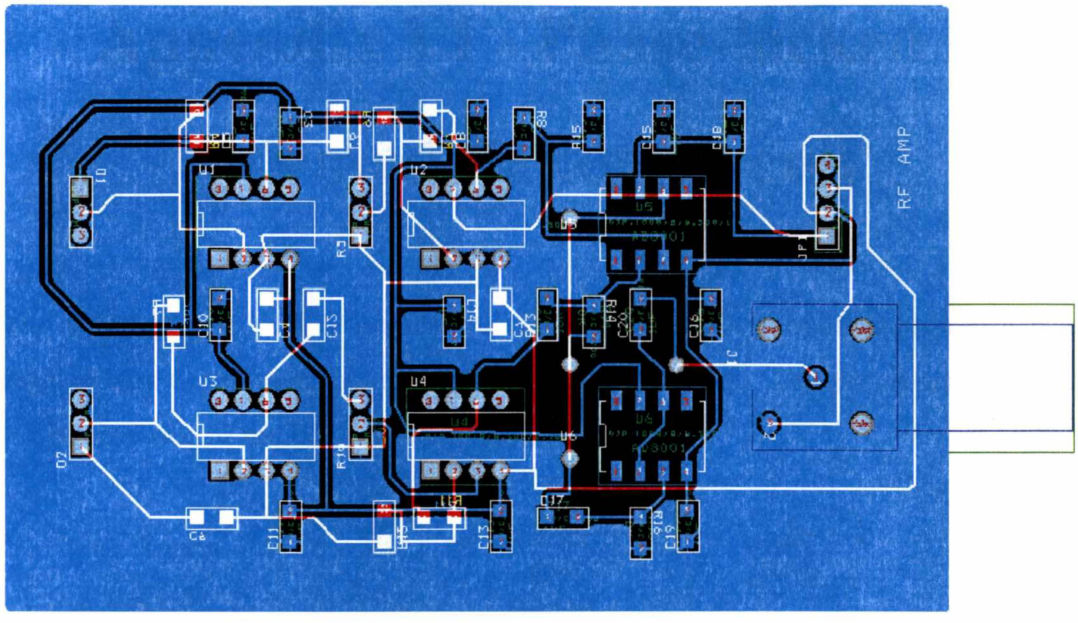

(a)

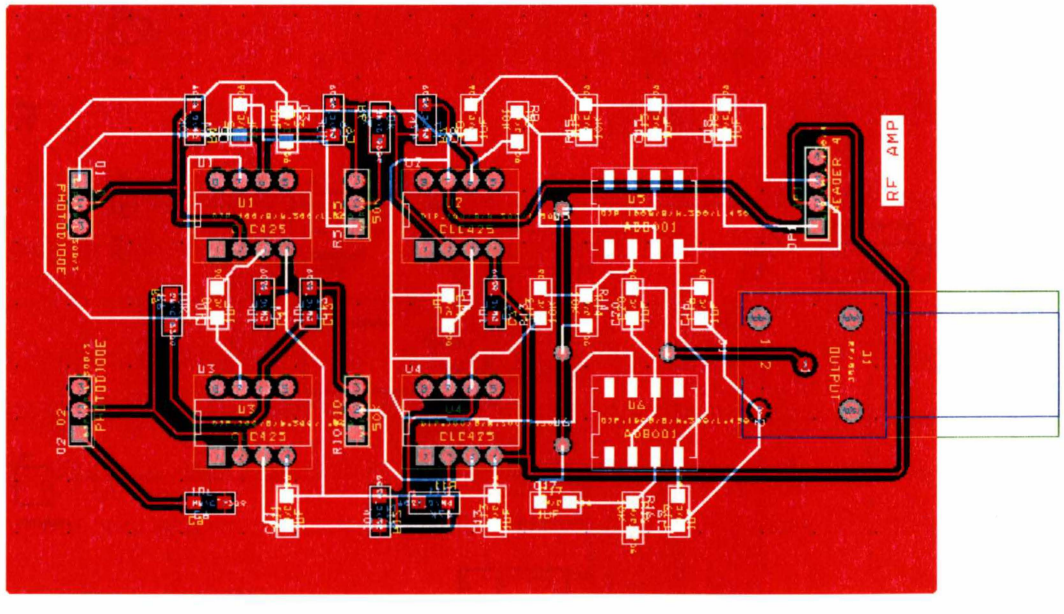

(b)

Figure 7. 4 - (a) Top side and (b) bottom side of RF amplifier PCB.

Appendix VI - Phase-locked loop demodulation circuit

The phase-locked loop demodulation circuit used in the amplified reference beam storage loop experiment was designed using ORCAD 9.0. The circuit schematic and the bottom side of the PCB are illustrated below.

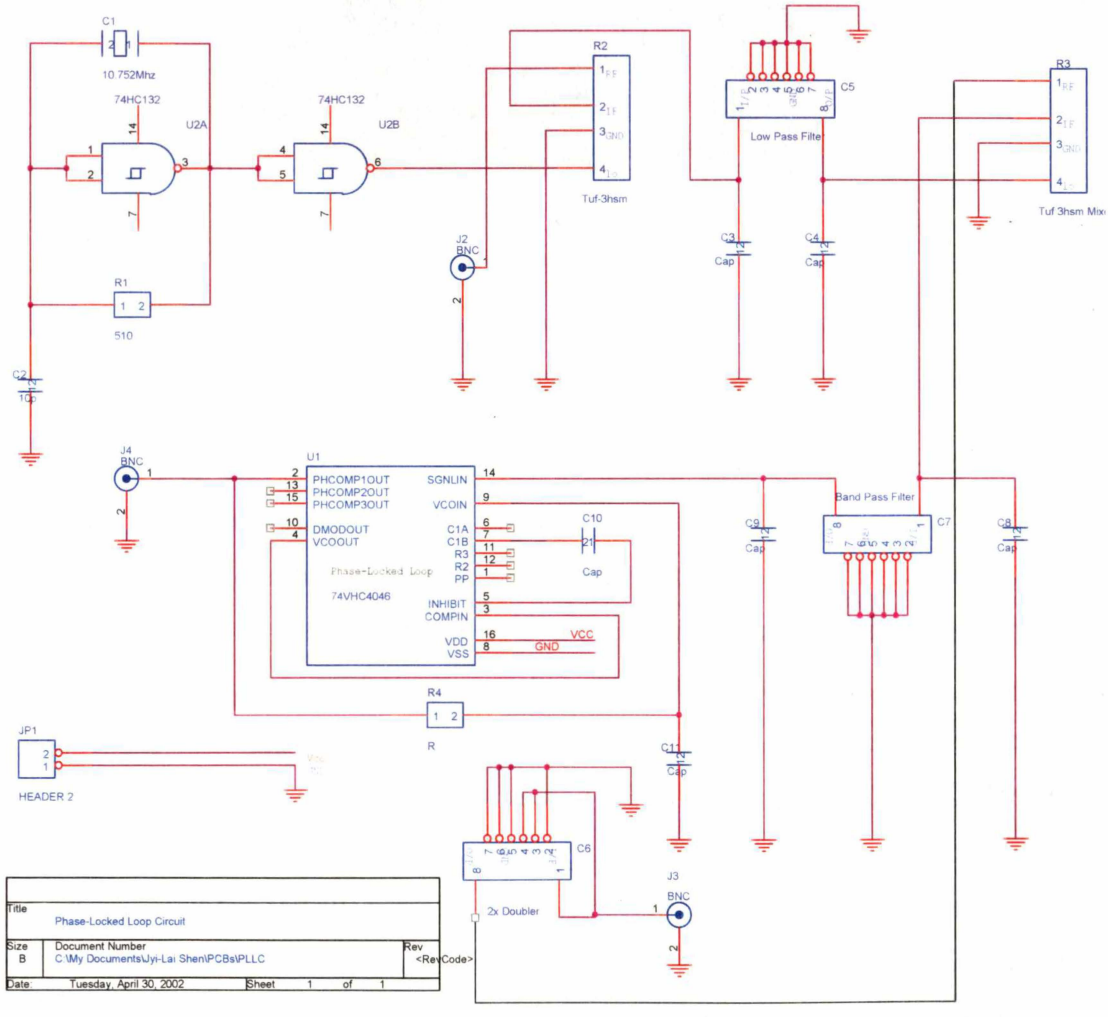

Figure 7. 5 - The schematic diagram of phase-locked loop demodulation circuit.

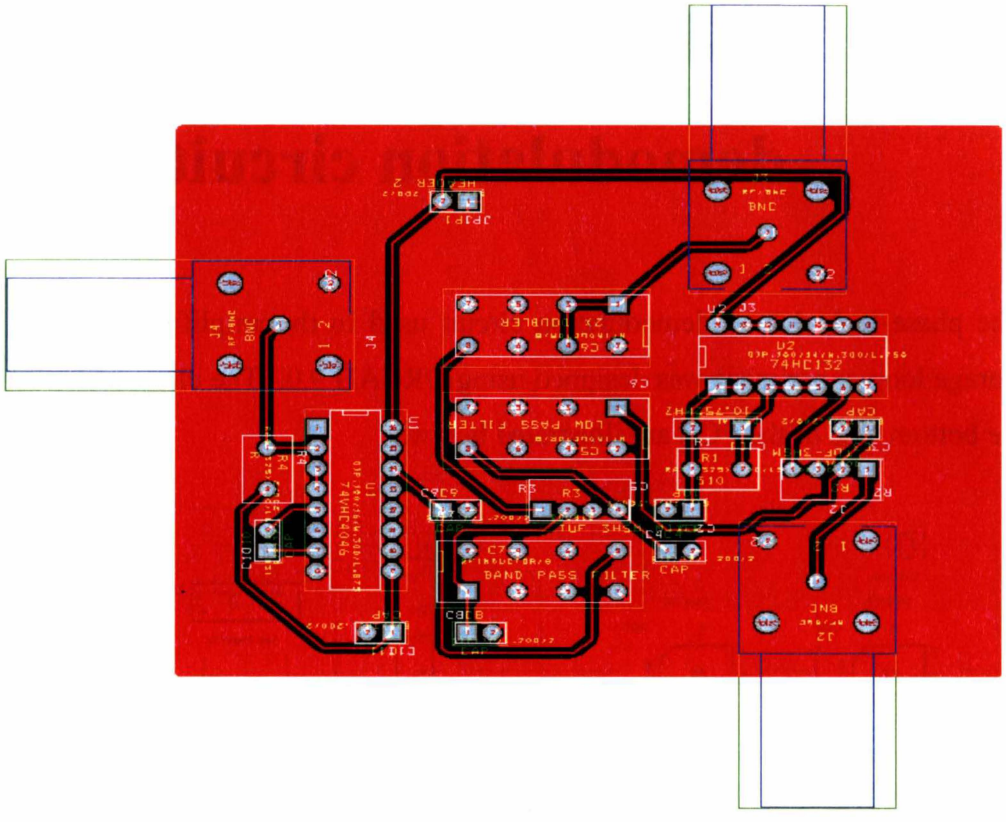

Figure 7. 6 - Bottom Side of phase-locked loop demodulation PCB.

Here is the schematic of a phase-locked loop used for noise reduction. There are two mixers (Tuf-3hsm, Mini-circuits, New York, USA) that are used in this system to merge two signals. These mixers provide a frequency range of between 0.15 and 400 MHz with a Mid-band conversion loss of 5.0 dB. Mixer 1 is used to combine the Doppler shifted measurement light and a very stable and precise 10.752 MHz frequency provided by the crystal oscillator (112434, Farnell, New Zealand). The two CMOS NAND gates (74HC132, Farnell, New Zealand) are used as converters.

This combined signal is directed into a low-pass filter (PLP450, Mini-curcuits, New York, USA). The output from low pass filter is then mixed with the 400 MHz input signal provided by the frequency doubler (RK-2, Farnell, New Zealand) and passed to the bandpass filter (PBP-10.7, Mini-curcuits, New York, USA). The signal then enters the phase locked loop (74VHC4046N, Farnell, New Zealand) and is then the output.

Appendix VII – Coherence length determination

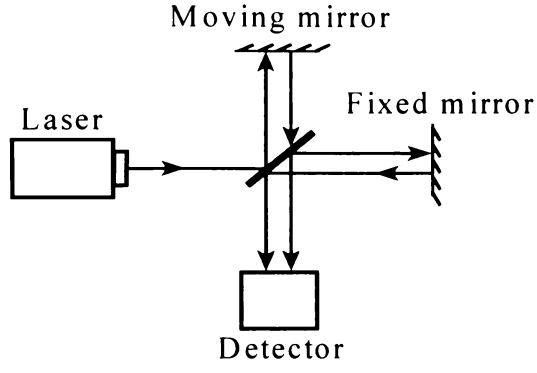

Figure 7. 7 - Block diagram of Michelson interferometer.

The coherence length was measured using the set-up shown in Figure 7.7. Interference fringes were recorded, and the fringe visibility was determined.

The intensity on the detector is (Saleh and Teich, 1991)

$$I = I_1 + I_2 + 2\left(I_1 I_2\right)^{\frac{1}{2}} \left|g_{12}\right| cos\varphi \qquad 7\text{-}2$$

where I_1 and I_2 are the intensities, g_{12} is the cross correlation, and φ is the phase delay between the two beams. The fringe visibility is defined as

$$V = \frac{I_{max} - I_{min}}{I_{max} + I_{min}} \qquad 7\text{-}3$$

where I_{max} and I_{min} are the maximum and minimum values of I when the mirror is moved. Since cosφ varies between 1 and –1 this leads to

$$V = \frac{2\left(I_1 I_2\right)^{\frac{1}{2}}}{\left(I_1 + I_2\right)} \left|g_{12}\right| \qquad 7\text{-}4$$

If $I_1 = I_2$, this simplifies to

$$V = |g_{12}| \tag{7-5}$$

The cross correlation g_{12} is equivalent to the degree of temporal coherence $g(\tau)$, which is related to the coherence time τ_c and the coherence length l_c:

$$\tau_c = \int |g(\tau)|^2 d\tau \tag{7-6}$$

$$\ell_c = c\tau_c \tag{7-7}$$

where c is the speed of light.

Interference occurs only when the optical path difference is smaller than the coherence length. l_c is the length where the fringes have totally disappeared and the fringe visibility is zero. In practice, this was defined as the point where the visibility dropped below 10%.

For the 1550 nm DFB laser used in this thesis, the coherence length was measured to be 0.27 mm ± 5%.

References

Abreu, V. J., Barnes, J. E., Hays, P. B., 1992. "Observations of winds with an incoherent lidar detector". Appl. Opt., 31, 4509-4514.

Agrawal, G. P., 1997. "Fibre-optic communication systems". John Wiley & Sons Inc. New York, USA.

Ahmed, Z., Onodera, N., 1996. "High repetition rate optical pulse generation by frequency multiplication in avtively mode-locked fibre ring lasers". Electron, Lett., 32, 455-457.

Barnes, W. L., Poole, S. B., Townsend, J. E., Reekie, L., Taylor, D. J., Payne, D. N., 1989. "Er^{3+} -Yb^{3+} and Er^{3+} -doped fibre lasers". J. Lightwave Technol., 7, 1461-1465.

Best, R. E., 1984. "Phase-locked loops: theory, design and applications". McGraw-Hill, New York, USA.

Bilbro, J. W., DiMarzio, C., Fitzjarrald, D., Johnson, S., Jones, W., 1986. "Airborne Doppler lidar measurements". Appl. Opt., 25, 2952-2960.

Bilbro, J., Fichtl, G., Fitzjarrald, D., Krause, M., Lee, R., 1984. "Airborne Doppler lidar wind field experiments". Bull. Am. Meteorol. Soc., 65, 348-359.

Bononi, A., Rusch, L.A., 1998. "Doped-fibre amplifier dynamics: A system perspective". J. Lightwave Technol., 16, 945-956.

Bononi, A., Tancevski, L., Rusch, L.A., 1999. "Large power swings in doped-fibre amplifiers with highly variable data". IEEE Photon. Technol. Lett., 11, 131-133.

Brown, R.G.W., Jones R., 1983. "Burst-correlation laser Doppler velocimetry". Appl. Opt. 8, 449-451.

Brown, R. S., Kozin, I., Tong, Z., Oleschuk, R.D., Loocka, H.P., 2002. "Fiber-loop ring-down spectroscopy". Journal of chemical physics, 117, 23.

Cai M., Liu X., Cui J., Tang P., Peng J., 1997. "Study on noise characteristic of gain-clamped erbium-doped fibre-ring lasing amplifier". IEEE Photon. Technol. Lett., 1093-1095.

Chanin, M. L., Garnier, A., Hauchecorne, A., Porteneuve, J., 1989. "A Doppler lidar for measuring winds in the middle atmosphere". Geophys. Res. Lett., 16, 1273-1276.

Clark, D. F., Moir, T. J., 1997. "Application of a PLL and ALL noise reduction process in Optical sensing system". IEEE Transactions on Industrial Electronics, 44, 136-139.

Doerr, R., Haus, H. A., Ippen, E. P., Shirasaki, M., Tamura, K., 1994. " Additive-pulse limiting". Opt. Lett., 19, 31-33.

Dorrington, A. A., Künnemeyer, R., Danehy, P. M., 2001. "Reference-beam storage for long-range low-coherence pulsed Doppler lidar". Applied Optics, 40, 3076-3081.

Drain, L. E., 1980. "The laser Doppler technique". John Wiley & Sons Inc., Chichester, Great Britain.

Fatehi, M. T., Giles, C. R., 1996. "Erbium-Doped Fibre Amplifiers with Wavelength-Selective Optical Feedback". IEEE Photonics Technology Letters, 8, 1012-1014.

Fischer, K. W., Abreu, V., Skinner, W. R., Barnes, J. E., McGill, M. J., Irgang, T. D., 1995. "Visible wavelength Doppler lidar for measurement of wind and aerosol profiles during day and night". Opt. Eng., 34, 499-511.

Giles, C. R., DiGiovanni, D., 1990. "Spectral dependence of gain and noise in erbium-doped fibre amplifiers". Photon. Technol. Lett., 2, 797-800.

Giles, R., Desurvire, E., 1991a. "Modeling erbium-doped fibre amplifiers". J. Lightwave Technol., 9, 271-283.

Giles, R., Stone, J., Stulz, L. W., Walker, K., Burrus, C. A., 1991b. "Gain enhancement in reflected-pump erbium-doped fibre amplifier". Tech, Dig. Optical Amplifier and Their Applicat. Washiongton. DC: Opt. Soc. Amer., 13, 148-151.

Gupta, K., Novak, D., 1997. "Millimetre-wave repetition-rate optical pulse train generetion in harmonically modelocked fibre ring lasers". Electron. Lett., 33, 1330.

Hall, F. F., Jr., Huffaker, R. M., Hardesty, R. M., Jackson, M. E., Lawrence, T. R., Post, M. J., Richter, R. A., Weber, B. F., 1984. "Wind measurement accuracy of the NOAA pulsed infrared Doppler lidar" Appl. Opt., 23, 2503-2506.

Harris, M., Kavaya, M. J., 1999. "Bistatic laser Doppler wind sensor at 1.5 μm". Technol. And Appli., 277.

Harris, M., Pearson, G. N., Vaughan, J. M., Letalick, Karlsson, D., 1998. "The role of laser coherence length in continuous-wave coherent laser radar". Journal of Modern Optics, 45, 1567-1581.

Henderson, S. W., Suni, P. M., Hayle, C. P., Hannon, S. M., Magee, J. R., Burns, D. L., Yuen, E. H., 1993. "Coherent laser radar at 2 μm using solid state lasers". IEEE Trans. Geosci. Remote Sens., 31, 4-15.

Huffaker, R. M., Hardesty, R. M., 1996. "Remote sensing of atmospheric wind velocities using solid-state and CO_2 coherent laser systems". Proc. IEEE, 84, 181-204.

Huve, J., Knief, A., Stroker, D., Mitschke, F., 1999. "Structure Formation in an Erbium-doped Fiber Ring Laser". Chaos, Solitions & Fractals, 10, 921-926.

Jackson, K. P., Newton, S. A., Moslehi, B., Tur, M., Cutler, C., Goodman, J., Shaw, H., 1985. "Optical Fibre delay line signal processing". IEEE Trans Microwave Theory Tech., MTT-33, 193-210.

James, J. F., 1995. "A student's guide to Fourier transforms: with applications in physics and engineering". Press Syndicate of the University of Cambridge, Cambridge, Great Britain.

Jeon, M. Y., Jeon, H. K., Lee, Ahn, J. T., Kim, K. H., Lim, D. S., Lee, E. H., 1998. "Pulse-amplitude-eqalization output from a rational harmonic mode-locked fibre laser." Opt. Lett., 23, 855-857.

Kakinume, T., Takeda, T., Nishimura, E., Tamura, Y., 1990. "Gain and noise characteristics of erbium doped fibre amplifiers with different pumping directions".in Tech. Dig. Optical Amplifiers and Their Applicat. Washington, DC: Opt. Soc. Amer, 13, 126-129.

Karásek, M., Bononi, A., Rusch, L. A., Menif, M., 2000. "Gain Stabilization in Gain Clamped EDFA Cascades Fed by WDM Burst-Mode Packet Traffic". Journal of Lightwave Technology, 18, 308-313.

Karlsson, C. J., Olsson, F. Å. A., Letalick, D., Harris M., 2000. "All-fibre multifunction continuous-wave coherent laser radar at 1.55μm for range, speed, vibration, and wind measurements". Appl. Opt., 39, No.21.

Kavaya, M. J., Magee, J. R., Hale, C. P., Huffaker, R. M., 1989. "Remote wind profiling with a solid-state Nd: YAG coherent lidar system". Opt. Lett., 14, 776-778.

Kavaya, M. J., Sume, P. J. M., 1991. "Continuous wave coherent laser radar: calculation of measurement location and volume". Appl. Opt., 30, 2634-2642.

Kim, Nam-Guk, Ha, In-Joong, 1999. "Design of ADPLL for both large lock-in range and good tracking performance". IEEE, Transactions on circuits and systems, Anolog and digital signal processing, 46, 9.

Kogelnik, H., 1964. "Coupling and conversion coefficients for optical modes". Pro. Quasi-Optics, 14, 333-347.

Korb, C.L., Gentry, B.M., Li, S.X., 1997. "Edge technique Doppler lidar wind measurements with high vertical resolution". Applied Optics, 36, 5976-5983.

Kringlebotn, J. T., Blotekjaer, K., Pannell, C. N., 1995. "Fibre Optic Sensor Based on a Sagnac Interferometer Including a Recirculating-Ring Delay Line with an EDFA". Fibre and Integrated Optics, 14, 265-285.

Kyo, Inoue, 1999a. "Gain-Clamped Fiber Amplifier with a Loop Mirror Configuration". IEEE Photonics Technology Lett., 11, 533-535.

Kyo, Inoue, 1999b. "Gain-Clamped Fiber Amplifier with a Short Length of Preamplification Fiber". IEEE Photonics Technology Lett., 11, 1108-1110.

Lee, K., Kim, K., Kim, H. G., 1999. "Pulse-amplitude equalization of rational harmonic mode-locked fibre laser using a semiconductor optical amplifier loop mirror". Opt. Commun., 160, 51-56.

Li, Shenping, Chan, K. T., 1999. "Wavelength-tunable actively mode-locked erbium-doped fibre ring laser using a distributed feedback semiconductor laser as mode locker and tunable filter". Applied Physics Lett., 75, 313-315.

Li, Zhihong, Lou, Caiyun, Tai, Chan Kam, Li, Yuhua, Gao, Yizhi, 2001. "Theoretical and Experimental Study of Pulse-Amplitude-Equalization in a Rational Harmonic Mode-Locked Fibre Ring Laser". IEEE Journal of Quantum Electronics, 37, 33-37.

Luo, L. G., Chu, P. L., 1997. "Suppression of self-pulsing in an erbium-doped fibre laser". Opt. Lett., 22, 1174-1176.

Mallat, S., 1998. "A wavelet tour of signal processing". Academic Press, New York, USA.

Marcuse, D., 1977. "Loss analysis of single-mode fiber splices". Bell Syst. Tech. J., 56, 703-718.

Massicott, J., Lebre, C., Wyatt, R., Kashyap, R., Williams, D., Yu, A., 1996. "Low noise, all-optical gain controlled Er^{3+} doped fibre amplifier using asymmetric control laser cavity design". Electron. Lett., 32, 816-817.

Massicott, F., Willson, S. D., Wyatt, R., Armitage, J. R., Kashyap, R., Williams, D., 1994. "1480 nm pumped erbium doped fibre amplifiers with all-optical automatic gain control". Electron. Lett., 30, 962-964.

Masuda, H., Takada A., 1990. "High fain two-stage amplification with erbium-doped fibre amplifier". Electron. Lett., 26, 661-662.

McGill, M. J., Skinner W. R., 1997. "Multiplefabry-perot interferometers in an incoherent Doppler lidar". Opt. Eng., 36, 139-145.

McGill, M. J., Spinhirne J. D., 1998. "Comparison of two direct-detection Doppler lidar techniques". Opt. Eng., 37, 2675-2686.

Nakazawa, M., Yoshida, E., Kimura, Y., 1994. "Ultrastable harmonically and regeneratively modelocked polarization-maintaining erbium fibre ring laser. Electron. Lett., 30, 1603-1605.

Yoshida, E., Nakazawa, M., 1996. "80-200 GHz erbium doped fibre laser using a rational harmonic modelocking technique". Eletron. Lett., 32, 1370-1372.

NASA, 1992a. "Tests show fewer air pockets". Aerospace Technology Innovation, 6, 8.

NASA, 1992b. "Making the Skies Safe from Windshear". NASA Facts Online, http://oea.larc.nasa.gov/PAIS/Windshear.html. (accessed 19 August 2002)

NASA, 1998. "ACLAIM: Airborne Coherent LIDAR for Advanced In-Flight Measurement". NASA Facts. FS 1998-04-042-DFRC, http://trc.dfrc.nasa.gov/PAO/PAIS/PDF/FS-042-DFRC.pdf. (accessed 19 August 2002)

Nishi, S., Aida, K., Nakagawa, K., 1990. "Highly efficient configuration of erbium doped fibre amplifier". ECOC '91, 1, 99-102.

Okamura, H., 1992. "Automatic loss compensation with an Erbium-doped fibre amplifier". J. Lightwave Technol., 10, 1110-1116.

Pearson, G. N., Collier, C. G., 1999. "A pulsed coherent CO2 lidar for boundary-layer meteorology". Quarterly Journal of the Royal Meteorological Society, 125, 2703-2721.

Post, M. J., Cupp, R. E., 1990. "Optimizing a pulsed Doppler lidar". Appl. Opt., 29, 4145-4158.

Saleh, B.E.A., Teich, M.C., 1991. "Fundamentals of Photonics". John Wiley & Sons Inc., New York, USA.

Schawlow, A. L., 1983. "Optical remote sensing". Springer series in optical sciences. 39, 383.

Shelekhov, A. P., 2000. "Doppler lidar measurement of the wind for the non-Gaussian signal in the turbulent atmosphere". Wave Propagation in the Atmosphere and Adaptive Optics, 4338 PG, 155-161.

Shirahama, Hiroyuki, Taniguchi, Kenji, Nakashi, Kenichi, 1995. "A very fast pull-in phase-locked loop with antipseudo-lock function". Electronics and Communications in Japan, 78, 104-114.

Sola, I. J., Martin, J. C., Alvarez, J. M., 2002. "980 and 1480 nm EDF characterisation by ring tunable laser dynamic study". Optics Communications, 203, 349-358.

Stewart, G., Atherton, K., Yu, H., Culshaw, B., 2001. "An investigation of an optical fibre amplifier loop for intra-cavity and ring-down cavity loss measurements". Institute of physics publishing, Meas. Sci. Technol., 12, 843–849.

Taylor, H. F., 1990. "Application of fibre optic delay lines and semiconductor optoelectronics to microwave signal processing". Proc. SPIE, 1371, 150-160.

Tipler, PA. 1983. " Physics". Worth Publishers Inc., New York, USA.

Truax, B.E., Demarest, F.C., Sommargren, G.E., 1984. "Laser Doppler velocimeter for velocity and length measurements of moving surfaces". Applied optics, 23, 67-73.

Vaughan, J. M., Steinvall, K. O., Werner, C., Flamant, P. H., 1996. "Coherent laser radar in Europe". Proc. IEEE, 84, 205-226.